AES/TG/13-16 **Static Reservoir Model of Crevasse Splays in the Colorado River System, Salar of Uyuni, Bolivia**

August 19th 2013 **Yadir Alexander Torres Carranza**

TU Delft Delft University of Technology

Challenge the future

Title	:	Static Reservoir Model of Crevasse Splays in the Colorado River System, Salar of Uyuni, Bolivia

Author(s)	:	Yadir Alexander Torres Carranza
Date	:	August 2013
Professor(s)	:	Dr. M.E (Rick) Donselaar Dr. Gert Jan Weltje
Supervisor(s)	:	Dr. M.E (Rick) Donselaar Dr. Gert Jan Weltje
TA Report number	:	AES/TG/13-16
Postal Address	:	Section for Applied Earth Science Department of Geoscience & Engineering Delft University of Technology P.O. Box 5028 The Netherlands
Telephone	:	(31) 15 2781328 (secretary)
Telefax	:	(31) 15 2781189

Static Reservoir Model of Crevasse Splays in the Colorado River System, Salar of Uyuni, Bolivia

Reservoir Modeling

Master of Science Thesis

For obtaining the degree of Master of Science in Reservoir Geology at Delft University of Technology

Yadir Alexander Torres Carranza MSc.

August 19th 2013

Delft University of Technology

Department of Applied Earth Science

The undersigned hereby certify that they have read and recommended to the Faculty of Civil Engineering and Geoscience for acceptance a thesis entitled **'Static Reservoir Model of Crevasse Splays in the Colorado River System, Salar of Uyuni, Bolivia'** by **Yadir Alexander Torres Carranza MSc** in partial fulfillment of the requirements for the degree of **Master of Science**.

Dated August 19th 2013

Supervisor:

Dr. M.E (Rick) Donselaar

Supervisor:

Dr. Gert Jan Weltje

Reader:

Dr. M.G.G. De Jong

This is dedicated to the memory of my Grandmother
Rosita, wherever you are, I will never forget you…

Abstract

The Altiplano Basin (Bolivia) exhibits one of the best examples of dryland river systems with a low gradient, where it is possible to obtain field data to build 3D high-resolution geological models of different sediment bodies. This study presents the development and understanding of a 3D geological model for crevasse splays deposited in this kind of basin. The data used consists of sediments in-situ and remote sensing data (satellite images). The integration of field and remote sensing data shows that the grain size has a better correlation with the channels location than the RGBD information from the satellites images. Likewise, with the grain size model, it is possible to visualize that porosity is not highly affected by the clay content, and due to the small grains, the initial predicted porosity is around 49 to 56%, which can be reduced to values below 7% because of overburden. According to grain size and porosity, permeability is around 350 to 600 mD, due to grain size distribution at surface conditions. These petrophysical properties are appropriated for gas storage and they can accumulate up to 3 MSCM of gas reserves in one single crevasse splay. As observed in the field, crevasse splays are vertically stacked resulting in a high net to gross ratio, and increasing gas reserves up to 300 MSCM of gas in-situ, making these reservoirs an attractive target for exploration in fluvial systems.

Acknowledgements

"Life's as kind as you let it be"
Charles Bukowski

The completion of this MSc project would not have been possible without the financial support provided by Delft University of Technology and Delft University Fund Foundation (Ufd). Likewise, I would like to thank my supervisors Dr Rick Donselaar and Dr Gert Jan Weltje for their unconditional support, guidance and all the knowledge and experience provided. I would like also to thank Menno Bloemsma and Jiaguang Li, who were an important help during the field data acquisition and the subsequent processing stages.

I am deeply grateful for the outstanding family I have, who have been always by my side giving me support and enlighten me during the tough moments. Special thanks to my girlfriend Andrea for being with me all this time helping me and encourage me every single moment with warm words and inspiring actions. Thank my heart for getting into my life at the right time and the right moment.

Finally, I would like to express my infinite thanks to my grandmother Rosita, who showed me all the beauty things in life even during her last moments. Thanks 'Abuelita' for being always there.

Abbreviations

ALR	Additive-log-ratio
α_v	Specific internal surface area
Bgi	Initial gas formation volumetric factor
BRV	Bulk rock volume
CLR	Centered-log-ratio
cm	Centimeters
FDP	Field Development project
GIIP	Stock gas in place
GPS	Global Positioning System
GS	Grain Size
GSD	Grain Size Distribution
H_2O_2	Hydrogen Peroxide
HCl	Hydrochloric acid
k	Permeability
km	Kilometers
m	Meters
Ma	Million Years
mD	Millidarcy
MSCM	Millions of standard cubic meters
NTG	Net to gross
RCM	Reservoir cubic meters
RGBD	Red, Green, Blue, Darkness
SCM	Standard cubic meters
Sg	Gas Saturation
XN	Crossed Nicols
Z	Depth
µm	Microns
τ	Tortuosity
ϕ	Porosity

Contents

List of Figures

List of Tables

Introduction

Crevasse splays are part of fluvial systems in which such sediment bodies are treated by reservoir geoscientists as hydrocarbon reservoirs being an important item for economic analysis in the oil industry. Nowadays due to the lack of hydrocarbon accumulation into fluvial conventional reservoirs such as point bars, many operator companies and geoscientists have become more interested in these kinds of reservoirs due to their areal extension and their reservoir properties. A good understanding of crevasse splays in terms of reservoir architecture, reservoirs properties and hydrocarbons reserves are crucial to have a new perspective about their role in the oil industry.

Despite the available data and technology used to characterize clastic reservoirs in subsurface such as image logs, cores, seismic data, etc., information acquired about reservoir sedimentology on crevasse splays still quite limited. Therefore, it is necessary to carry out sedimentological studies on field analogues to understand the sedimentology of these bodies better, which in turn could provide enough information for geoscientists to characterize such reservoirs.

Different authors have carried out few studies on crevasse splays but just some of them have been focused on the sedimentology and reservoir architecture issues like Bridge (1983), O'Brien (1986), Smith (1989), Bristow, Skelly, & Ethridge (1999), Farrell (2001), and Anderson (2005). The information collected in these studies has been conditioned by the quality of the outcrops in the case of ancient crevasse splays and by environmental conditions in recent crevasse splays. Therefore, finding recent crevasse splays with adequate conditions such as absence of vegetation and a good 3D exposition are remarkably important for a better understanding of these sediment bodies.

There are only few places around the world, where due to the arid conditions, the absence of vegetation and good pavement outcrops it is possible to acquire sedimentological information of sediment bodies with a high degree of detail. One of these places is the southwest part of Bolivia at the province of Potosi (Fig. 1). Several semi-arid river systems are present. As shown in figure 1, one outstanding example of such kind of systems is the Colorado River (in blue). Due to its remarkable exposition and good preservation of its deposits, the Colorado River was chosen for a large research project supported by Delft University of Technology of which this study belongs.

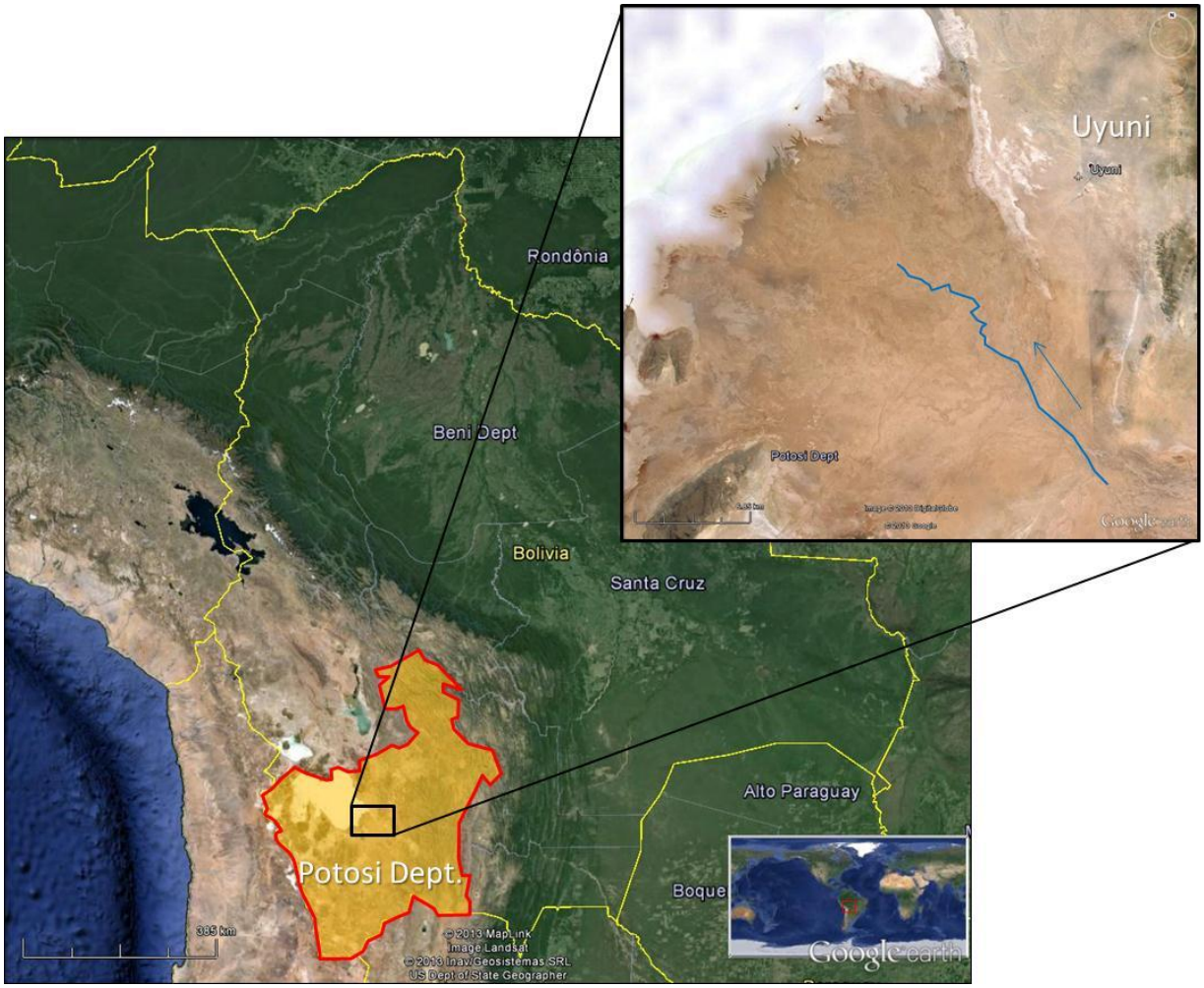

Figure 1. Study Area of the project 'Modeling of Fluvial Systems in Semi-Arid Endorheic Basin'.

This study constitutes an MSc Thesis carried out at Delft University of Technology in the frame of the Petroleum and Geoscience curriculum. This thesis is part of a large project called '*Modeling of Fluvial Systems in Semi-Arid Endorheic Basin'* supervised by Prof. Rick Donselaar and executed by Jiaguang Li at the department of Applied Earth Science. The objective of this project is to model and characterize all the sediment deposits related to the Colorado River system from the catchment area until the edges of the Basin. Therefore, it is required to model all the deposits present along the Colorado River in which crevasse splays are part of the system.

The principal aim of this MSc thesis is to build up a detailed static model of several crevasse splays related to the Colorado River system based on grain size distribution. This static model will be created by modeling different properties such as grain size, thickness, facies, porosity and permeability. Based on the integration of some of these properties different realizations will be generated to quantify the hydrocarbons present in a crevasse splay. The result of the static model and the hydrocarbon volumes will be compared with analogue fields that produce gas from similar reservoirs with the aim of evaluating to which extent the static model can be representative of a hydrocarbon reservoir.

In order to achieve these objectives a four-week geological fieldwork at the Uyuni area in Bolivia (Fig. 1) was carried out for data acquisition between November and December of 2012. The data acquired during the fieldwork consists of sediment samples taken from the newest event of two crevasse splays chosen prior to the fieldwork. Additionally, several lacquer peels were taken from vertical sequences of such crevasse splays with its description of sedimentary structures and facies. This was complemented with high resolution photographs of artificial vertical sections made by digging several holes into these crevasse splays. Besides the acquisition data, high-resolution satellite images were used with the aim of correlating them with the information found in the field. The purpose of which is describing some of the properties mentioned above in detail. Once all the data was acquired, grain size processing data per sample was performed in order to obtain representative grain size distributions in their respective areas, which in turns was correlated with processed data from satellite images of the crevasse splays. Based on these correlations, the static model of both crevasse splays was built. These models were used to obtain hydrocarbons volumes for each crevasse splay.

In this report you will find, first a brief description of the geological setting of the study area (Chapter 1), then Chapter 2 will show you how the data was acquired and what kind of methodology was used to collect such information. Chapter 3 will be about how the field data was interpreted and how this interpretation was used to create a geological conceptual model of the crevasse splays. Chapter 4 will describe how the grain size data was processed and analyzed in order to create a detailed 3D grain size model. Finally in Chapter 5, a full static model will be developed. Based on this model, deterministic and stochastic hydrocarbon volumes will be determined per crevasse splay to have an idea to which extent those volumes match analogues in the oil industry.

1. Geological Setting

Rivers systems are the product of different conditions such as climate, vegetation, tectonics and sea level. For example, dryland river systems show a downstream decrease in channel width and depth in its terminal parts due to dry climate conditions. These distal bodies differ from the terminal parts of classic river systems in terms of how they are developed. For instance, the first kind ends at the floodplain, while classic rivers form lacustrine deltas (Donselaar, Gonzalo Cuevas, & Moyano, 2012). In order to understand the morphology pattern and the model behind of such kinds of deposits, a research project was developed on the Colorado River by Dr. Donselaar in 2010 and 2011. From the results of such research, a fieldwork was carried out with the aim of acquiring field data to build up a static model of crevasse splays in dryland river systems. The information regarding to acquisition will be described in more detail in Chapter 2. This fieldwork was conducted in Bolivia - Province of Potosi (Fig. 2). The study area comprises many different sediment bodies such as crevasse splays along the Colorado River, which in turns is located approximately at 10 km southwest from Uyuni. Geologically speaking, the study area is situated within the Altiplano basin, which will be briefly described in the next section.

1.1. The Altiplano Basin

The Altiplano Basin is a North-South elongated endorheic basin of 200,000 km^2, which extends through Peru, Bolivia and Chile. The basin has an altitude that varies between 3650-4200 m above sea level and it was developed as part of the Andean orogenic system. This has an extension of 8000 km and it can be sub-divided into three segments. From north to south, these segments are the Colombia-Ecuador segment, the Peruvian segment and the Chilean-Bolivian Segment (Jaillard, et al., 2000). Here, we are going to expand on the formation of the Chilean-Bolivian segment, due to its relevance with respect to the study area.

The Chilean-Bolivian segment of the Altiplano Basin is bounded by the Cordillera Occidental and the Cordillera Oriental. The first cordillera is made of Neogene-Quaternary arc rocks that include several volcanoes, which can reach up to 6000 m. There are few an isolated outcrops, where it is possible to see the unconformable contact between Tertiary arc rocks overlaying the Precambrian basement (Jaillard, et al., 2000). This cordillera represents the western limit of the Altiplano, which is approximately 200 km

wide and filled with a thick sequence (thousands of meters) of Tertiary and Quaternary rocks (late Pleistocene to Holocene deposits). On the other side, the Altiplano is bounded by the Cordillera Oriental that is made of Paleozoic folded metasediments, which are thrust to the SW onto the Altiplano border.

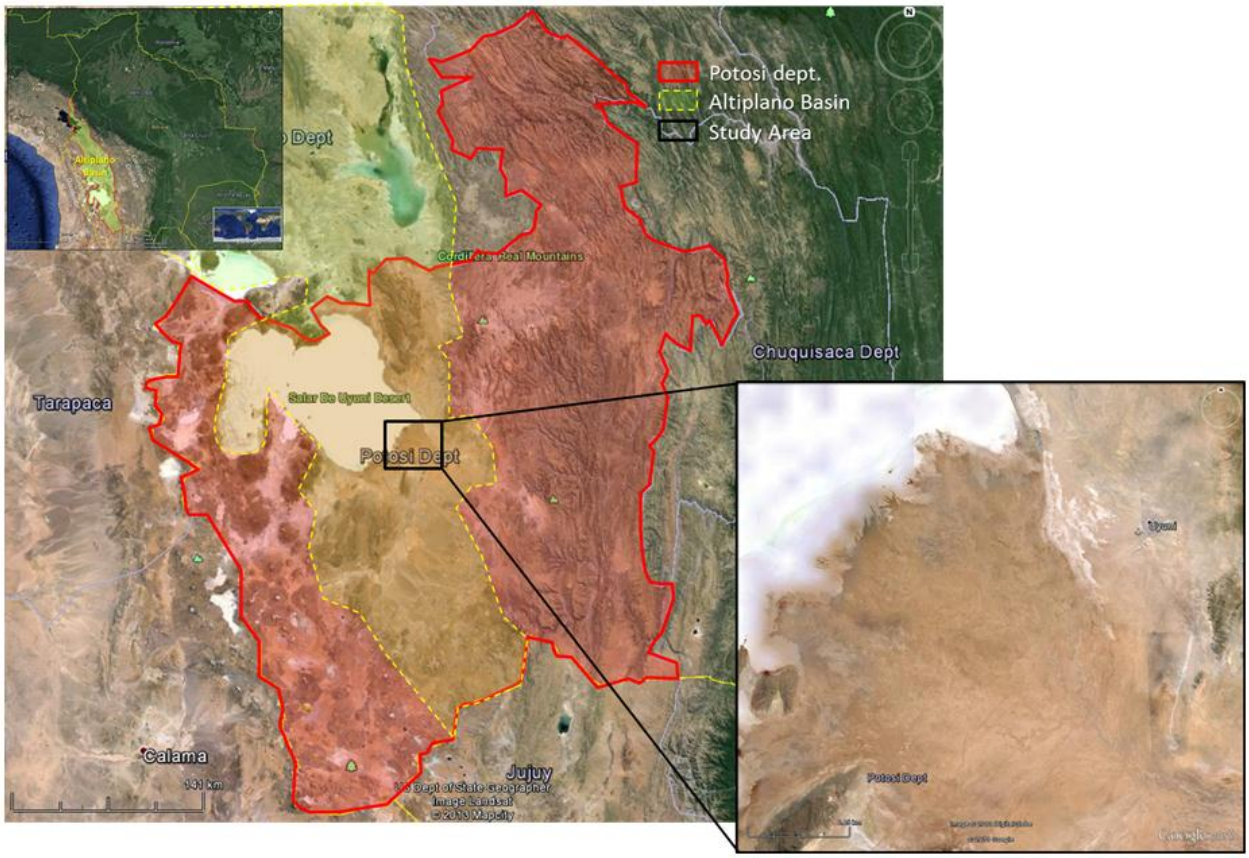

Figure 2. Study Area Map.

The origin of the basin relates to the subsidence phase that reached its maximum development after the uplifting of the Andean geosynclinal during the late cretaceous and early tertiary age (Rodriguez, 1985). This process and the intense volcanism produced that most of the deposits covering the basin belongs to the tertiary and the quaternary ages. These deposits are mainly Tertiary ash-flow tuffs, clastic continental sediments and deposits related to stratovolcanoes (Ericksen & Salas, 1989). The Altiplano reaches its maximum altitude to the north at Lake Titicaca, while in the Salar de Uyuni it has an altitude of 3653m representing the lowest part of the basin and its central current axis.

In terms of the composition of the deposits that are filling the Altiplano basin, the large amount of salt present into the lakes and salars is interpreted as the result of leaching of ash-flow tuffs, which contain considerable amounts of water-soluble saline material (Ericksen & Salas, 1989). These ash-flow tuffs are the result of several phases of volcanism. The earliest volcanism phase occurred during the Miocene and Early Pliocene. This was characterized by explosive caldera type eruptions of dacitic to rhyolitic ash-flow tuffs, covering a large area of the Altiplano. Afterwards, many andesitic stratovolcanoes were developed during the Pliocene and the Quaternary, overlaying the ash-flow blanket deposits from the Miocene

(Jaillard, et al., 2000). Nowadays these volcanoes are in a passive stage, showing some fumarolic activity and have had a few eruptions in the past. In addition, the basin is filled with quaternary clastic fluvial and lacustrine sediments exposed in some outcrops along the Cordillera Oriental.

In addition, the basin is related to the Andean uplift, which means that it had been tilted in various directions due to tectonic movements. These tectonic movements result in irregular salars shapes and compositions. In other words, the shape and the composition of the salars are directly related to the tectonic history of the area.

1.1.1. Basin Evolution

In terms of geological evolution, the Altiplano Basin is a geomorphological depression that has been changing since the early Tertiary (Rodriguez, 1985). It started forming due to uplifting of the Cordillera Occidental and Cordillera Oriental. As result of the uplifting, lacustrine and fluvial sediments are being deposited into the basin by influx of sediments from the surrounding cordilleras.

Back in the early Tertiary, after the formation of the Cordillera Oriental and the Cordillera Occidental, these became in the boundaries of the basin. After that, the Altiplano Basin has been filled by deposits product of volcanism and clastic continental sediments, which are mainly lacustrine and fluvial deposits (Lavenu, 1991). In order to understand the evolution of the basin, several lacustrine deposits have been studied as well as their relationship to climate changes during the Pleistocene and the Holocene. These relationships give some clues on how to recreate the history of the basin (Servant & Fontes, 1978). Therefore, in order to have a good idea of the history of the basin, these lacustrine deposits are going to be described in detail, starting from the oldest deposit and extending to the most recent lacustrine deposit.

Early Pleistocene

During the Pleistocene epoch, two main formations were deposited and from old to young these are the Mataro Formation and Cabana Formation. The first one shows fluvial detritical facies that are represented by siltstone to sandstone brown layers alternated with massive sandstone layers and pebbles clasts. The Mataro Formation exhibits its highest erosional surface at a current altitude of 3950 m above sea level and its maximum thickness recorded in the area is about 50m in a vertical section. The oldest fossil found denotes that the formation belongs to an undifferentiated quaternary and can be correlated to the Purapurani Formation in the La Paz Basin and to the south with the Ayo Ayo Formation (Hoffstetter, 1971).

Subsequently, the Cabana Formation incised the Mataro deposits showing a lake-level of 3900 m above sea level. The thickness of the Mataro formation is about 50 m and its deposits are described as lacustrine deposits composed of blue and red-color laminated siltstone and sandstone. These deposits are referred to as middle Pleistocene and can be correlated with the Ulloma Formation in Viacha, Pando and Ulloma areas (Argollo Bautista & Irondo, 2008).

Outcrops of these deposits in the North and Centre of the Altiplano Basin demonstrate that (Lavenu, 1991) the paleo-lakes had the same lake-level along the whole Altiplano. This differs from the current development of lakes such lakes Titicaca and Popoo, which are separated by the Desaguadero River.

Late Pleistocene

The upper Pleistocene is composed of deposits from Lake Ballivian and Lake Minchin. The Lake Ballivian deposits incise the Cabana deposits, and according to South-American chronology, they can be dated to the Ensenadense or lower Lujanense era (Lavenu, 1991). The Ballivian lake-level can be found at 3840 m above sea level and its deposits are formed by intercalation of fine sandstone layers and siltstone and claystone layers (Argollo Bautista & Irondo, 2008). Cutting the Ballivian deposits, younger sediments deposited by lake Minchin were found. These deposits marked the end of the Pleistocene epoch. The deposits in Lake Minchin are characterized by accumulations of algaes, stromatolite and silt to sand sediments with high calcareous content. These deposits are the product of glacial melting from the Choqueyapu glaciation. In terms of age, these deposits have been dated to the Lujanense age and are undifferentiated by Marshal and Sempere (1991).

The lake-levels of both deposits showed that the lakes were separated by a paleo-high, dividing the basin into two sectors, one to the north and other to the south. The northern part of the basin developed a smaller lake than in the southern sector (Lavenu, 1984). The existence of this separation can be seen from the differences in terrace altitudes. For example, the deposits of Lake Ballivian exhibit terrace altitudes of 3860m to the north while to the south the same deposits developed terraces at 3780 m.

Holocene

The Holocene is represented by the deposits of Lake Tauca with an altitude of 3715m to the North, 5m above the current altitude of Lake Titicaca (Lavenu, 1984). To the south, the lake has an altitude of 3720 m. Its extension in the area was about 43,000 km^2 in contrast to the 9,000 km^2 to the north (Fig. 3). These areas have decreased their extension continuing into what nowadays is called Lake Titicaca (8,560 km^2) at the north, Lake Popoo in the center and the salars Coipasa and Uyuni to the south.

The deposits of Lake Tauca are composed of lacustrine diatomite of two to five meters thick interbedded by fine sandstone layers that occasionally show intercalation of fluvial gravel and sandstones layers with cross stratification. These deposits indicate a date between 12,500 and 10,000 yr. according to Servant and Fonts (1978).

Currently, Lake Titicaca, Lake Poopo and Salar Copaisa and Uyuni (Fig. 3) divide the Altiplano Basin from North to south. The water level of these lakes is controlled by evapo-transpiration and precipitation gradient, which decrease from north to south resulting Lake Titicaca in a permanent fresh water lake while Salar Coipasa and Uyuni result in seasonal hyper saline lakes (Donselaar,

Gonzalo Cuevas, & Moyano, 2012). The highest precipitation occurs between December and March period, when the air from the Amazon Basin overpass the Cordillera Oriental.

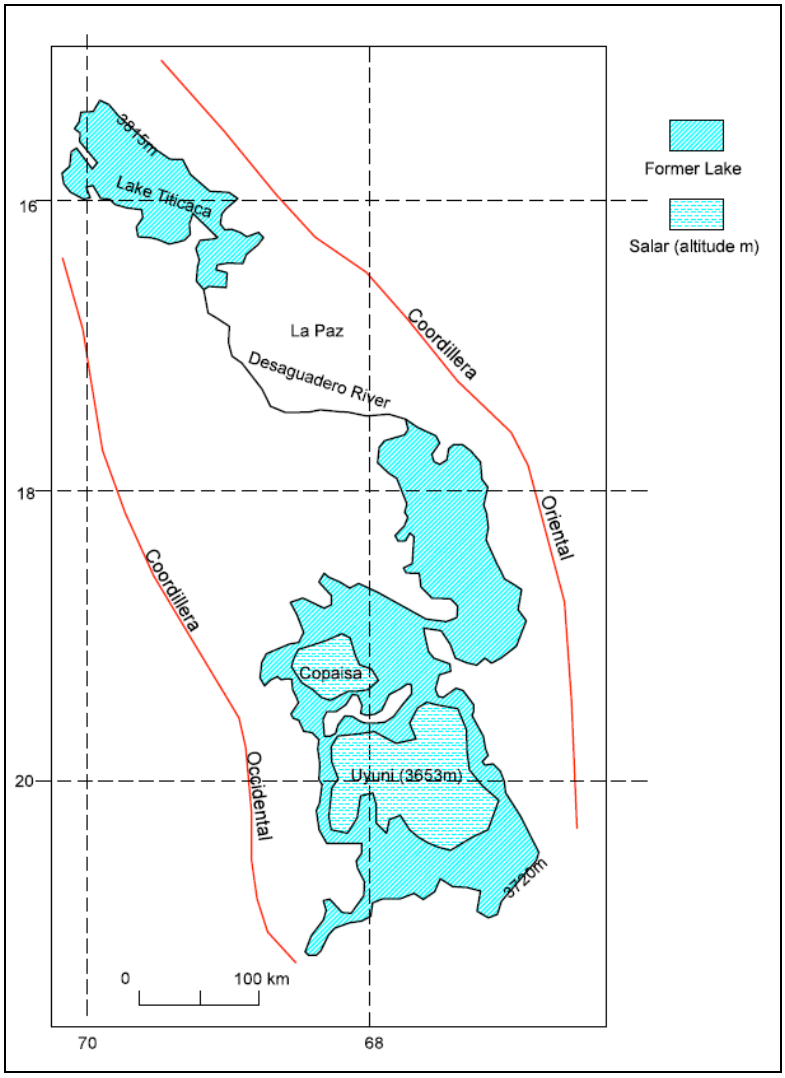

Figure 3. Maximum extension of former larger lakes during the Holocene. (Modified from Ericksen 1989)

Regarding to the relationship between the deposits and the climate changes, some studies (Baucom & Rigsby, 1999) have shown that the limit between the Pleistocene and Quaternary is determined by remarkable climate change, which is recognizable by rapid local cooling at 3 Ma. This results in characteristic facies of the glacial and interglacial environment in the highlands, fluvial facies at the foothills and lacustrine and evaporitic facies at the center of the basin. These facies contrast with the fluvial and lacustrine sediments deposited during the Pleistocene in hot environmental conditions (Lavenu, 1991).

Some studies (Servant & Fontes, 1978) performed in several main paleo-lakes have shown that this relationship between the lacustrine deposits and the glaciation episodes (Fig 4) is proven in at least six of the successive lacustrine deposits. These paleo-lakes show their maximum extension represented by

different lake-levels (Fig. 5) at the end of each glaciation due to the melting of the glacial layer (Servant & Fontes, 1978).

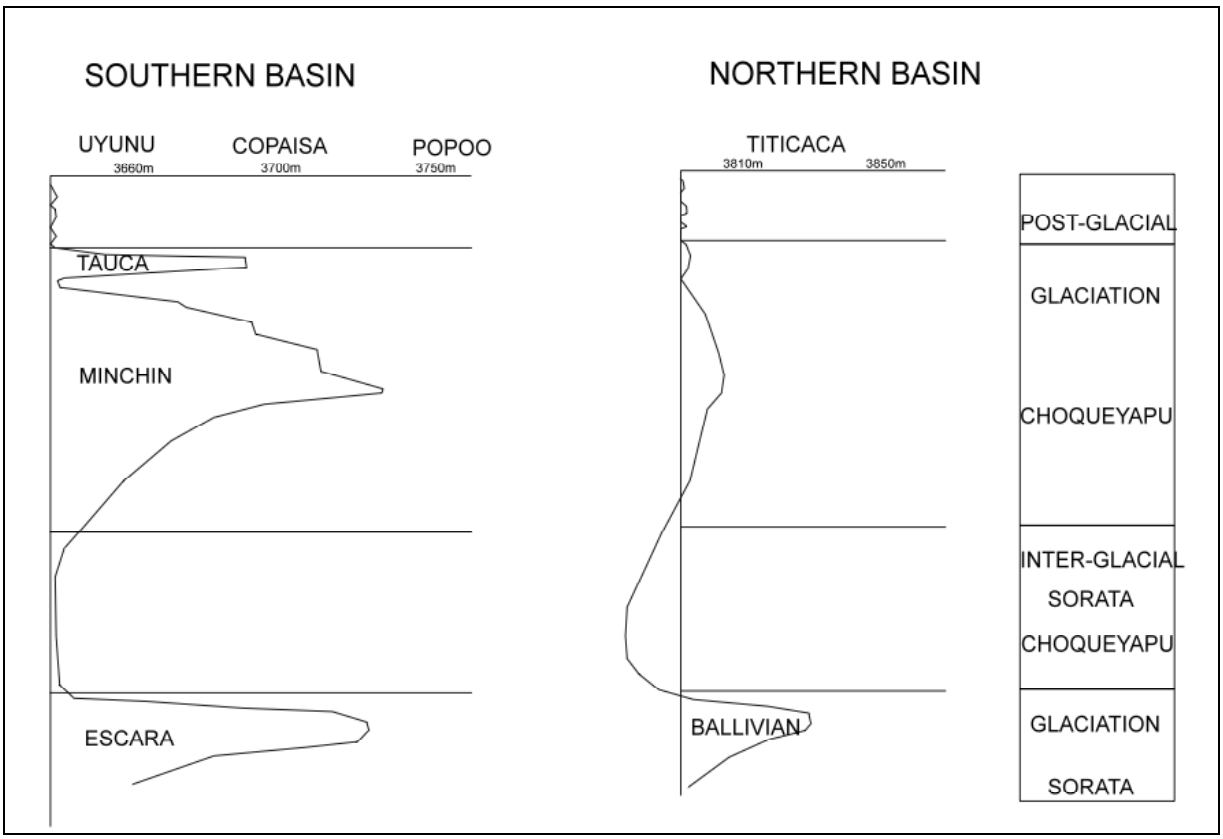

Figure 4. Correlation between Glacial formations and lacustrine deposits in paleo-lakes. (Modified from Servant & Fontes, 1978).

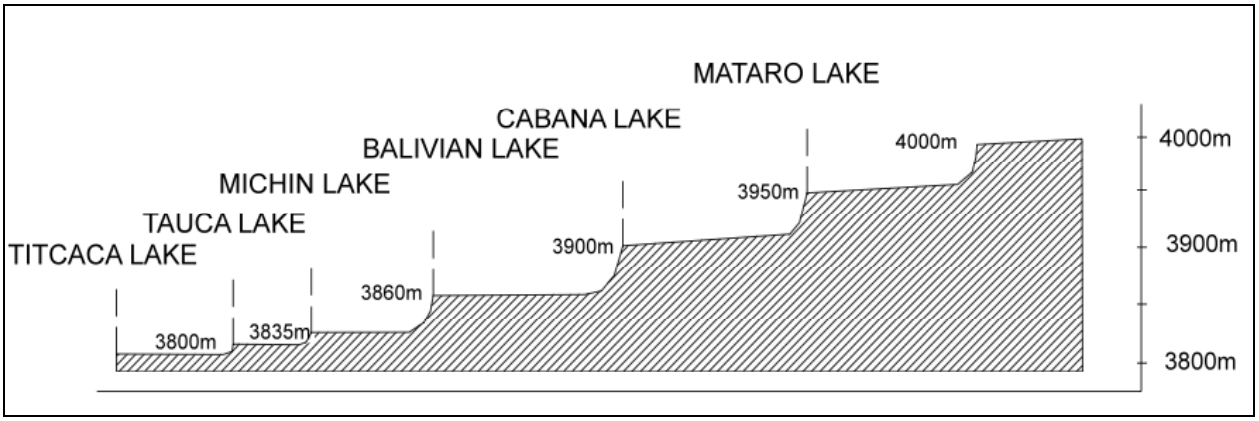

Figure 5. Lakes elevation in the Quaternary - Altiplano Basin (Modified from Lavenu, 1991).

The late Pleistocene and Holocene are represented by the deposits of the paleo-lakes Minchin, Tauca and Copaisa. The lake-level variations of such paleo-lakes are correlated with high stand deposits (HST) and low stand deposits (LST). The deposits of the Salar of Uyuni are interpreted as low stand deposits due the low annual precipitation (196 mm/yr.). This precipitation is mostly concentrated within three

weeks of the years, causing massive over bank deposits with high levels of sediment discharges that exceed the channels capacity (Donselaar, Gonzalo Cuevas, & Moyano, 2012).

As a result of these conditions and the scarce vegetation on the Altiplano Basin, the Colorado River is developed. This river drains from the southeast (west flank of Cordillera Oriental) to northwest (Salar de Uyuni) with a total drainage area of 15.000 km^2 (Fig 6) and it is characterized by five particular segments described by Donselaar, Gonzalo Cuevas, & Moyano (2012).

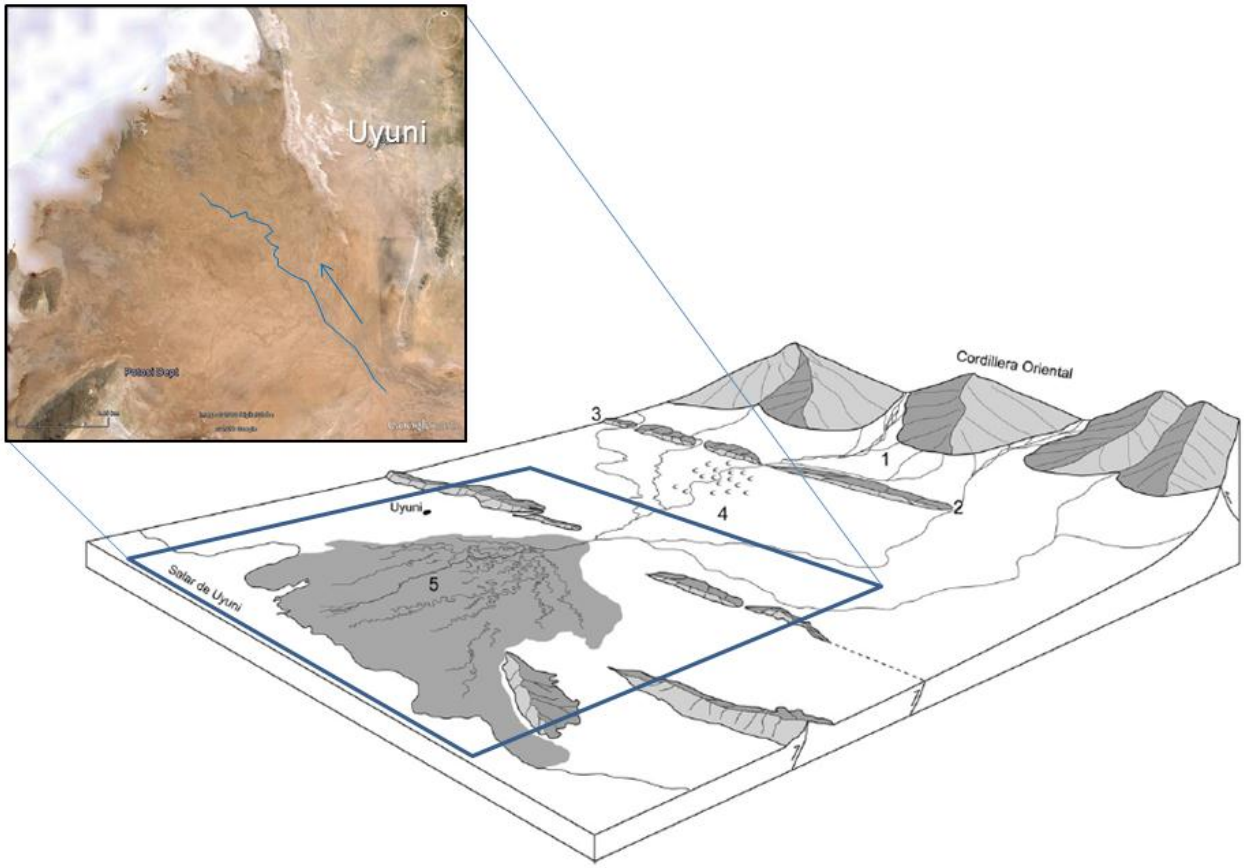

Figure 6. Block diagram of the Colorado River (not to scale). Lower coastal plain in grey. Modified from Donselaar, Gonzalo Cuevas, & Moyano, 2012.

This river system (figure 6) can be characterized from upstream to downstream in five regions. (1) a dendritic pattern of small distributary channels, (2) narrow canyons, (3) steep alluvial fans, (4) upper lacustrine coastal plain and dunes crossed by tributary channels and (5) a lower coastal plain with a divergent channel pattern spreading out over an approximated area of 500 km^2 (Donselaar, Gonzalo Cuevas, & Moyano, 2012). This study will be focus on the segment (5), which is characterized by a low slope gradient ($8.3E^{-5}$) composed by ochred coloured mud to very fine sand partially cemented by salt. Morphologically speaking, the coastal plain is constituided by a dense network of sinous river channels (Donselaar, Gonzalo Cuevas, & Moyano, 2012) with its respective point bars, crevasse channels and splays that will be matter of study in the next chapters.

2. Data Acquisition and Methodology

In order to build a 3D static reservoir model of a crevasse splay, it is necessary to obtain field data on size and shape distribution of the fluvial elements and sedimentary characteristics, such as spatial distribution of grain size and sedimentary structures. In order to collect this information several crevasse splays were selected in the research area along the Colorado River, Bolivia. This selection was done using Google Earth pro and following the current flow channel of the Colorado River (Fig. 7).

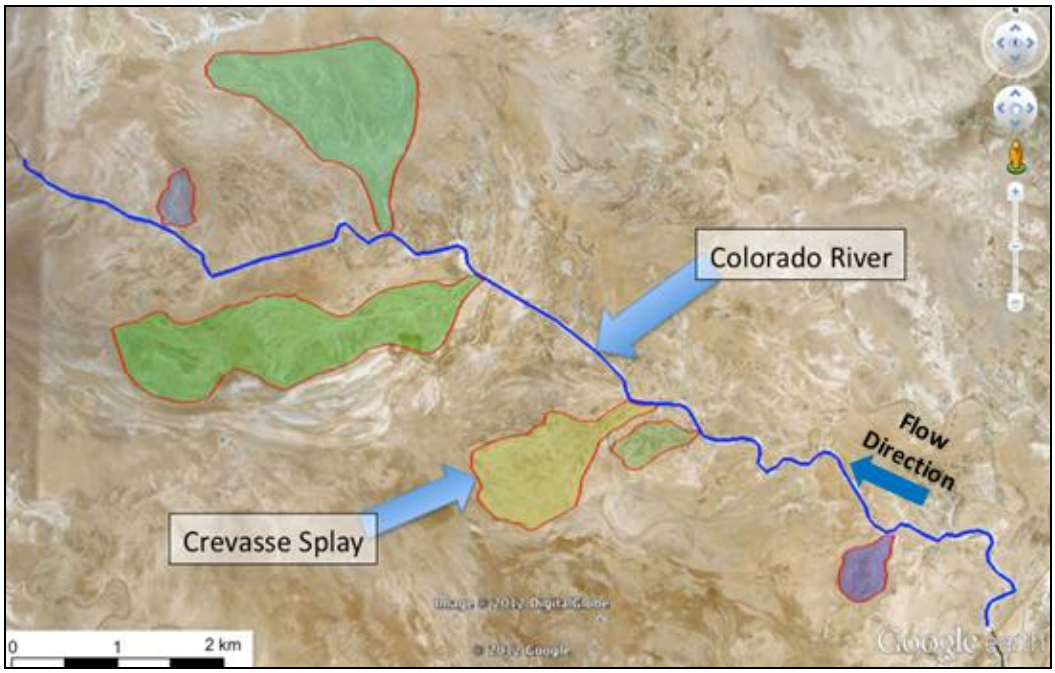

Figure 7. Crevasse Splay identification along the Colorado River. Google Earth Pro

Once the most visible crevasse splays were recognized, two of them were chose in order to prepare a logarithmic grid for measurement purposes (Fig 8). The aim behind the logarithmic grid consisted to have a good sampling in the proximal parts due to its probable large variation (Bridge, 1984), in contrast

to the low variability that would be present in the distal areas of the crevasse splays. After creating the logarithmic grids, junction points were marked in Google Earth pro and each point was numbered (Fig 8 - Appendix 1) and transferred to a hand-held GPS device.

Figure 8. Sampling Logarithmic Grid a) Crevasse Splay 1; b) Crevasse Splay 2. Google Earth Pro

Next, using the data points uploaded in a GPSmap 60CSx-Garmin, the fieldwork stage was conducted from late November to December of 2012 to avoid the rainy session. In order to acquire the data regarding to grain size distribution, sediment samples were taken and stored in Ziploc bags of 100 cc at every single point over the grid designed beforehand on the Crevasse Splays 1 and 2 (Table 1).

These samples were obtained at 5 to 10 cm below the surface in order to have a representative sediment sample, which later on were correlated with remote sensing data. The samples were taking at these depths to avoid contaminated samples with salt crystals due to the presence of a superficial salt cap of 2-4 cm thick over most of the study area.

Table 1. Samples collected along the Colorado River - UTM Coordinates

Crevasse Splay 1			*Crevasse Splay 2*		
Point	**East-X(m)**	**North-Y(m)**	**Point**	**East-X(m)**	**North-Y(m)**
C1	713028,68	7730576,79	C2-1	715407,39	7728816,37
C1-1	713025,32	7730669,95	C2-2	715412,96	7728806,60
C1-2	713004,12	7730666,62	C2-3	715422,97	7728794,07
C1-3	712985,65	7730659,95	C2-4	715332,91	7728785,28
C1-4	713021,61	7730764,88	C2-5	715342,19	7728762,83
C1-5	712979,36	7730758,52	C2-6	715361,39	7728738,74
C1-6	712942,30	7730744,35	C2-7	715248,18	7728749,81
C1-7	713016,63	7730875,26	C2-8	715264,82	7728715,93
C1-8	712950,23	7730865,51	C2-9	715294,03	7728679,31
C1-9	712891,67	7730842,22	C2-10	715150,42	7728710,77
C1-10	713011,63	7731000,81	C2-11	715175,07	7728661,79
C1-11	712917,33	7730986,65	C2-12	715213,90	7728607,25
C1-12	712832,99	7730954,03	C2-13	715034,78	7728663,98
C1-13	713005,80	7731152,11	C2-14	715067,29	7728598,14
C1-14	712877,90	7731132,54	C2-15	715120,31	7728526,23
C1-15	712998,48	7731334,94	C2-16	714890,60	7728603,66
C1-16	712829,43	7731310,19	C2-17	714933,70	7728516,76
C1-17	712679,04	7731251,01	C2-18	715004,04	7728422,66
C1-18	712989,63	7731570,25	C2-19	714711,52	7728530,16
C1-19	712767,32	7731536,99	C2-20	714768,57	7728418,37
C1-20	712570,53	7731460,24	C2-21	714860,78	7728295,07
C1-21	712975,81	7731903,93	C2-22	714447,14	7728421,49
C1-22	712681,04	7731859,80	C2-23	714523,90	7728269,04
C1-23	712416,77	7731757,46	C2-24	714647,92	7728105,02
C1-25	712530,64	7732405,90	C2-25	714002,35	7728242,30
C1-26	712157,04	7732262,68	C2-26	714113,25	7728024,29
C1-27	711405,80	7732350,75	C2-27	714289,16	7727786,35
C1-28	711951,31	7731696,34	C2-30	714796,15	7727846,41

Micro pictures of grain size in situ (Fig 9) were taken with a digital microscope camera for grain size analysis. Initially, these pictures were obtained in every single point of the logarithmic grid but due to its low resolution and quality, this procedure was cancelled. On these pictures, it is noticeable that most of the grains are present as part of aggregates (Fig 9). Moreover, high proportion of gypsum crystals were recognized in some pictures at random areas.

Besides the sediment samples and micro pictures in situ, holes with dimensions (length, wide and depth) of 1.0*1.0*0.5 m were dug in the field. The aim of these holes was to describe sedimentary structures present vertically along the crevasse splays and to obtain lacquer peels from the walls of the trenches. These lacquer peels recorded information about sedimentary structures and vertical grain size trends at some locations of the crevasse splays. In total nine lacquer peels were obtained (Appendix 1) within both crevasse splays. From the lacquer peel acquisition, it was realized that this technique works better with dry sediments than with wet sediments. This shows that the best information regarding to

sedimentary structures and grain size is recorded in the lacquer peels acquired on the Crevasse Splay 2. These are located at the most proximal areas along the Colorado River.

Figure 9. Sediment Micro Pictures InSitu

Additionally to the sediment sampling and lacquer peel collection, gross thickness was measured over the Crevasse Splays 1 and 2. The criterion to measure the thickness of each crevasse splay was based on the composition of the main sediment body and the sediment body underneath. In this case, the shallower sediment body, which it is the target of the research, is composed mainly of silt and very fine quartz grains and in some cases gypsum. On the other hand, the lower sediment body is composed by high clay proportion (floodplain mud).

Figure 10. Boundary definition using Color as indicator. a) Crevasse Splay 1 point 25. b) Crevasse Splay 2 point 8.

These sediment bodies were differenced by color (Fig. 10) due to the crevasse splay has a light yellowish color, in contrast to the brownish dark color that exhibits the lower layer. Gross thickness is listed in table 2.

Table 2. Gross Thickness Crevasse Splay 1 and 2.

Crevasse Splay 1		*Crevasse Splay 2*	
Point	Gross Thickness (cm)	Point	Gross Thickness (cm)
C1-4	10	C2-1	28
C1-5	22	C2-2	12
C1-6	5	C2-3	12
C1-7	15	C2-4	15,5
C1-8	12	C2-5	12
C1-10	12	C2-6	12
C1-11	10	C2-7	10,5
C1-12	8	C2-8	9,5
C1-14	24	C2-9	10
C1-15	9	C2-10	9
C1-16	12	C2-12	10
C1-17	7,5	C2-13	7
C1-19	6,5	C2-14	30
C1-20	7	C2-15	10,5
C1-21	15	C2-16	9,5
C1-22	12	C2-17	8,5
C1-23	15	C2-18	7,5
C1-25	1	C2-19	12
C1-26	3	C2-21	6,5
C1-27	6,5	C2-23	28
		C2-24	6,5
		C2-27	7

The samples collected in the Crevasse Splays 1 and 2 were analysed in Uyuni using a high-resolution digital microscope camera (Fig. 11). After taking several series of pictures, it was seen that the grains were highly wet and thus the information obtained were related to aggregates, which gave wrong results about single grain sizes. For this reason, the samples acquired were dried up at 100C for one week in the laboratories of TU Delft. The aim of this procedure was to separate single grains to carry out a proper grain size analysis following two different methods. The first method consisted in taking micro pictures of the sediments collected in the field to carry on a grain size analysis of each sample with QWin. The second method involved a laser analysis of each sample, this was done in the University of Amsterdam and it will be described in the next section.

Figure 11. Conrad DP-M17 USB Digital Microscope, 10x to 200x Magnification, 9.0 Megapixel High Resolution.

2.1. Image Analysis

The aim of this analysis consisted to obtain a grain size distribution using micro pictures and processing them with QWin, (image analysis software). This analysis requires dry sediments to avoid measuring aggregates, which are the result of humidity and clay present in the sample. Consequently, subsamples were taking into the laboratory to dry them up. After that, the sub-samples were taken to the digital microscope set with an equal spaced grid (blue background) of 1 mm. These pictures were revised and based on their quality (Fig. 12) 69 out of 424 were pre-selected to be the input for imaging analysis. This selection was carried out by identifying single grains in each picture, and then pictures of aggregates were rejected. From this selection, (Table 3) 45 images belong to the Crevasse Splay 2 show better results than the crevasse splay 1, which still showing aggregates after the drying process.

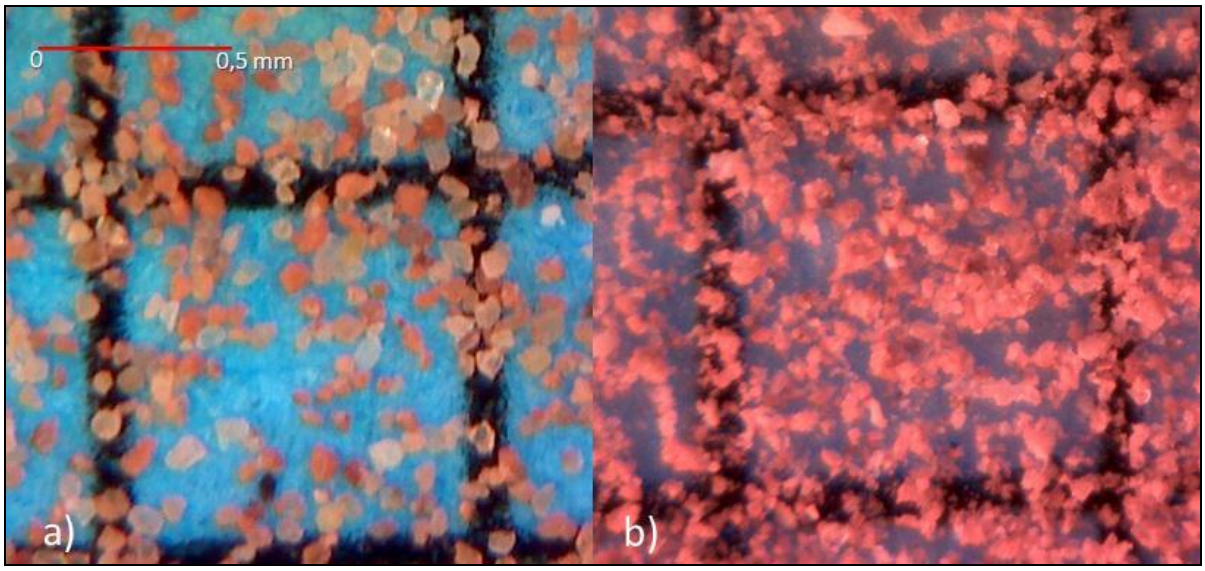

Figure 12. Selected pictures comparison. a) Selected Micro picture Sample C2-23 (single grains) b) Non Selected Micro picture C2-2 (aggregates)

The first step to obtain the grain size distribution consisted in scaling the images (8-bit full color) of 612X612 pixels based on the reference grid. Next, the images were converted to binary images by using the command *detection*. This procedure was carried out over all the preselected images and from these only 14 images from Crevasse Splay 2 gave consistent binary data to be analyzed. Based on such binary images, using commands like segmentation, erosion, dilation or/and logic operations, single grains were distinguished (Fig. 13). Over such grains, spatial characteristics such as area, perimeter, length, breadth, roundness, and aspect ratio were measured. This information was saved and converted to an excel file to be analyzed for grain size frequency distribution. After that, several filters were used to get a better grain size distribution. For instance, grains with roundness values and aspect ratio larger than the mean grain size were excluded from the analysis. This filter was based on the idea that grains with high aspect ratio and roundness tend to be aggregates or salt crystals formed after crevasse splay deposition.

Table 3. Micro-pictures selection for imaging Analysis.

Crevasse Splay 1		*Crevasse Splay 2*			
Sample	Picture	Sample	Picture	Sample	Picture
C1-0	C1-0-6	C2-2	C2-2-1	C2-14	C2-14-1
	C1-0-7		C2-2-2		C2-14-2
C1-3	C1-3-3		C2-2-5		C2-14-4
C1-14	C1-14-13		C2-2-6	C2-16	C1-16-2
	C1-14-14	C2-5	C2-5-1		C1-16-5
	C1-14-15		C2-5-5		C1-16-6
C1-16	C1-16-6		C2-5-6	C2-18	C2-18-2
	C1-16-7	C2-10	C2-10-2		C2-18-4
	C1-16-8		C2-10-3		C2-18-5
C1-20	C1-20-1	C2-11	C2-11-1		C2-18-6
	C1-20-2		C2-11-4	C2-19	C2-19-1
	C1-20-8		C2-11-5		C2-19-3
	C1-20-9		C2-11-6		C2-19-4
C1-22	C1-22-6	C2-12	C2-12-3		C2-19-5
	C1-22-7		C2-12-4		C2-19-6
C1-25	C1-25-1		C2-12-5	C2-21	C2-21-1
	C1-25-2		C2-12-6		C2-21-3
	C1-25-6		C2-12-7		C2-21-4
C1-26	C1-26-1		C2-12-8		C2-21-5
	C1-26-2	C2-13	C2-13-2	C2-23	C2-23-1
	C1-26-5		C2-13-3		C2-23-3
C1-27	C1-27-1		C2-13-6		C2-23-4
	C1-27-2				C2-23-7
	C1-27-5				

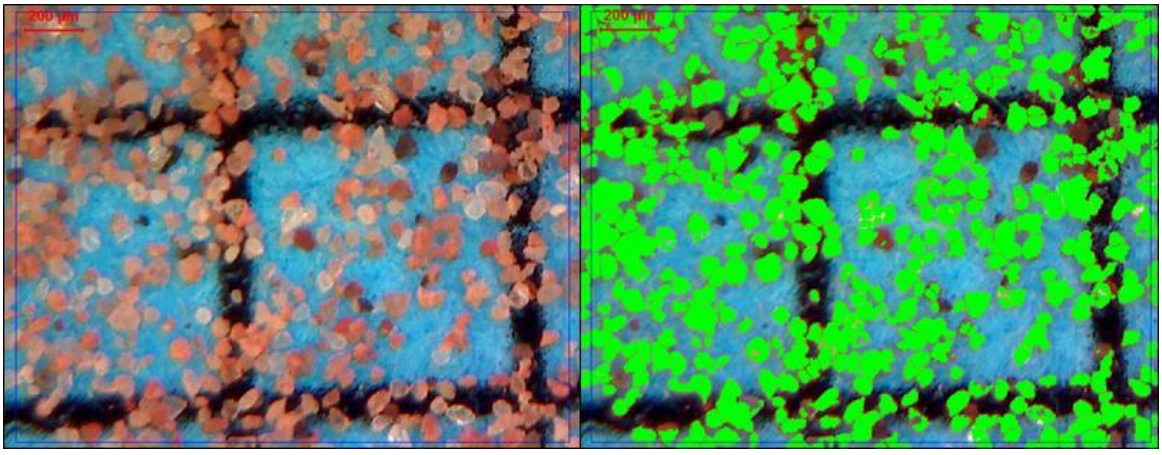

Figure 13. Grain size detection and identification of single grains. Sample C2-23

After filtering the initial results, the diameter of all the features was obtained based on the theory that individual grains with low aspect ratio could be treated as spheres. The grains diameter were derived from their perimeter, giving a grain size frequency distribution (Fig. 14). Summary statistics like mean and standard deviation were extracted from the frequency distributions to characterize properly each sample (Table 4).

Table 4. Summary of mean and Standard deviation samples crevasse splay 2.

Crevasse Splay 2		
Point	**Daimeter Mean (um)**	**Standart Deviation (um)**
C2-3	144	56
C2-5	41	29
C2-6	57	28
C2-8	56	42
C2-9	73	43
C2-10	70	27
C2-11	95	39
C2-12	57	33
C2-14	59	23
C2-18	44	16
C2-19	63	23
C2-20	66	19
C2-21	51	23
C2-23	74	31

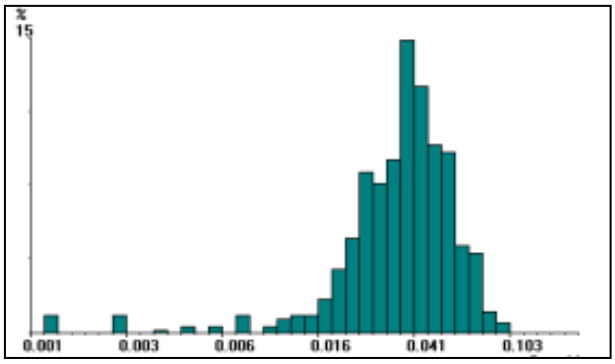

Figure 14. Frequency distribution plot (mm). Sample C2-14

2.2. Laser Analysis

Samples from Crevasse Splays 1 and 2 were sent to the grain size laboratory to determine more accurately their particle sizes, due to the low quality of the micro pictures and their results. Those samples were analyzed under a laser granulometer (Fig 15) - Helos KR Sympatico -. This device works on particles between 0.1 µm to 2000 µm, based on the Fraunhofer diffraction theory (Blott, Croft, Pye, Saye, & Wilson, 2004) .

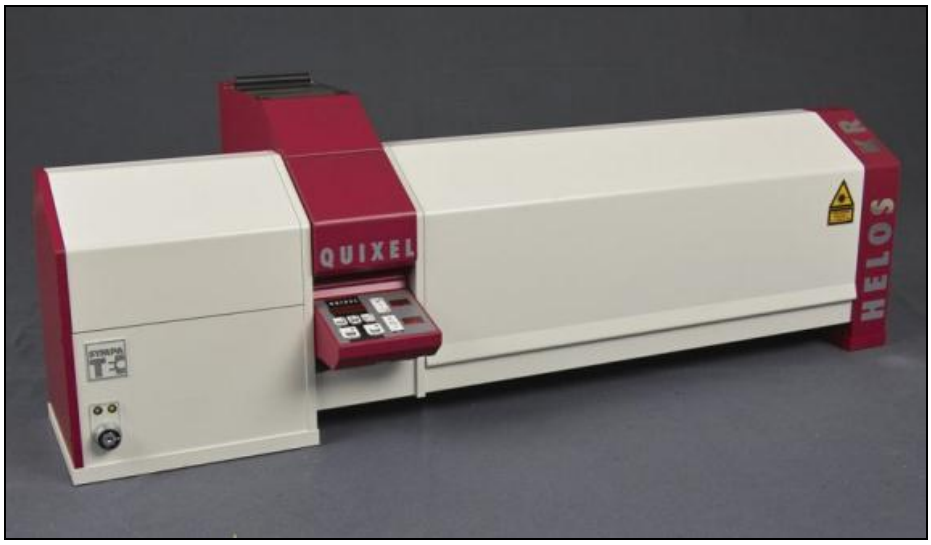

Figure 15. HELOS/KR with advanced wet disperser.

The principle of laser diffractometry consists in detecting diffracted light (Blatt, 2000), which is generated by a laser and magnify with an optical system (Fig. 16). Such system consists of an array of several lenses, which amplify the laser beam and illuminates the whole sample. The particle samples

are put in suspension in a vessel with water, which due to the Fourier lenses diffracts the light that pass through many identical particles at different locations to the detection rings on the detector. Then, the detected intensities are recorded into a PC, which under a Microsoft Windows system analyses the raw data acquired.

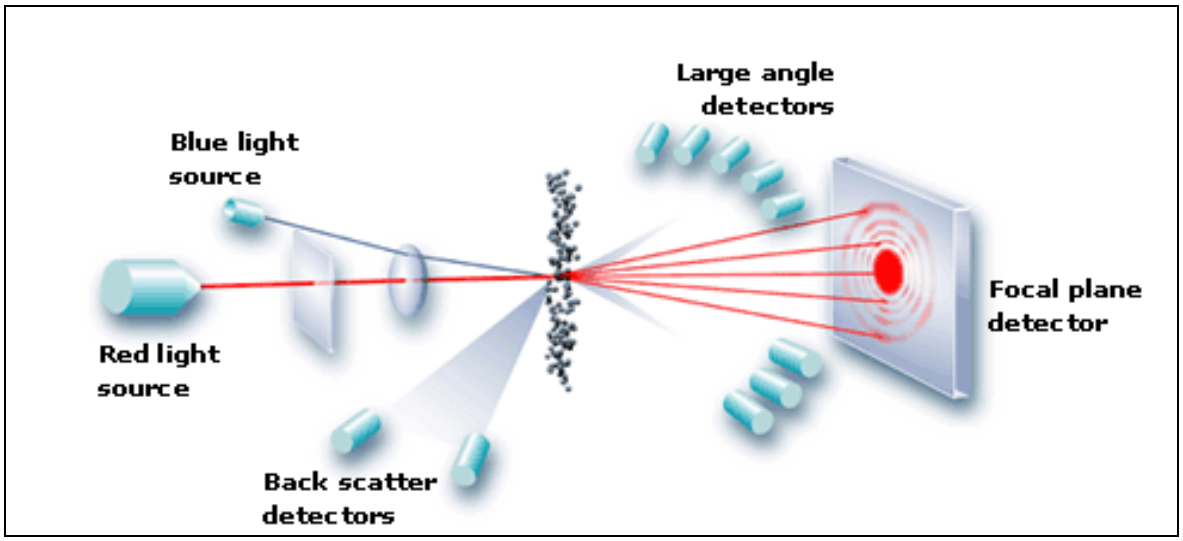

Figure 16. Laser Diffraction particle Sizing (www.marvern.com).

To carry out a laser grain analysis many different preparations and conditions are conducted to the samples of study. In this research in order to build a high definition 3D grain size model, it is necessary to obtain the most accurate grain size measurements. Therefore, it is required to reduce as much as possible the unwanted fractions (organic matter) in the sample, which require acid pre-treatment (Blott, Croft, Pye, Saye, & Wilson, 2004). In the same way, the degree of accuracy of the laser technique depends on the amount of sample used. The laser intensity passing through the sample is inversely proportional to the volume of sample. So, as much sample you add as much degree of obscurity you get from the detectors, which impacts the results of the grain size measurements. In Fourier systems like the HELOS systems, the recommended degree of obscuration varies between 8 – 12%, which in terms of sample weight is in-between 0.2 to 4 grams.

The samples acquired during the fieldwork belong to continental sediments, which implies an acid pre-treatment, due to the their main cement components are organic matter and carbonates. These unwanted components can be partially removed by adding either hydrogen peroxide and/or hydrochloric acid (Sun, et al., 2002). The expected grain sizes are below fine sand ranges according to the mean grain size obtained in the image analysis. This leads us to use a small volume of sample because finer sediments cause large obscuration. A brief description of the procedure performed is described below (Blott, Croft, Pye, Saye, & Wilson, 2004):

- Register the samples in 'Lab-Archief' and select the option KG that is referring to Grain Size Analysis.

- Put 1-2 g of sediment samples in a vessel of 800ml (high model), in order to achieve an adequate beam obscuration.

- Carry out an oxidation reaction using 5 ml of 30% H_2O_2. Avoid boiling to dryness by using some demineralized water. After the first violent reaction is finished, fill the level up to 100 ml with water and boil it until all the peroxide is removed (Fig. 17). Keep level between 50-100 ml. For samples with significant content of organic matter filter the big pieces and repeat the oxidation process.

- Cooling down until 40˚C.

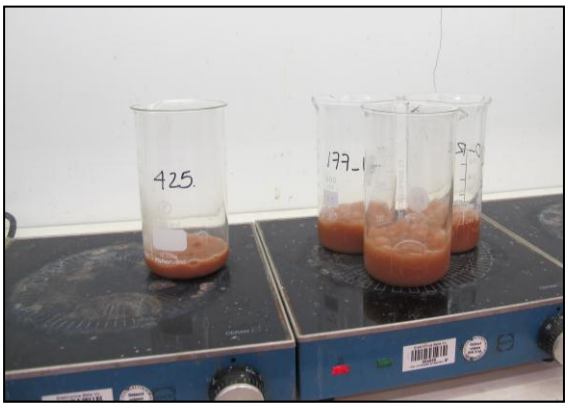

Figure 17. Oxidation Reaction to remove organic matter by using H_2O_2

- Cleaning (rinse) the walls of the beaker and avoid to reach more than 100ml of mixing water.

- Adding 10 ml of HCl 10%. If the reaction is too violent, more acid must be added. Then fill the beaker with water until 100 ml.

- Bringing the mixture to boiling point. Then boil it for no more than one minute.

- Cooling down and clean the walls of the beaker to avoid loss material. After cooling down, fill the beakers until the top with water and leave them to decant overnight.

- After decantation, absorb the water until its level gets to approximately 50ml, the suspension is filled up to 100 ml. About 300mg $Na_4P_2O_710H_2O$ is added. Heat the samples until the boiling point is reached, but boil no longer than one minute.

- After cooling, the samples can be measured on the Helos KR.

After placing each sample into the Helos KR, the grain size was measured, and a compile file (appendix 2) of information regarding to the mean, standard deviation, skewedness and kurtosis among others was created. In the same way, a frequency plot was created in order to see graphically the characteristic distribution of each sample. Few samples were randomly chosen in order to do a reliability test, which shows that the results vary 1% from the previous measurements.

3. Field Data Interpretation

After the field data acquisition was carried out, it is necessary to analyze and interpret such information to build a geological conceptual model of the crevasse splays. This model consists in a structural model, which will be defined by the thickness distribution and the facies model. This in turns is based on the field observations and the lacquer peels acquired in the field. The result of this model will be used as a source data for understanding the grain size model described in the next chapter.

3.1. Structural Model

The structural model consisted in the integration of a pillar grid and a facies model. A pillar grid is associated with the structure that will be modeled and it is usually composed by the limits of the model (main faults). The second component is the facies model, which reflects the vertical and lateral extension of particular characteristics of the reservoir units or formations under study. In this case, the structural model differs to the typical models in how the boundaries are characterized. In crevasse splays, these limits are not defined by faults or any tectonic control but by environmental controls. In other words, the limits of the model are demarcated by the crevasse splay edges defined by fake color satellite images. Finally, the facies model will be created based on the field observations and the analyzed data from lacquer peels.

3.1.1. Pillar Gridding

In order to create a pillar grid is necessary to set up the upper and lower boundaries of the model, which in turns are laterally limited by the edge of the crevasse splays. So, the lower limit for each crevasse splay will be assumed as the reference level (zero). This limit was defined in every sample point by lithological differentiation that turns in the contact between the flood plain, which is composed mainly by mud, and the crevasse splay itself, which is composed mainly by silt sediments. This differentiation was based on color changes of the units (Fig. 18) in which the silt sediments are represented by a yellowish unit, while a dark brown layer characterizes the mudstone unit. At the trenches, the base of the crevasse splays were defined under the criteria that the flood plain does not show any sedimentary structure, while the crevasses clearly show sedimentary structures such

as climbing ripples, planar lamination, cross lamination, etc. (Fig 19). The upper limit of the model was defined by measuring the total thickness of the crevasse splays from the reference level to the ground surface.

After the crevasse splay thickness in one flooding event was defined and re-checked on the lacquer peels available, isopach maps of both crevasse splays were generated by using Petrel (Appendix 3). Consequently, the upper surface was generated using the base of the crevasse splays and the isopach maps to create a pillar grid for each crevasse splay.

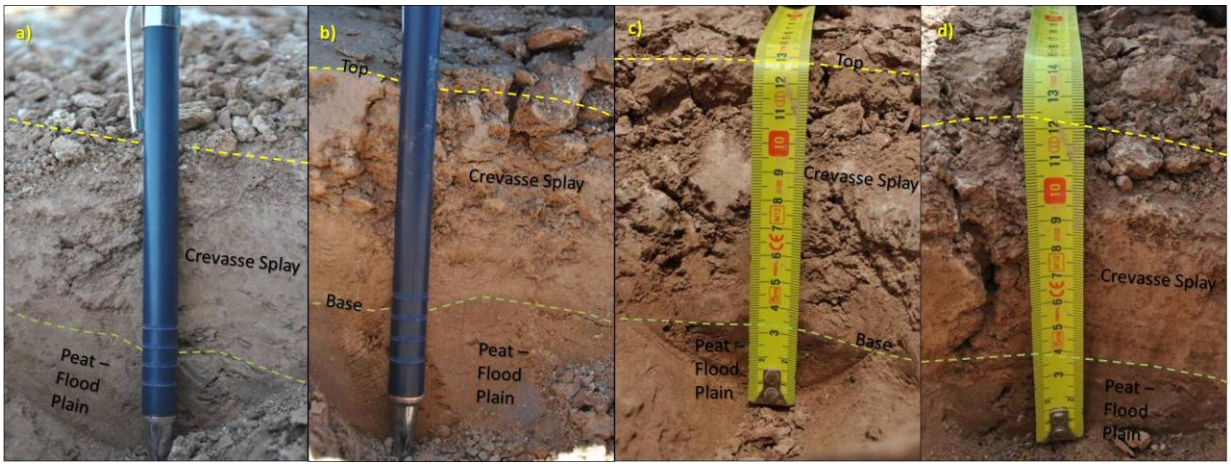

Figure 18. Thickness Definition. a) Crevasse Splay1_Sample-18. b) Crevasse Splay 1_Sample-8. c) Crevasse Splay2_Sample-8. d) Crevasse Splay2_Sample-12.

The pillar grids show that the crevasse splays exhibits a particular spatial distribution linked to the main characteristics of the splays at the development stage I described by Smith, 1989. We can see from the satellite images that both crevasse splays have a lobate shape in a map view (Appendix 1) that is characteristic for the Stage I splays. The Crevasse Splay 1 exhibits a wedge-shape body oriented parallel to the direction of the sediment flux (O'Brien & Wells, 1986) and a lens-shape body perpendicular to the flow (Fig. 20). Section (a) shows that the Crevasse Splay 1 is thicker at the proximal areas and gets thinner gradually toward the distal parts, suggesting low energy levels in such areas. Section (b) shows that the crevasse splay gets thinner from its axis to its edges. This reaffirms that the thickness of such bodies in one single flooding event are mainly controlled by environmental conditions and the waning process (Johansen, 1983).

3.2. Facies model

The second component of the structural model is the facies distribution. Here, we will describe the facies observed in the trenches and based on such information a facies model will be developed on each crevasse splay. Regarding to the facies information on the Crevasse Splay 1, we obtained 1 good quality sedimentary log (Appendix 4) out of 4 lacquer peels obtained in the area.

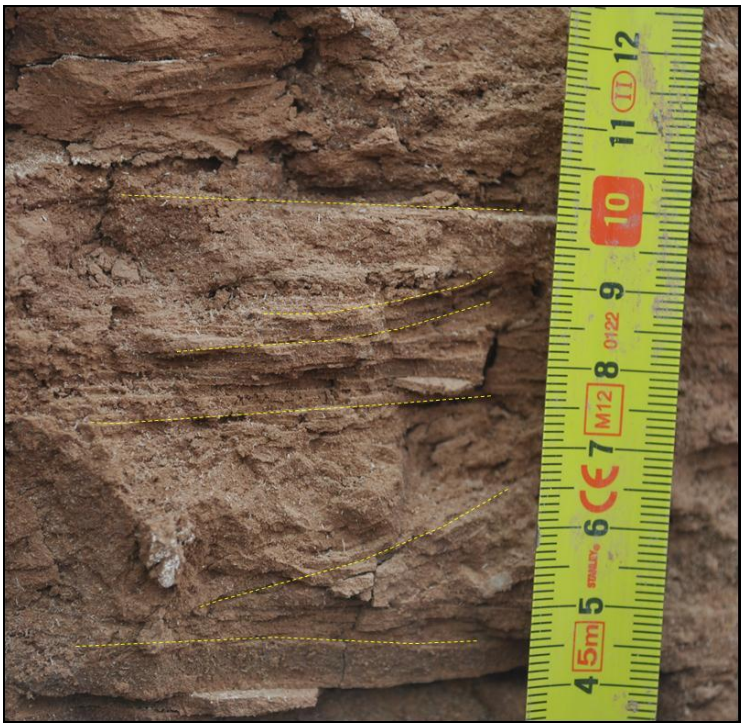

Figure 19. Sedimentary Structures present along Crevasse Splays.

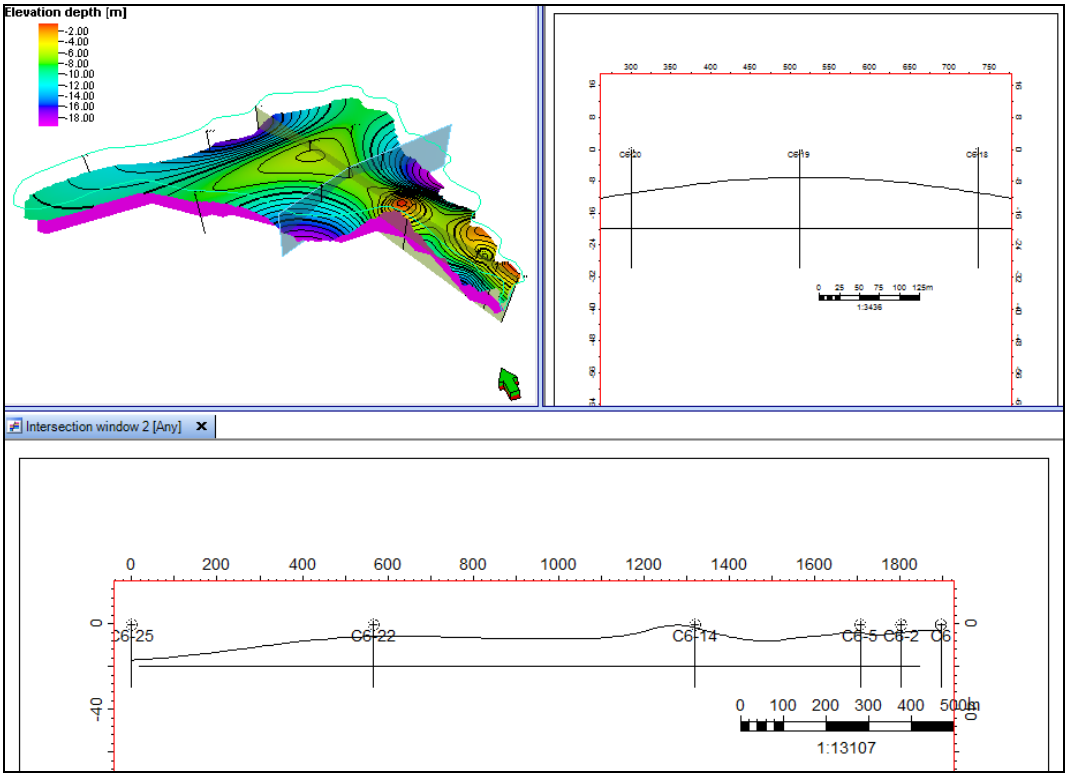

Figure 20. Cross Sections Crevasse Splay 1. a) Section parallel to progradation. b) Section Perpendicular to Flow direction.

Besides the sedimentary logs, field descriptions and pictures at the trenches were used to describe the main sedimentary facies at such locations, instead of the poor data obtained from the lacquer peels. On the Crevasse Splay 2, the lacquer peel acquisition gave 4 good quality sedimentary logs (Appendix 4). These together with the field data descriptions and the pictures of the trenches provide enough information to describe the facies of the sediment body.

In general terms, two main facies were found by associating particular sedimentary structures and grain size. However, it is important to remark that grain size was not linked completely to the facies differentiation because of the difficulty of identifying vertical grain size trends by naked eye. From bottom to top, the lower facies are defined by silt sediments deposited in a moderate to low energy environment. This fining upwards sequence is characterized by a sporadic cross lamination at the bottom (Fig 21 – Appendix 4), which vertically turns into climbing ripples (Fig 22 – Appendix 4) with moderate climbing angle. The cross laminated sediments are truncated by shallow scours dipping upstream that can be the result of flute-like erosion of in-homogeneities on poor cohesive beds (van Gelder, van den Berg, Cheng, & Xue, 1994).

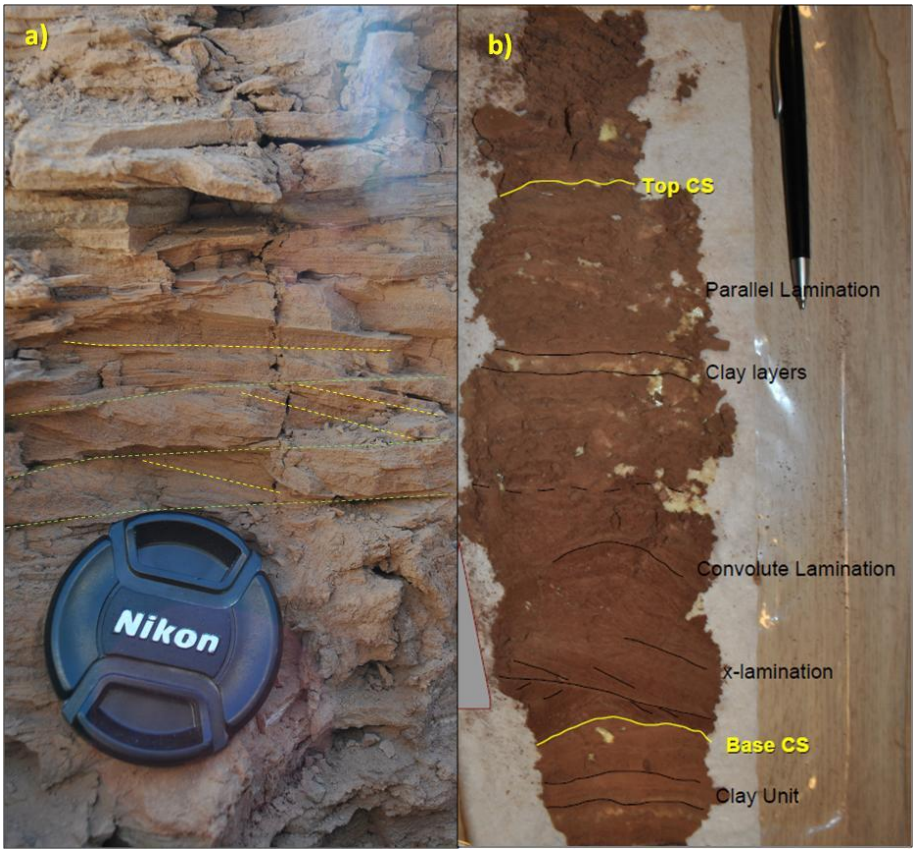

Figure 21. Cross laminae Silt facies. a) Crevasse Splay 1 Sample 14. b) Crevasse Splay 2 Sample 23.

These scouring surfaces can be associated to low angle cross lamination and horizontal even laminations, which could be deposited in high flow velocities according to van Gelder (1994).

Figure 22. Climbing Ripples Silt facies. Crevasse Splay 2.

The second group of facies found is defined by a wavy laminae fining upwards sequence, whose lower limit is not clearly defined in vertical section. This facies can be recognized by wavy and horizontal laminations (Fig. 23 – Appendix 4), which are the result of the waning process acting over the climbing ripples at the former facies (Johansen, 1983). These structures can be related to low flow regime. This regime can be distinguished by the increasing angle of the climbing ripples that degenerates into wavy and horizontal lamination when the migration stops. The latter can be linked to the suspended load conditions (van Gelder, van den Berg, Cheng, & Xue, 1994).

These facies are strongly related to each other because both are result of the waning process that implies flow deceleration. The reduction of the flow velocity has been tested in several experiments on sediments by Banerjee (1977), who explain that slow deceleration results in a particular sequence of sedimentary structures. These structures from bottom to top are parallel lamination ripples that went from steep short forms to sinusoidal ripple lamination and ending with a suspension blanket. Therefore, the similarity of this sequence and the observed sequence (Fig. 24) might explain the facies distribution along the crevasse splays in terms of energy regimes.

Once the facies were defined at trenches, a facies model in Petrel was constructed having in mind the energy regimes. The first step to construct the model consisted in the generation of a forward model, which was based on the facies descriptions and analogue crevasse splays described in the literature (e.g. McCabe, 1987; Farrell, 1984; Smith, 1989; Farrell, 2001).

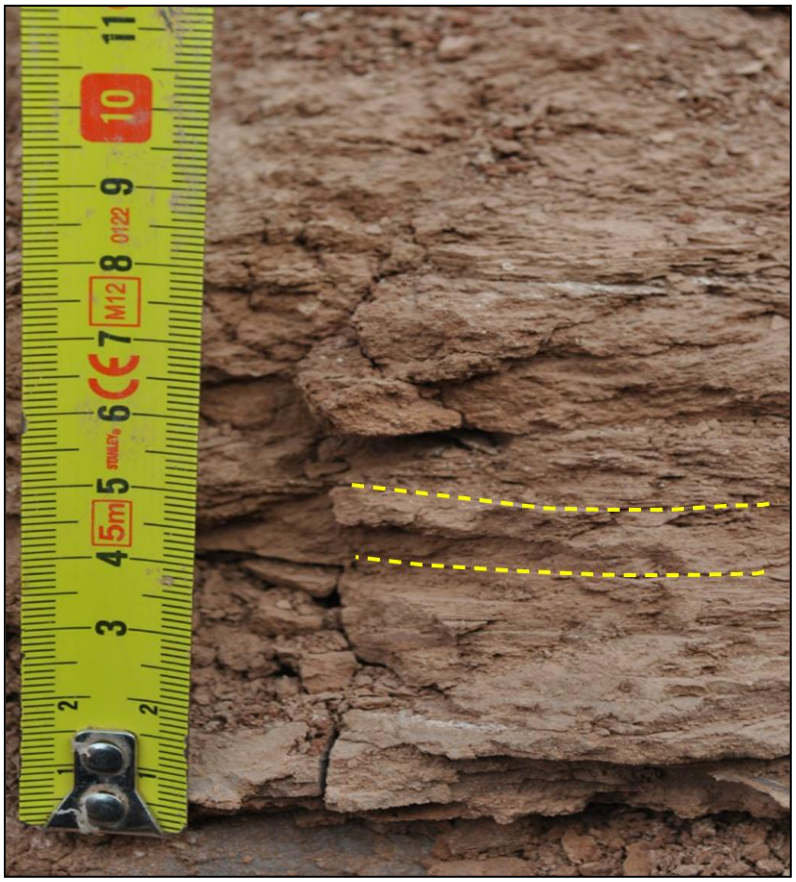

Figure 23. Wavy and Horizontal laminae Silt facies. Crevasse Splay 2

Based on this, Crevasse Splay 1 (Fig. 25) shows that thick cross-ripple silt laminae facies are present in the center and proximal part of the crevasse splay. So, as we move towards the distal areas, the thickness of this facies gets thinner until it disappears. Likewise, the wavy-horizontal silty clay facies are encountered over the whole crevasse splay. This facie is represented by a thin layer in the proximal areas, which becomes thicker to the terminal areas of the sediment body. Such distribution can be associated to the geomorphological evolution of a crevasse splay stage I, (Farrell, 2001) in which a main channel levee is breached and a small distributary mouth bar is formed on the flood plain. This distributary mouth bar is correlated to the cross laminae silt facies that are filling up the depression caused by the feeder crevasse.

These deposits were buried by wavy laminae silty clay deposits (marginal bar deposits) due to the flow deceleration. The wavy laminae silty clay deposits in turns act as levees along the feeder channel aggrading until they reach the local base level burying the cross laminae deposits. Moving toward the end of the channel splay, the flow becomes unconfined letting that the suspension deposits spread out toward the margins of the crevasse splay as wavy silty clay deposits.

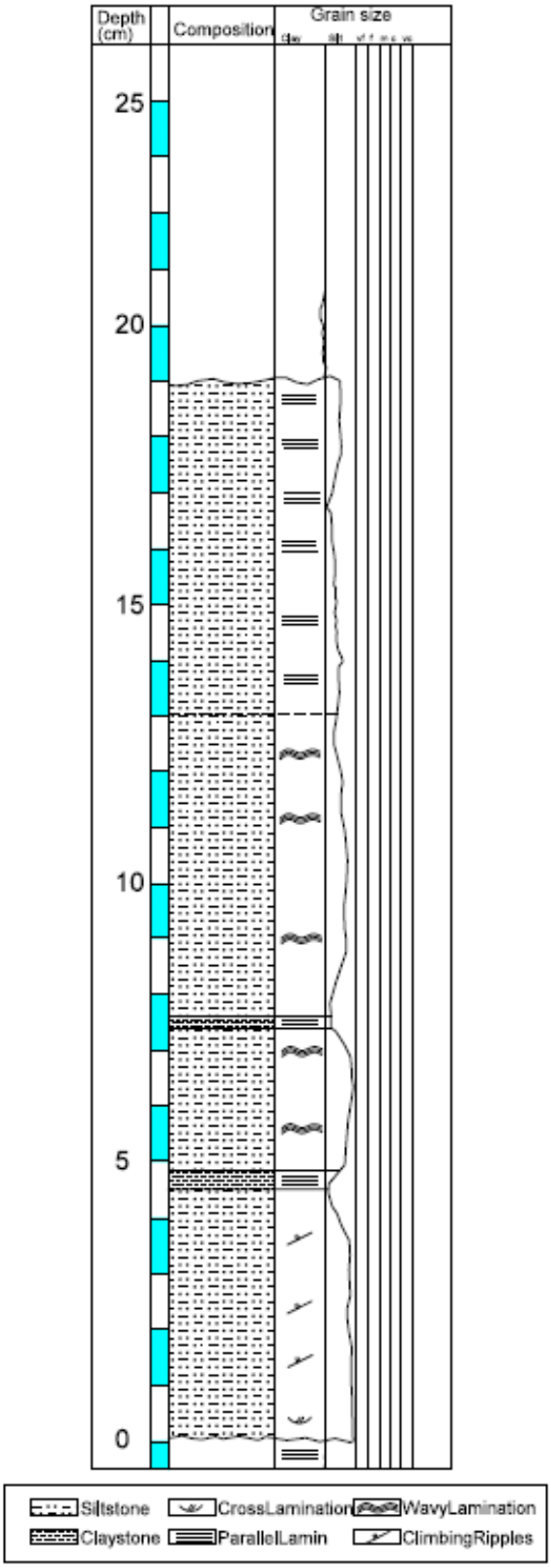

Figure 24. Sedimentary Log. Crevasse Splay 2 - Location 1.

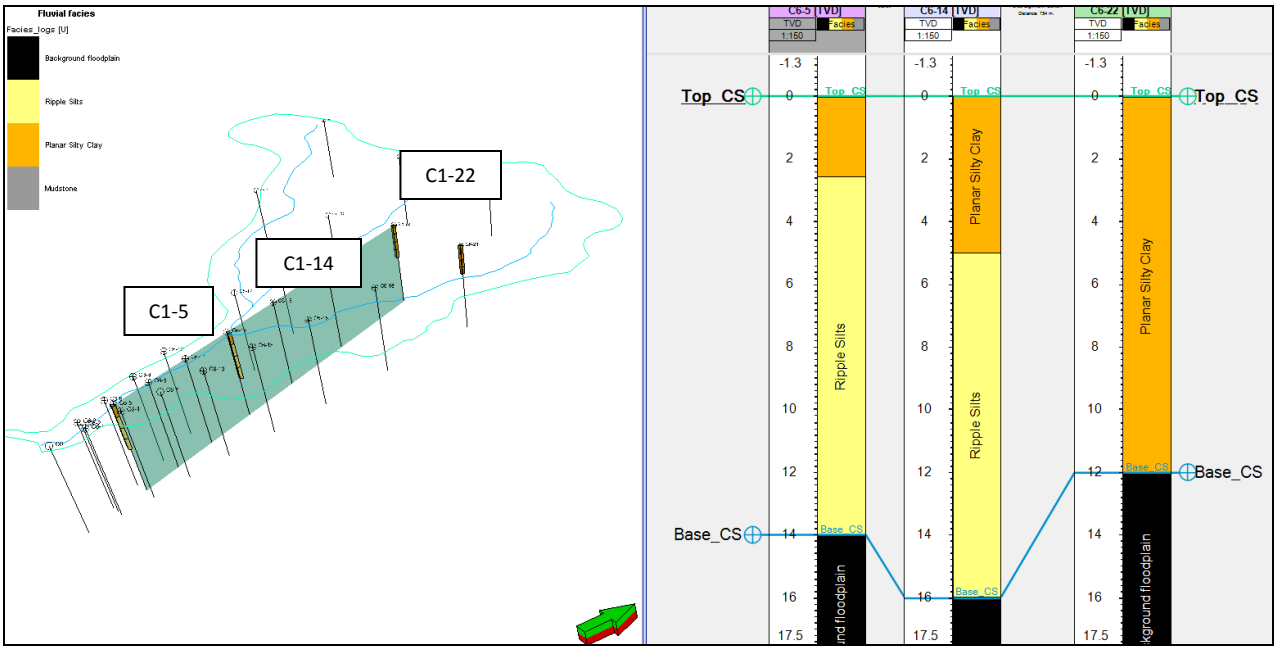

Figure 25. Cross Section parallel to the flow direction along the Crevasse Splay 1.

The second step to construct the facies model consisted to discretize the facies observed in the trenches and distribute them over the whole crevasse splays using different interpolation techniques. These discretized facies were upscaled in order to have a better geological distribution over the area. With the upscaled facies and using different modeling approaches such as truncated sequential Gaussian distribution with trends, object based modeling, etc., several realizations were produced based on the forward model.

The result of the facies modeling is shown in the figure 26. This shows that the cross laminae silt facies (in yellow) are deposited mainly in the proximal area, where the feeder channels can be developed (Fig. 26d). As the flow is waned, the beds become more laminated and horizontal (Johansen, 1983) represented by wavy-horizontal facies (in orange). In a vertical section, the cross laminae facies are thicker close to the source area (Fig 26b) and as we move towards the edges (Fig 26c), it becomes thinner.

Besides the facies distribution of a crevasse splay deposited in one flooding event, another flooding event formed before deposition of the crevasse splay under study was recognized at some trenches. This flooding event can be distinguished from the previous one by a sporadic mud layer (Fig. 27), along the crevasse splays (Johansen, 1983). This finding suggests that the crevasse splays behave similarly to the mouth of deltaic distributary channels prograding into quiet water resulting in progradational lobes.

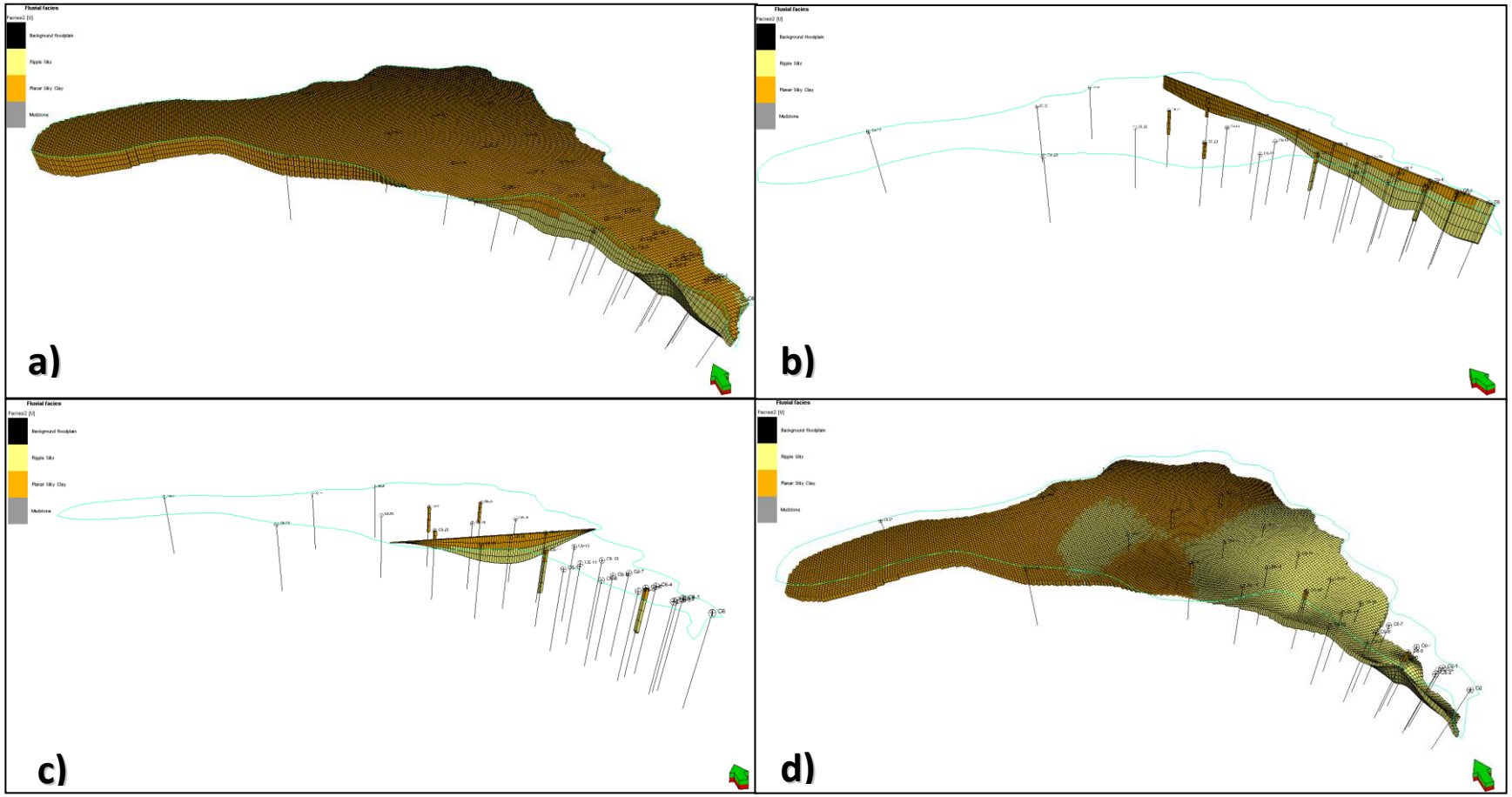

Figure 26. a) Facies Model Crevasse Splay 1. b) Cross Section along the axis of the Crevasse Splay facies model. c) Cross Section perpendicular to the axis of the crevasse splay facies model. d) Bottom layer of the crevasse splay facies model. In yellow cross laminae Silt Facies. In orange wavy-horizontal laminae facies.

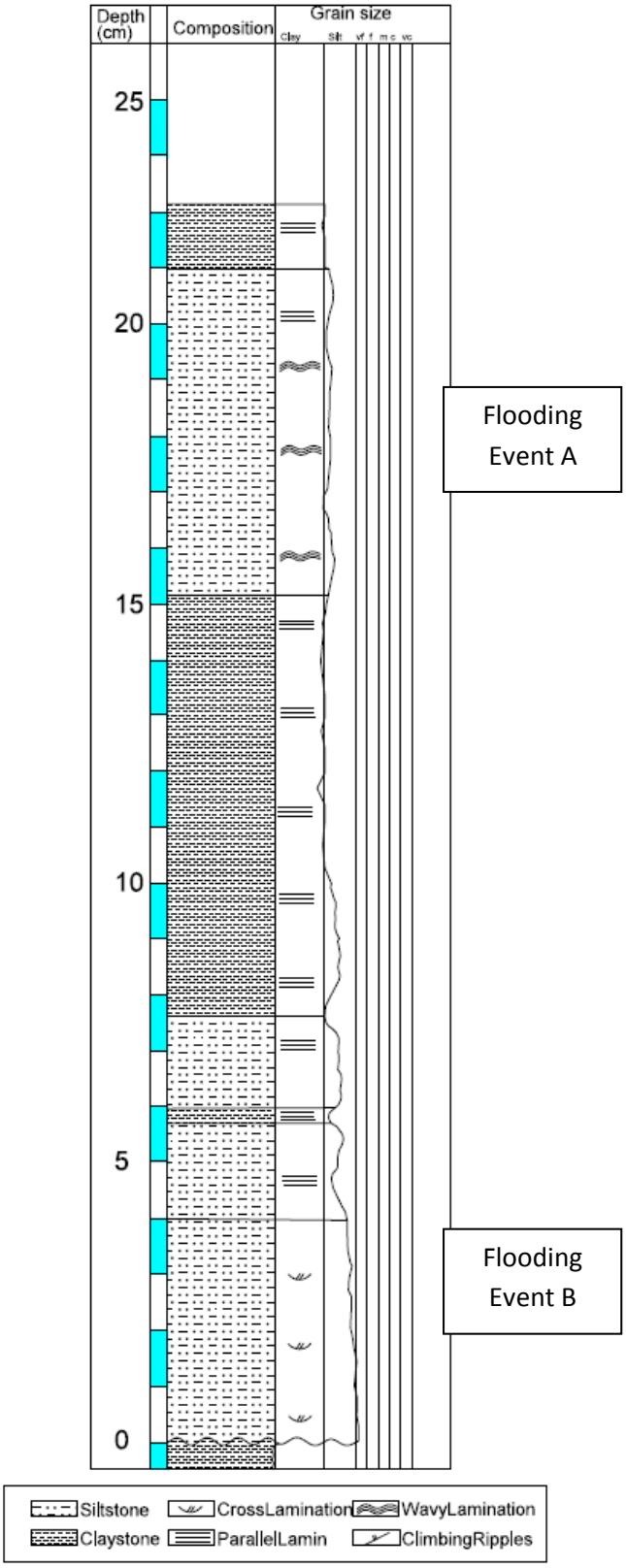

Figure 27. Sedimentary Log Crevasse Splay 2 - Location 19. Flooding events separated by a mud layer

4. Grain Size Modeling

In chapter 2, we explained how the sediments samples were obtained along the crevasse splays near Uyuni town. This chapter will explain how the grain size data were analyzed and how its results were used as one of the main inputs of the grain size model. In the same way using the grain size data, we will show its relationship with the main processes that were involved during the formation of the crevasse splays in a low gradient basin. These processes are the key factor in the grain size distribution along such sediment bodies. Besides the genesis of the crevasse splays, the grain size data will be correlated with physical features present in satellite images, such as channels. In addition, it will be show how to use these features as a parameter of a high-resolution grain size model. Finally, we will show the procedure implemented to correlate features such as channels with RGBD data from satellite images and based on these correlations, it will be describe how to improve the high-resolution model.

4.1. Grain Size Data Analysis

As was mentioned in chapter 2, the samples collected in the Crevasse Splays 1 and 2 were analyzed by two different methods. The first method consisted in analyzing pictures of the samples and the second consisted of obtaining a grain size distribution of each sample by using a laser particle sizer. The results of both methods were analyzed using summary statistics, frequency distributions and cumulative distributions. Due to the results, the methods were compared to each other showing which of both methods better represents the grain size distribution along the crevasse splays.

The image analysis method shows that 14 samples out of 56 samples gave appropriate results, while with the laser analysis method, all the samples collected in the field were analyzed giving 56 results. The results of the image analysis showed that the grain size of the collected samples varies between 51 μm and 144 μm, which is on average too high for this type of deposits. According to the literature, crevasse splays are dominantly silty (<65um) (Marshak, Kuykendall, & Zhixiong, 2011). In contrast, the mean grain size of the samples analyzed by the laser particle sizer showed (Fig 28) that the bulk results varied between 6 μm and 9 μm, which belong to a more realistic silt and clay range.

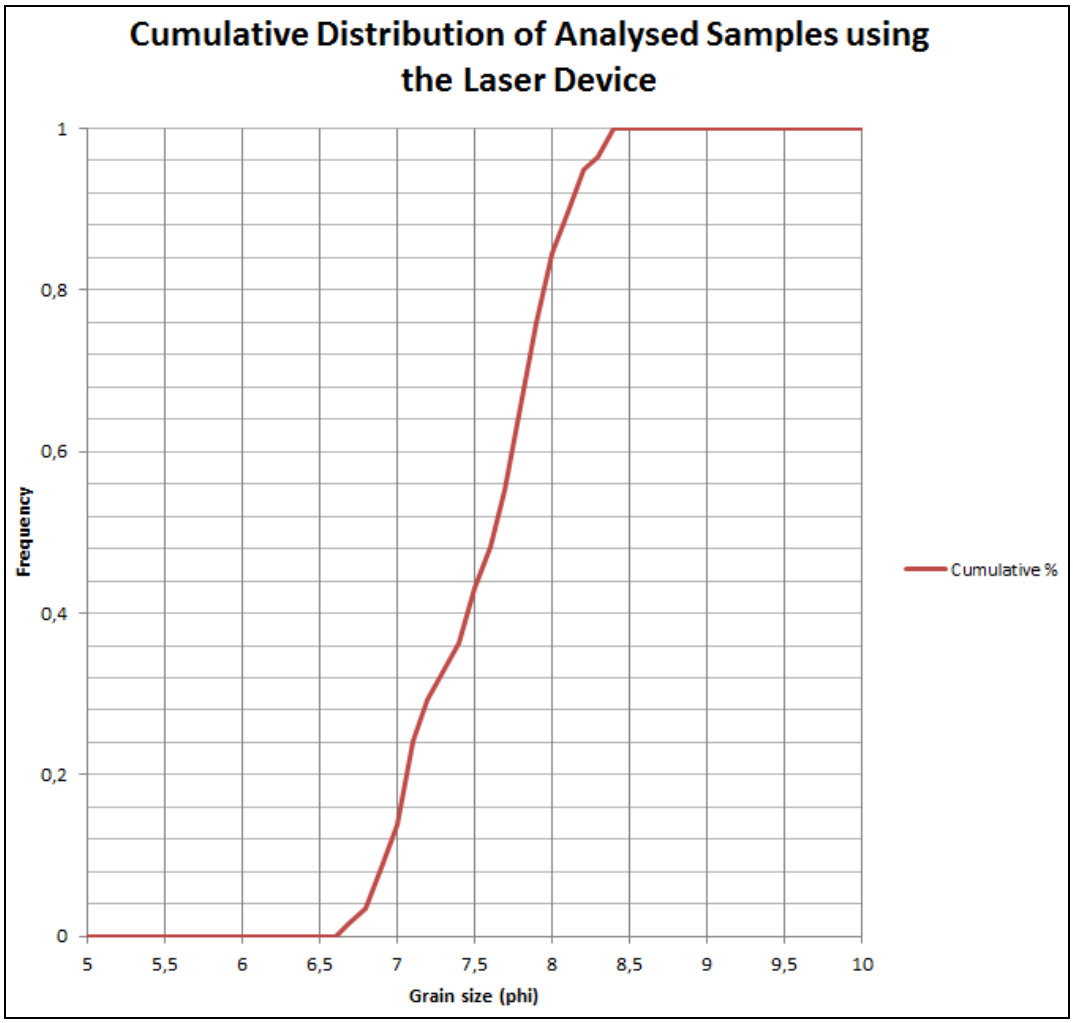

Figure 28. Cumulative distribution over crevasse splays sampled.

Based on the results of both methods and the uncertainty about the amount of information obtained, the results from the laser analysis was used to describe the grain size distributions. Therefore, this data is going to be analyzed in detail in the next sections in order to show how to build up a model that faithfully represents the nature of the crevasse splays.

4.1.1. Analysis of Raw Data

The raw data (Fig. 29) shows that the sediments are polymodal, composed by at least three different components (Sun, et al., 2002). A first component goes from 0.5 µm to 20 µm, a second component that varies between 2 µm to 30 µm and a largest component that runs between 30 µm to 100 µm. According to the literature, these polymodal distributions are related to different transport mechanisms, which usually are identified in aeolian and hydraulic sediments systems (Ashley, 1978; Middleton, 1976). The principal mechanisms and processes that are operating in hydraulic sedimentary systems are suspension, saltation and traction, (Sun, et al., 2002) all of which are related to the particle size. Therefore, it is necessary to sub-divide the grain size frequency

distribution of each sample into components in order to understand how the whole sediment body was formed and what kind of processes governed their formation (Weltje & Prins, 2007).

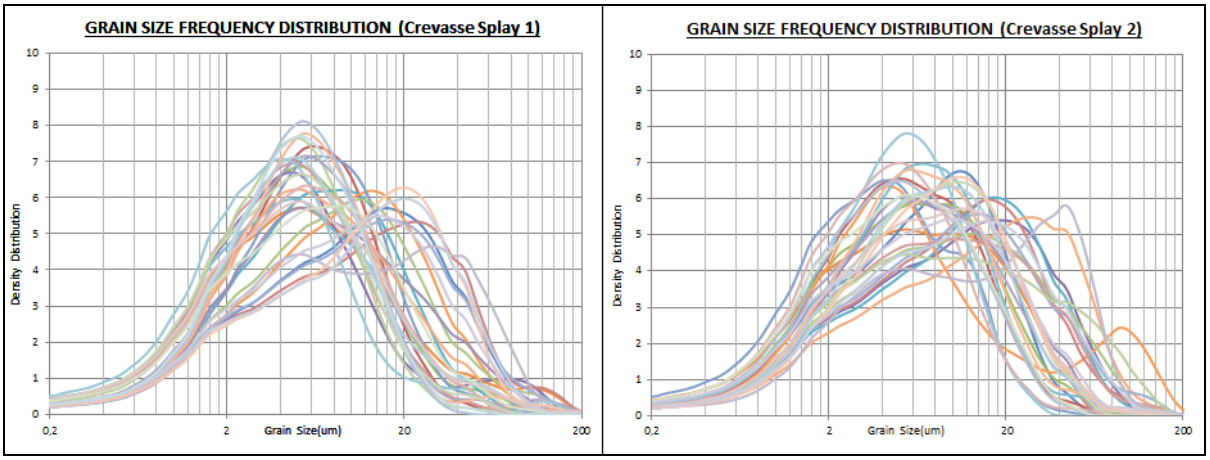

Figure 29. Grain size Frequency distribution of Crevasse Splay 1 and 2 from laser analysis.

Another issue that should be considered to comprehend the crevasse splays formation is the spatial distribution of the mean bulk grain size and its respective components. By this means, it is possible to see if there is any process related to the areal particle distribution. For instance, a simple mapping of the median size from the raw data shows (Fig. 30 – Appendix 5) that the grain size seems to decrease radially (from 8 µm to 3 µm). These low values could be related to the result of a mixing process acting over different components.

4.1.2. Grain Size Partitioning

4.1.2.1. Methodology

In order to understand the results of partitioning components that are mixed in one frequency distribution is necessary to explain briefly the methodology applied to this data and how its results can be interpreted.

The first step consists in determining the sedimentary components that are present in a sediment sample. The best way of validating the component determination is by a fitting experiment. This consists in fitting different theoretical distribution functions such as *Normal, T, Poisson* and *Weibull* with the raw data by changing the number of components present in such distributions. In this study, we will describe the Gaussian Function and the Weibull Function that are the most well-known curves in the literature (Sun, et al., 2002; Weltje & Prins, 2007).

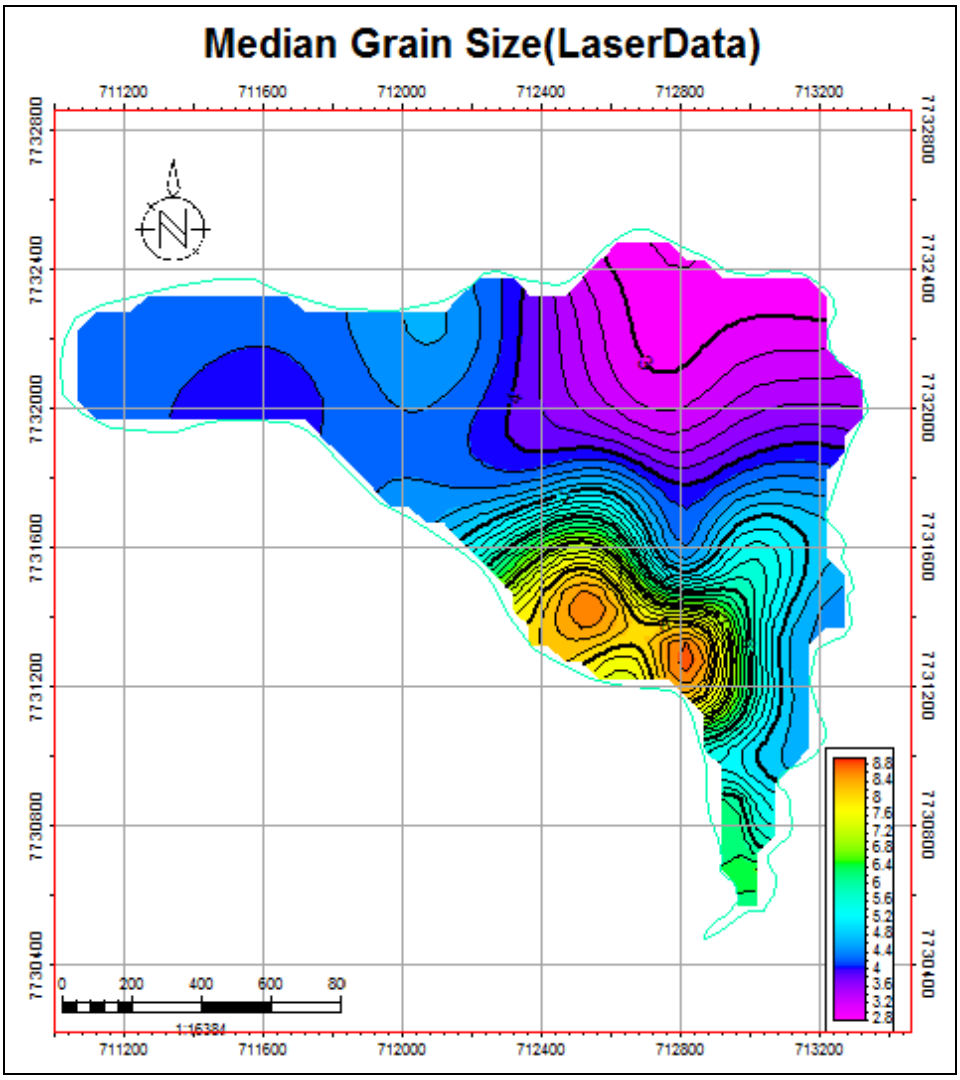

Figure 30. Median Grain Size Map – Raw data from laser analysis - Crevasse Splay 1.

The Gaussian function is a symmetric function that can be expressed in the following terms:

$$f(x,\mu,\sigma) = \frac{1}{\sqrt{2\pi\sigma}} * e^{-[\frac{(x-\mu)^2}{2\sigma^2}]}$$

Where μ (phi scale) is the mean, σ (phi scale) is the variance and x represents the grain size (phi scale), this function has been used to describe the statistical moments of grain size distribution such as mean and variance.

On the other hand, we have the Weibull function, which is known because of its flexibility and can be described as:

$$f(x,\alpha,\beta) = \frac{\alpha}{\beta^{\alpha}} * x^{\alpha-1} * e^{-(\frac{x}{\beta})^{\alpha}}$$

Where α is the shape parameter, β is the scale parameter and x is the grain size (μm). This function can be skewed to any direction depending of specific parameters. Due to its benefits over the other functions, the Weibull function is used worldwide in many different fields such as meteorological statistics (Sun, et al., 2002).

After choosing the function to perform a curve-fitting, then the mixing theory (Weltje & Prins, 2007) is applied to the raw data. This theory is based on the idea that an universal distribution can be determined by the sum of the product of each prototype function of the component times their respective percentage, as it is expressed in the following equation:

$$f = p_1 f_1 + p_2 f_2 + p_3 f_3 + \cdots + (1 - p_1 - p_2 - p_3 - p_{n-1}) f_n$$

For example, if a bulk distribution is bimodal with a coarse grain size component and a silt grain size component, then the representative resulting Weibull function will be described by five parameters α_1, β_1, α_2, β_2, and m. The first two parameters are the shape and the scale, which will describe the coarse grain size distribution. The third and fourth parameters will describe the silt distribution mode and finally the m parameter will give the representative percentage of the coarse component. These variables can be obtained by setting the squared of the residual error (or residual error standard) to cero during the fitting of the raw grain size data.

4.1.2.2. Description of Results

The results (statistical moments) that are going to be described in this section were obtained by fitting the raw grain size data with the Gaussian function and the Weibull function. In order to establish which of these statistical moments could describe most accurately the distributions and which function works better on these kind of sediments, the results will be describe and compare in the next section.

4.1.2.2.1. Function Validation.

In order to know which results describe better the grain size distribution and how many components are present, the squared residual error given by the fitting experiment of the Gaussian function and the Weibull function were compared. The first fitting experiment was done assuming that all samples had two components. A second fitting experiment using three components was carried out on the samples were the number of components were uncertain. In the first experiment, the Weibull function gave lower squared sum of residual error values than the Gaussian function (Table 5). This behavior was seen in twenty-two (22) out of twenty-eight (28) samples over the Crevasse Splay 1 and in the same proportion over the Crevasse Splay 2.

Likewise, the results of the experiment using both functions were checked graphically by plotting the raw data and the predicted curves. The match of each function was compared with the raw data (Fig. 31) to corroborate the results of the squared residual error comparison. As shown in the table 5, the Weibull function yields better fits to the raw data.

Crevasse splay 1			Crevasse splay 2		
Point	*RSS Using Gaussian Function*	*RSS Using Weibull Function*	*Point*	*RSS Using Gaussian Function*	*RSS Using Weibull Function*
C1_0	0,00518	0,00089	C2-1	0,00568	0,00540
C1_1	0,00481	0,00726	C2-2	0,00416	0,00736
C1_2	0,00727	0,00150	C2-3	0,00512	0,00332
C1_3	0,00478	0,00814	C2-4	0,00498	0,00226
C1_4	0,01021	0,00066	C2-5	0,00379	0,00604
C1_5	0,00276	0,00905	C2-6	0,00473	0,00336
C1_6	0,00504	0,00056	C2-7	0,00517	0,00603
C1_7	0,00480	0,00115	C2-8	0,00510	0,00275
C1_8	0,01538	0,00527	C2-9	0,00485	0,00043
C1_9	0,00519	0,00020	C2-10	0,00689	0,00250
C1_10	0,00457	0,00046	C2-11	0,00498	0,00167
C1_11	0,00585	0,00057	C2-12	0,00438	0,00082
C1_12	0,00436	0,00078	C2-13	0,00312	0,00214
C1_13	0,00508	0,00181	C2-14	0,00236	0,01145
C1_14	0,00457	0,00501	C2-15	0,00596	0,00045
C1_15	0,00717	0,00150	C2-16	0,00468	0,00519
C1_16	0,00372	0,00809	C2-17	0,00525	0,00107
C1_17	0,00486	0,00331	C2-18	0,00566	0,00447
C1_18	0,00746	0,00257	C2-19	0,00536	0,00543
C1_19	0,00570	0,00052	C2-20	0,01060	0,00149
C1_20	0,00441	0,00651	C2-21	0,00330	0,00769
C1_21	0,00527	0,00029	C2-22	0,00299	0,00012
C1_22	0,00459	0,00026	C2-23	0,00575	0,00284
C1_23	0,00457	0,00031	C2-24	0,00493	0,00113
C1_25	0,00403	0,00040	C2-25	0,00460	0,00033
C1_26	0,00448	0,00024	C2-26	0,00407	0,00023
C1_27	0,00472	0,00016	C2-27	0,00345	0,00028
C1_28	0,00496	0,00059	C2-30	0,00265	0,01174

Table 5. Squared sum of residual error (RSS) of Gaussian and Weibull predictions. Crevasse Splays 1 and 2.

In the second fitting experiment that was carried out over few selected samples, we compared the sum of squared error of the 2-component and 3-component predictions using Weibull function. This comparison showed that the 2- component curves fitted better than using three components. For these reasons, the best model to analyze the raw data might be the Weibull function model with two components.

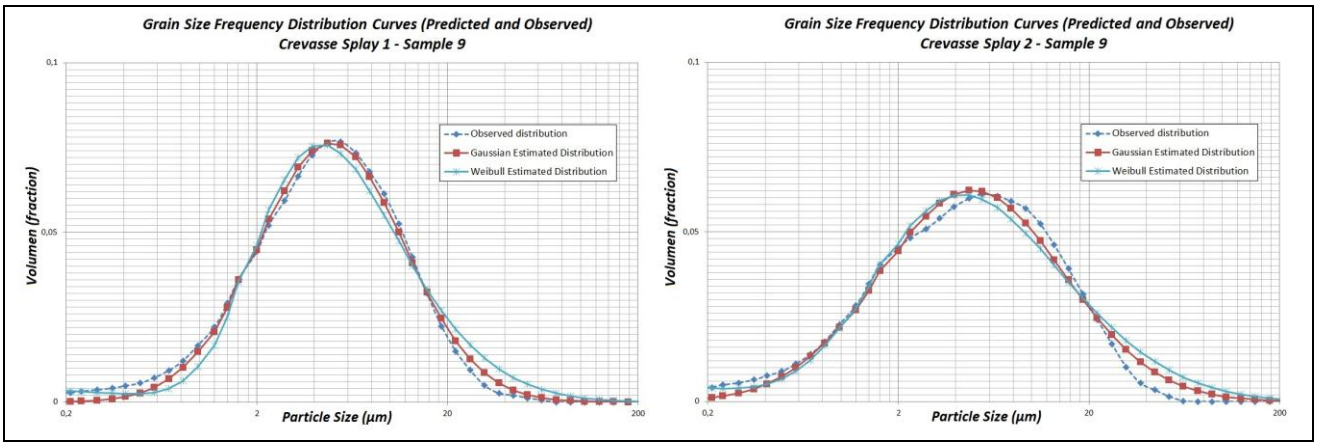

Figure 31. Fitting experiments using Gaussian function and Weibull Function Crevasse splay 1 sample 9 and Crevasse splay 2 sample 9.

The samples that did not have a good match (Fig 32) with the raw data were linked to samples with moderate influence of a third component. Therefore, on such samples a 3-component fitting experiment was run. The results of this experiment were poorer compared with the results of 2-component fitting experiment. In order to understand why a 3-component fitting experiment did not have better results than the 2-componet model, some samples were used to make thin sections to understand the genesis of the components. With these thin sections, the components present in the area were visualized. This information in turns was used to understand the sporadic presence of the third component in the laser results.

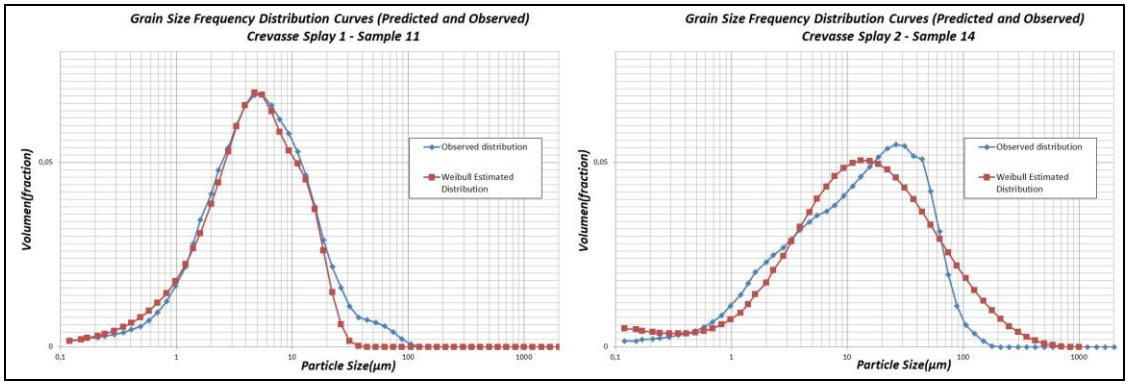

Figure 32. Fitting experiments with two components using Weibull Function Crevasse Splay 1_Sample 11 and Crevasse Splay 2 sample 14.

4.1.2.2.2. Partitioning and Components Description

Based on the previous arguments, each component will be described by its statistical moments based on the Weibull function. To visualize the trends present in the samples, a cumulative plot was created for each sample showing their respective Weibull components (Fig 33 - Appendix 6). With these plots, the Crevasse Splay 1 shows two main components, a first component that has a P50, which goes from 2.8µm to 3.8µm, and a second component that exhibits a P50 between 7µm and 25µm. In other words, the bulk grain size distribution can be divided by a clay component with grain sizes below 4µm and a silty component that exhibits values above 7µm. The cumulative curves of Crevasse Splay 2 were plotted showing the same behavior.

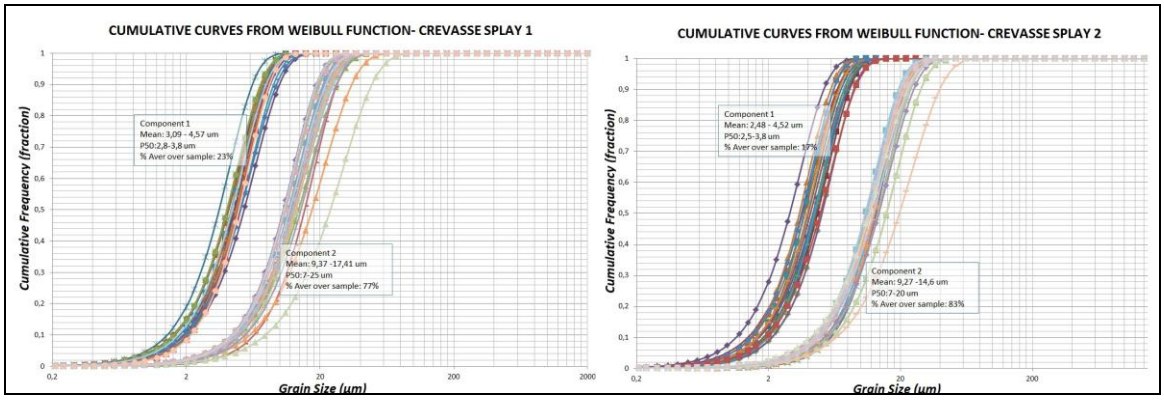

Figure 33. Cumulative Curves of the Identified components Crevasse Splay 1 and Crevasse Splay 2.

The proportion of the clay size component is around 30% and for the silt size component is 70% (Table 6). The high proportion of the silty component suggests that in order to have a good model for the grain size distribution, such component must be fully described on each sample. Therefore, the mean and the standard deviation of each sample were calculated (Table 6) using the shape and the scale parameters of the silty component. This process was carried out based on the Weibull cumulative curves by using the following equations (Blott & Pye, 2001):

$$M = \frac{(\emptyset_{16} + \emptyset_{16} + \emptyset_{16})}{3}$$

$$\sigma = \frac{(\emptyset_{84} + \emptyset_{16})}{4} + \frac{(\emptyset_{95} + \emptyset_{5})}{6.6}$$

Where, M is the mean grain size (phi units), ø is the diameter of the grain (phi units) at certain cumulative percentage and σ is the standard deviation (phi units).

Silty Component

The silty component of the Crevasse Splay 1 has a mean size that varies from 11.2 to 26.5 µm and a standard deviation between 0.804 and 1.26ø. Based on the mean size map, the silty component expresses a finger shape trend distribution (Fig. 34 – Appendix 5) that can be related to the crevasse splay depositional processes.

Table 6. Summary of mean size and standard deviation values from weibull function using two componets. Crevasse Splays 1 and 2.

Sample	Proportion Component 1 (Clay-Fracc)	Proportion Component 2 (Silt-Fracc)	Mean Size Component 2 (Silt-um)	Standard Deviation Component 2 (PHI)	Sample	Proportion Component 1 (Clay-Fracc)	Proportion Component 2 (Silt-Fracc)	Mean Size Component 2 (Silt-um)	Standard Deviation Component 2 (PHI)
C1	0,212	0,788	15,058	0,947	C2-1	0,128	0,872	16,693	0,864
C1-1	0,112	0,888	16,818	0,952	C2-2	0,137	0,863	17,770	0,900
C1-2	0,189	0,811	13,766	0,892	C2-3	0,180	0,820	13,529	0,590
C1-3	0,215	0,785	21,990	0,896	C2-4	0,155	0,845	13,019	0,774
C1-4	0,279	0,721	13,737	0,892	C2-5	0,136	0,864	16,393	0,852
C1-5	0,120	0,880	17,147	0,817	C2-6	0,141	0,859	13,273	0,769
C1-6	0,165	0,835	13,713	0,947	C2-7	0,142	0,858	16,720	0,892
C1-7	0,089	0,911	12,832	0,920	C2-8	0,145	0,855	14,124	0,797
C1-8	0,129	0,871	16,114	0,817	C2-9	0,133	0,867	12,435	0,900
C1-9	0,251	0,749	11,525	0,832	C2-10	0,192	0,808	14,234	0,824
C1-10	0,190	0,810	11,212	0,824	C2-11	0,140	0,860	14,642	0,895
C1-11	0,195	0,805	12,357	0,844	C2-12	0,152	0,848	11,593	0,809
C1-12	0,419	0,581	19,130	0,995	C2-13	0,072	0,928	12,442	0,789
C1-13	0,148	0,852	12,908	0,817	C2-14	0,146	0,854	21,064	0,852
C1-14	0,122	0,878	14,715	0,818	C2-15	0,143	0,857	11,777	0,832
C1-15	0,193	0,807	13,819	0,872	C2-16	0,090	0,910	15,683	0,900
C1-16	0,146	0,854	19,307	1,267	C2-17	0,102	0,898	12,529	0,886
C1-17	0,103	0,897	13,974	0,829	C2-18	0,149	0,851	16,711	0,852
C1-18	0,195	0,805	15,383	0,880	C2-19	0,128	0,872	18,000	0,774
C1-19	0,184	0,816	14,141	0,951	C2-20	0,146	0,854	13,301	0,852
C1-20	0,120	0,880	17,211	0,912	C2-21	0,114	0,886	19,929	0,824
C1-21	0,312	0,688	13,921	0,885	C2-22	0,300	0,700	11,451	0,824
C1-22	0,379	0,621	13,338	0,841	C2-23	0,339	0,661	21,706	1,015
C1-23	0,222	0,778	11,768	0,835	C2-24	0,168	0,832	12,077	0,789
C1-25	0,477	0,523	26,564	1,035	C2-25	0,176	0,824	12,416	0,892
C1-26	0,241	0,759	11,335	0,812	C2-26	0,176	0,824	12,747	0,947
C1-27	0,292	0,708	11,350	0,804	C2-27	0,328	0,672	13,409	0,900
C1-28	0,174	0,826	12,716	0,900	C2-30	0,274	0,726	26,395	0,789

This map shows high values at the junction with the Colorado River and in the central area of the crevasse splay, which can be associated to the location of the source points. Towards the edges of the crevasse splay, the grain size decreased gradually, which can be related to the energy of the environment acting on the sediments.

On the particle sorting, a cross-plot of the mean and the standard deviation (Fig. 35) was made showing a low correlation. This poor correlation shows that bigger particles seem to have better sorting than smaller particles (McCave, Manighetti, & Robinson, 1995). In theory, sorting can be associated with the energy of the environment and the strength of the medium. Therefore, once we move far from the source point such crevasse channels, the energy of the medium decrease, which could results in deposition of poor sorted sediments in those areas (Fig. 34).

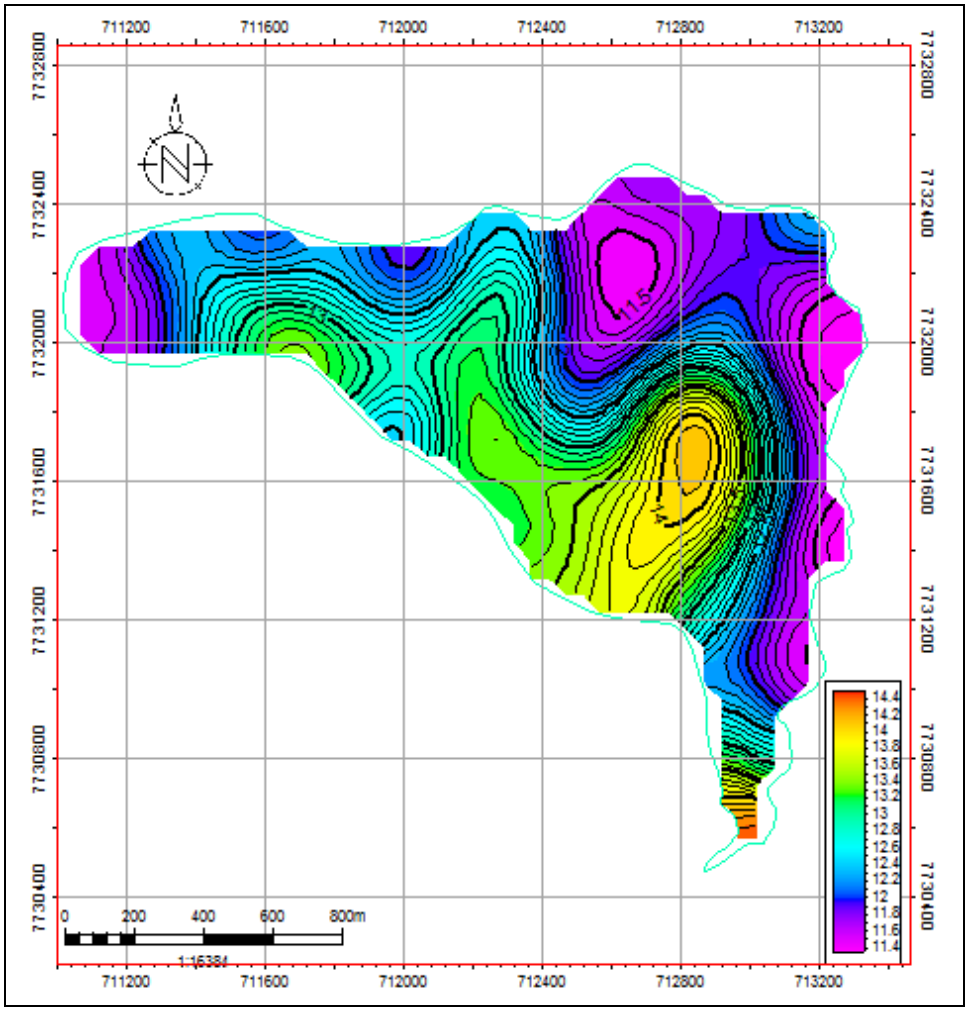

Figure 34. Silty Component Mean size Map (Weibull function 2-components) – Crevasse Splay 1

On the Crevasse Splay 2, the silty component shows a mean size distribution that fluctuates from 11.4 to 21.7 µm and a standard deviation that varies from 0.590 to 1.01ø. The mean size map (Fig 36– Appendix 5) let us see a radial pattern that is moving along an imaginary crevasse splay central axis.

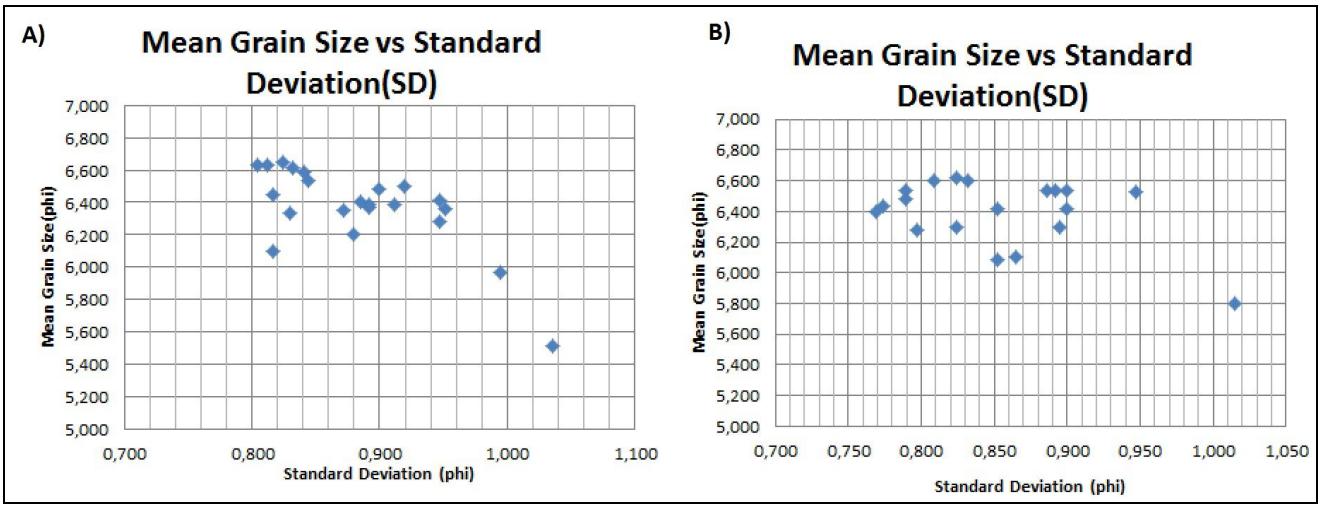

Figure 35. Mean Size and Standard Deviation from the silty component – A) Crevasse Splay 1; B) Crevasse Splay 2.

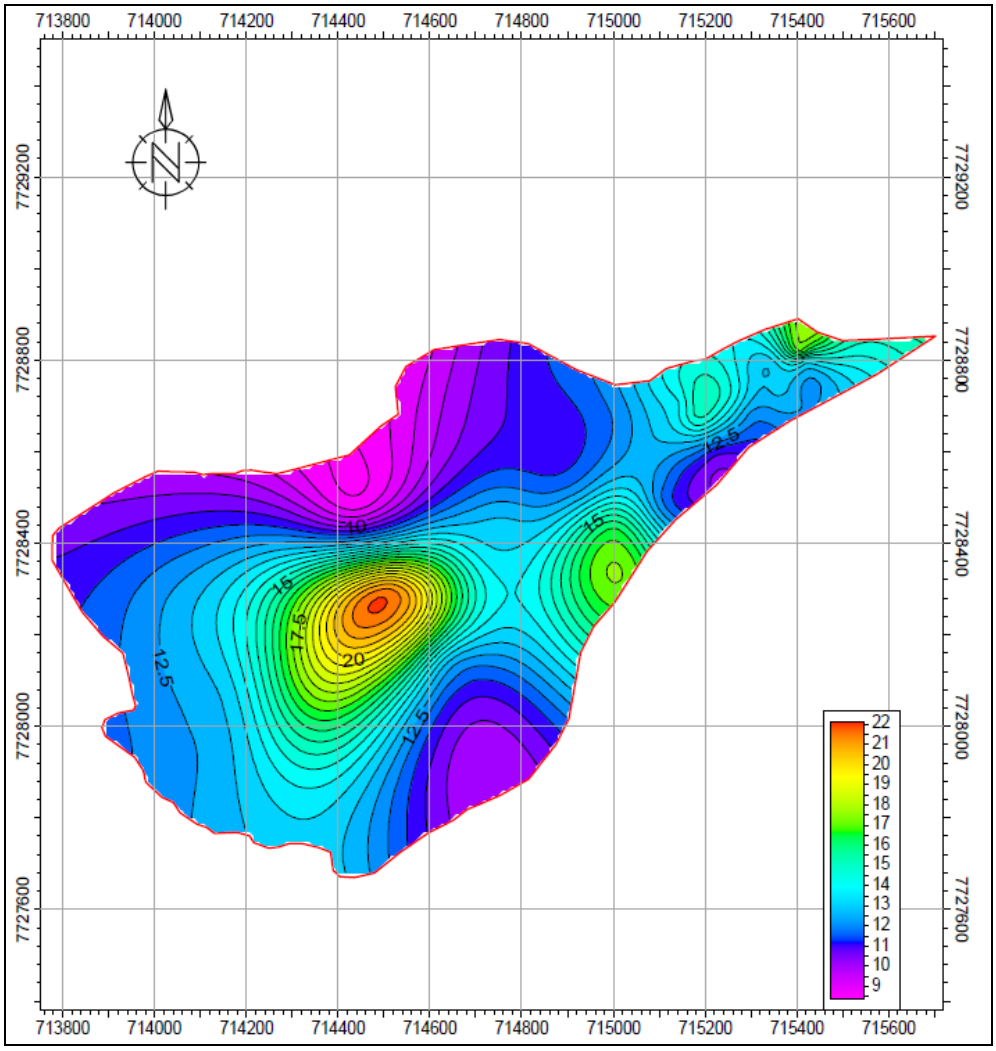

Figure 36. Silty Component Mean size Map (Weibull function 2-components) – Crevasse Splay 2

Clay Component

To understand how the clay component was deposited and its relationship with the main component (silt sediments), the clay volume was mapped. The map over Crevasse Splay 1 (Fig. 37 – Appendix 7) shows that the percentage of clay increases towards the margins of the sediment body, opposite to the source point. The increase of clays volume can be linked to the distance from the source points and to a later depositional stage than the silty component. This can be understood by the low correlation of the grain size and the standard deviation. In theory, if the clays were deposited together with the silts, then the higher clay volume would be found dispersed in areas, where the sorting would be poor, filling most of the empty spaces. However, the large volumes of clay are mostly present on the areas opposite to the source point, which can be related to a later depositional stage.

Additionally, by plotting the clay volume and the standard deviation of the silty component, (Fig. 38) it is not feasible to recognize any relationship. This suggests that the clay was deposited under different conditions than the silt. Such condition can be attributed to the waning processes and the effect of the deceleration on the flow (Banerjee, 1977), which implies that in areas of low energy levels, the clays could flocculate and form a blanket on top of the silt deposits.

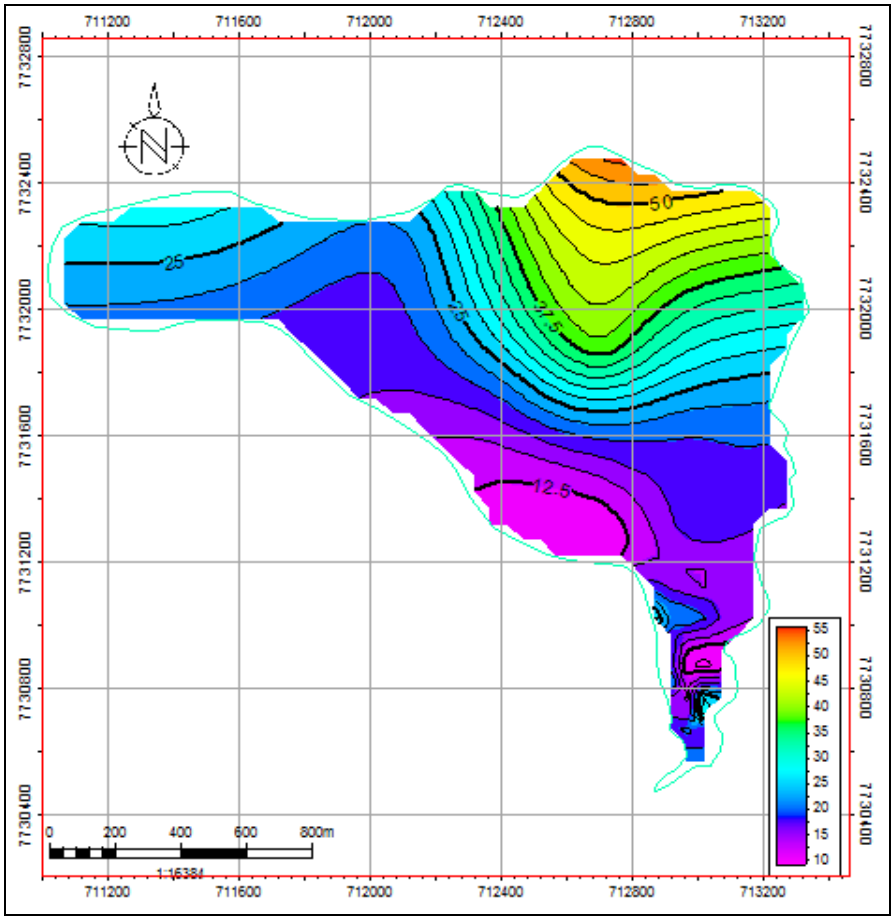

Figure 37. Clay Component Map (%) – Crevasse Splay 1.

The clay volume map over the Crevasse Splay 2 (Fig. 39 - Appendix 7) shows that the large volume of clay is deposited at the end of the crevasse channels. At these points the flow is unconfined, letting the fine particles be deposited following the same principles mentioned on the formation of Crevasse Splay 1.

Largest Component

This component has a grain size that exceeds 30 µm, reaching values up to 200 µm. Due to the small number of samples that contains this component and the low fitting degree of the 3-component model (using the Weibull function), this component was not including in the depositional analysis of the crevasse splays. Therefore, it is important to understand why this component is randomly present over the crevasse splays in order to have a better picture of the crevasse splay behavior. The first step in understanding the presence of this component in only a few samples is to characterize it in thin sections. The results of the characterization will be compared with the volume of silt and clay found by the fitting experiments to understand the genesis of the largest component present in the area.

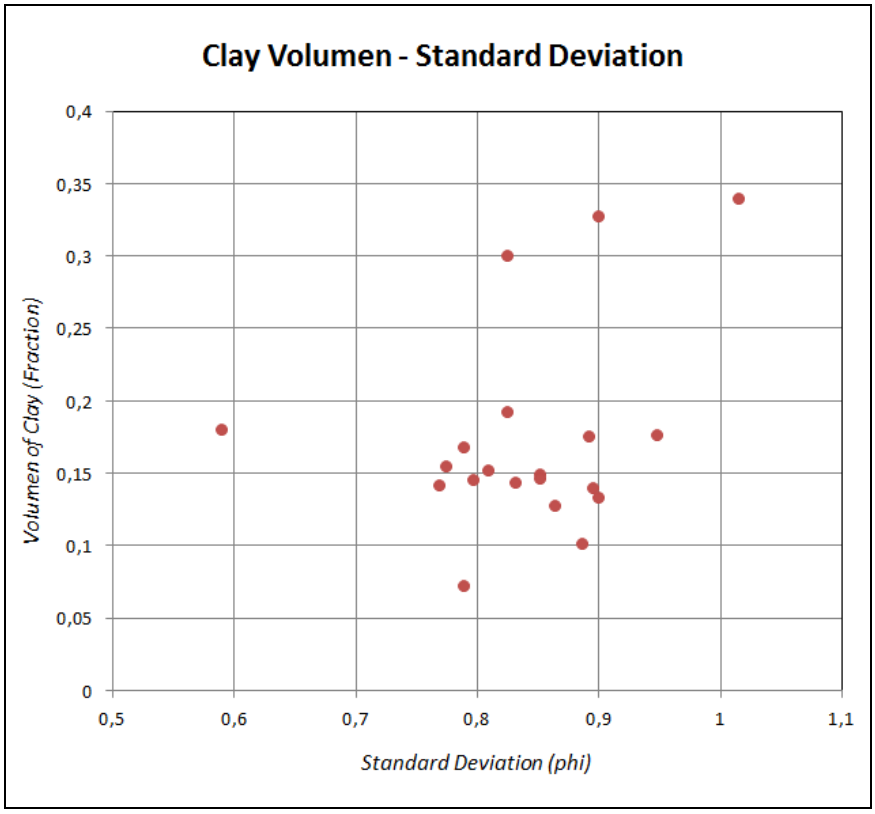

Figure 38. Clay Component (%) vs. Standard Deviation (silty component)

To make such characterization, few samples of loose sediments from the Crevasse Splay 2 were used to prepare thin sections. The chosen samples (C2-5, C2-14, C2-19 and C2-21) correspond to ones that did not show a good fitting with the Weibull function using 2 and 3 components. The particular preparation of the thin section consisted by submerging the samples in small vessels filled

with epoxy (glue product). Right after the loose grains were glued to each other, a thin slice was cut to create a thin section for microscope purposes.

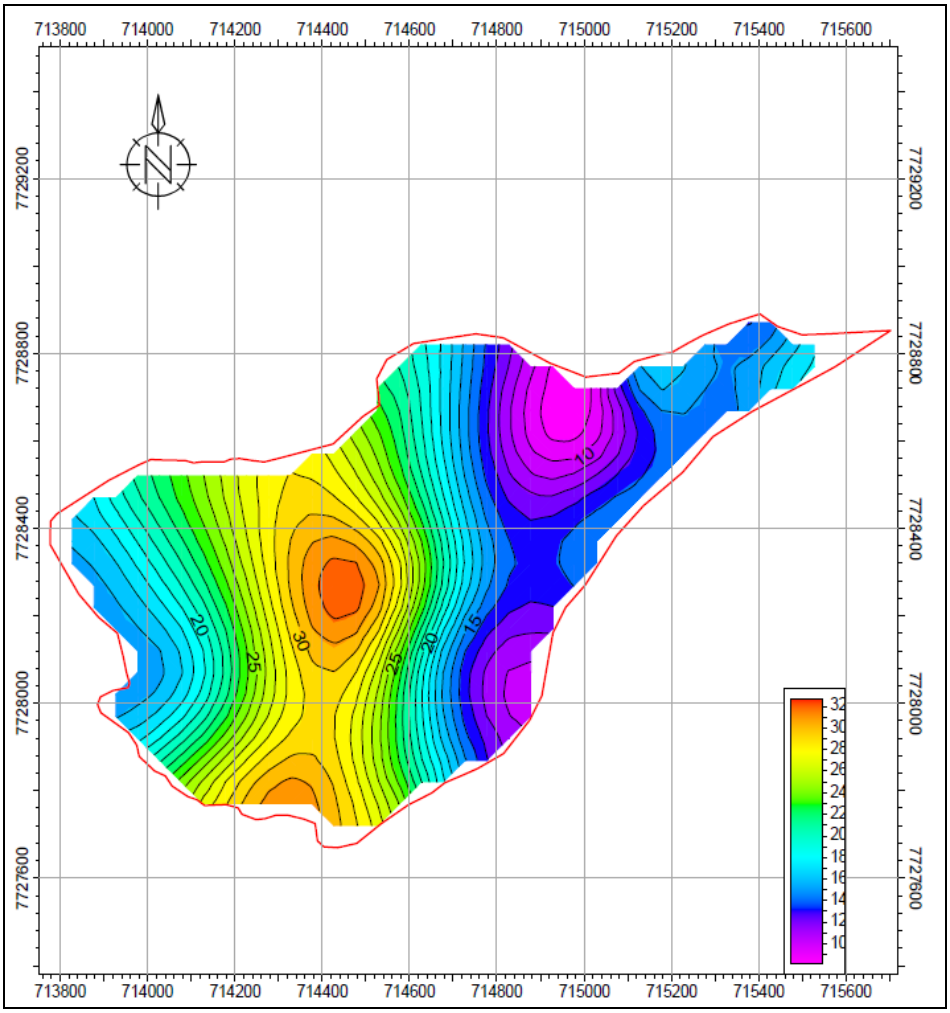

Figure 39. Clay Component Map (%) – Crevasse Splay 2.

In overall terms, the thin sections showed three main mineral components, which in turns can be classified by size. The largest proportion of crystals, which is about 65 to 75% of the samples are quartz that exhibits sizes between 10 and 20 µm. These crystals are generally sub angular to round (Fig. 40). The second component corresponds to clay minerals (25 to 30%). These crystals are brown and due to their dimension (<10µm), it is only possible to characterize them as clasts and/or aggregates, as it is shown in the figure 40.

The third component is represented by large tabular crystals of micas (>20um) and gypsum (Fig. 40). These crystals appear sporadically and correspond to the lowest percentage (1 - 5 %) of the samples. The micas are mainly tabular, thin, brown biotite crystals (Fig. 41) with strong colors of birefringence. The gypsum crystals are also tabular but colorless (XN), which helps us to difference them from quartz crystals.

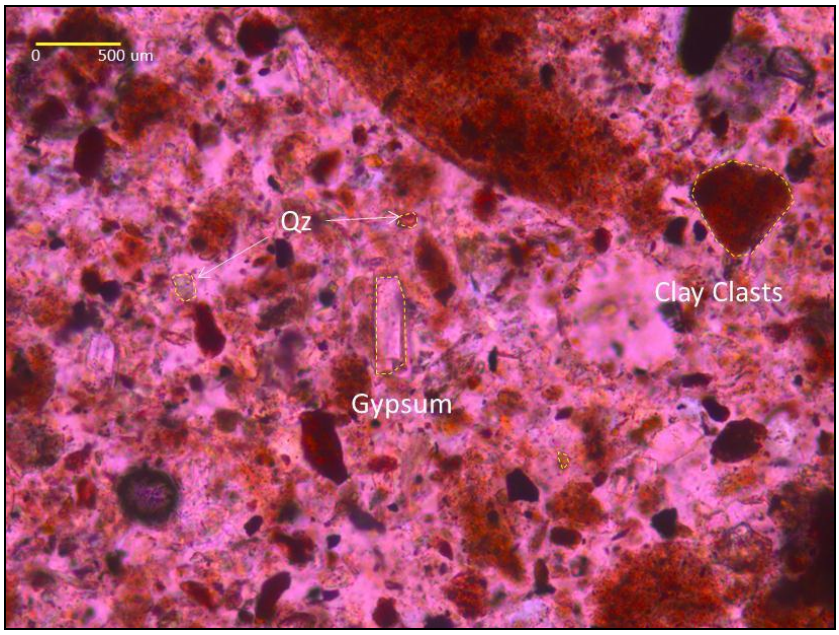

Figure 40. Thin section Sample 14 Crevasse Splay 2.

Due to the mineral composition of this component, we can see that the laser analysis method may not see this component in most of the samples because of the nature of the acquisition. In other words, micas are phyllosilicates, which make those crystals recognizable by the laser particle sizer in one dimension but almost imperceptible in the other direction. Therefore, in some samples this component has been detected, while in others is not or is included as part of the clay size component.

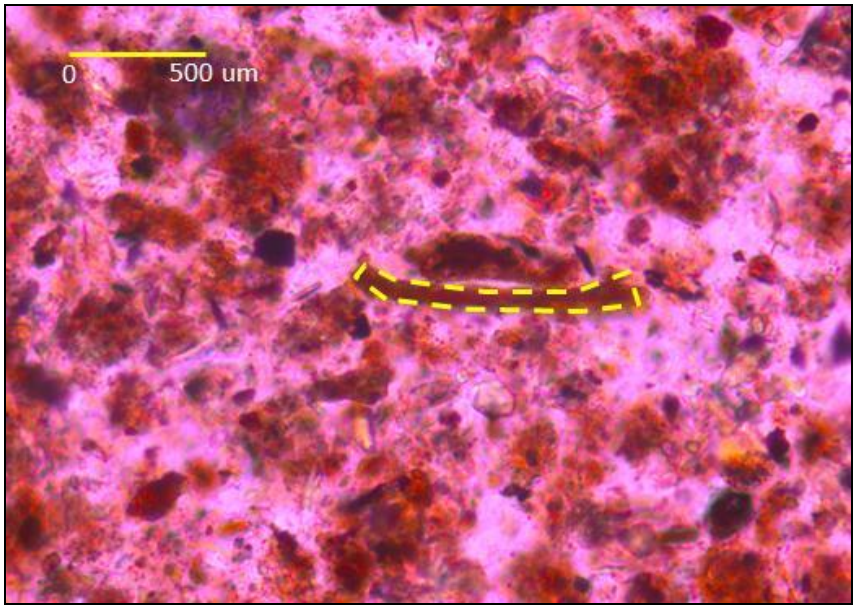

Figure 41. Thin section Sample 5 Crevasse Splay 2_ Mica crystal.

4.2. Grain Size Model

After describing the main components of the grain size distribution over the crevasse splays and understanding their most likely genesis, it is necessary to create a 3D grain size distribution (GSD) model. This model should faithfully represents the natures of such sediment bodies to proceed with a petrophysical modeling. Therefore, in this section we will describe how a 3D GSD-model was built and what kind of models and data were used in order to accomplish this objective.

4.2.1. Grain Size Model Definition

The mean grain size maps (silt component) of the crevasse splays show that the grain size distribution reflects the nature of the formation of such bodies. Therefore, based on that distribution, a 3D GSD-model will be create honoring the crevasse splay current stage. In order to do this, it is necessary to extract as much data as possible from the current satellite images, which show the recent physical distribution of surface properties of the crevasse splays. From such images, information such as RGBD data, scores of the Eigen Vectors (RBGD data processed) and crevasse channels were extracted. Based on this information, three different models were built from which we will choose one final model to guide the petrophysical property model.

The first two models deal with correlations of grain size data and satellite images. The grain size data used is the mean size values of the silty component. The second data source is the satellite images, which were obtained with Google Earth Pro software. These images have a horizontal resolution of 0.6 m/px over the study area.

In addition, all three models are strongly related to the distance with respect to the channels. This relationship can be explain by the dependency of the grain size to the energy of the environment, which in turns is related to the distance from the source point. Therefore, geo-referenced polygons of the channels and the edges of the crevasse splay were mapped through fake color images (Fig. 42). These fake images were obtained by manipulating the color spectrum of the satellite images.

a. 3D GSD-Model based on RGBD raw data.

This model was based on the assumption that the color changes over the satellite images can be associated to the grain size distribution along the crevasse splays. A relationship between the mean grain size and an attribute linked to its pixel at the sample locations could explain to which extent those variables are related to each other. Following this idea, RGBD data were extracted at the sample locations and to avoid noisy data, an average of RGBD data was taken around the sample location.

Once the average of the RGBD data was extracted, these 4-dimensional vectors or compositional RGBD data were transformed into log ratios giving the natural means of studying such data (Pawlowsky-Glahn & Egozcue, 2006). The log ratio transform recognizes that the relative magnitudes and their variations describe better the compositional data than their absolute values. Therefore, in order to have a better understanding of this compositional RGBD data, two of the

most well-known log-ratio representations such the additive-log-ratio (ALR) and the centered-log-ratio (CLR) were applied to the RGBD data transforming this data to real vectors.

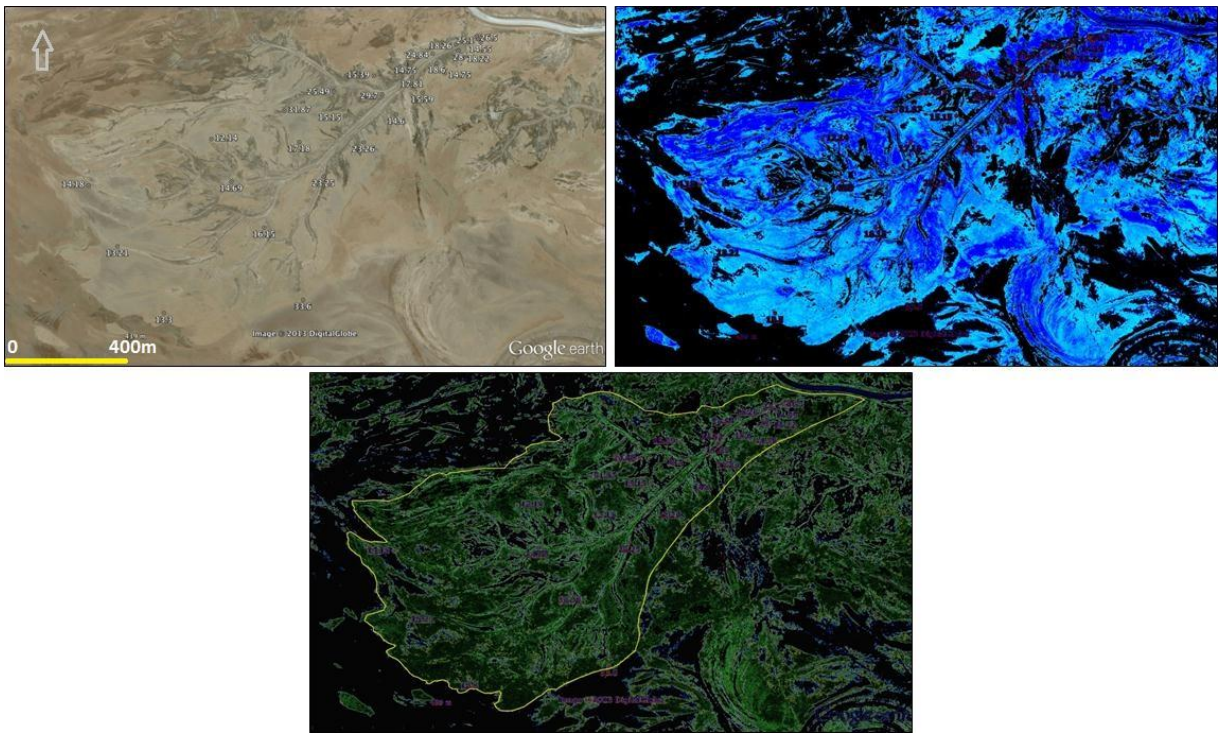

Figure 42. Edges and Channels Splay Detection Using Fake Color Images. (Crevasse Splay 2 - See Fig 8b)

The first log transformation applied to the RGBD data was the additive log ratio transformation (ALR), which essentially is the log normal of the ratios. This log transformation is described as:

$$alr(x) = [\ln\left(\frac{x_1}{x_D}\right); \ldots; \ln\left(\frac{x_{D-1}}{x_D}\right)]$$

A multivariate regression analysis (Duleba & Olive, 1996) was performed on the ALR of the RGBD data and mean grain size. This technique consisted of a regression analysis of several independent variables (ALR of RGBD data) and the mean grain size data at the acquisition points. The best result of such regression gave a very low correlation coefficient (R^2=0.052), which can be understood by plotting the original grain size data against the predicted grain size data (Fig. 43). This plot shows that the predicted values from the function found do not honor the original data.

Therefore, a second multivariate regression between the ALR of the RGBD data and distance from the samples with respect to the closest channel was carried out. The purpose behind this regression consists of finding a relationship between the RGBD information and the distance from the possible source. Based on the distance predicted from ALR of the RGBD data, a second correlation between distance and mean grain size would be used to develop a grain size model. According to this statement, a multivariate regression of ALR of the RGBD data and distance from the source at the location points were executed. The results of this multivariate regression were similar to the former

regression giving a correlation coefficient of 0.09, which implies that the ALR cannot be used to predict grain size.

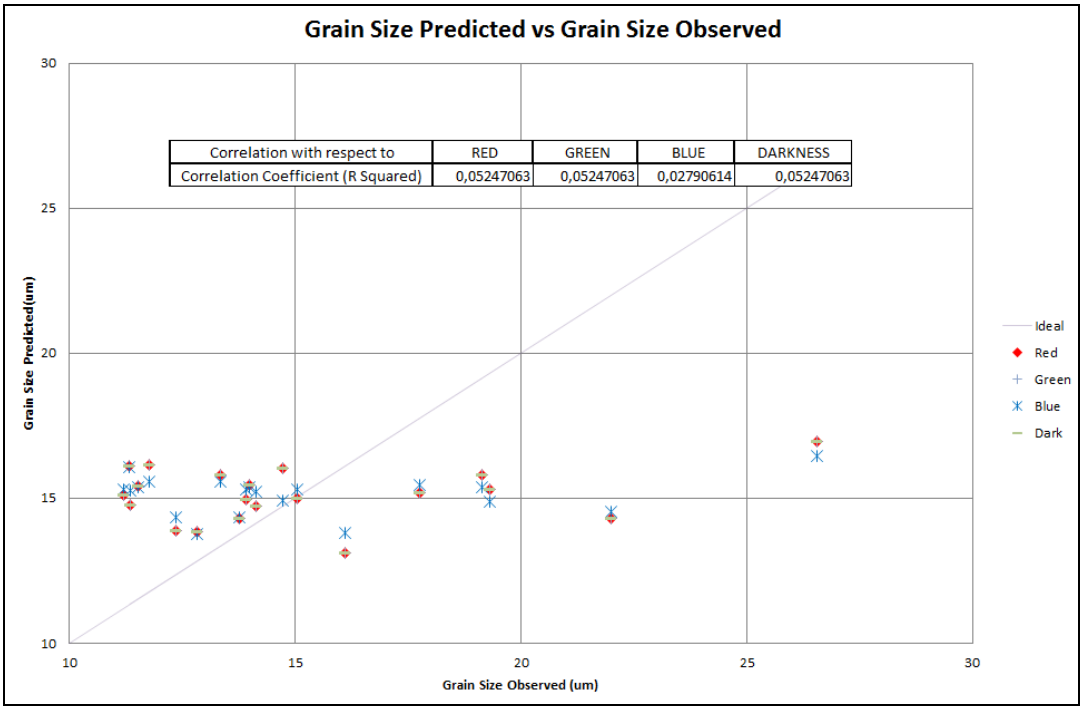

Figure 43. Grain size observed vs. Grain size predicted (Multivariate regression Grain Size and ALR of RGB data)

Due to the low correlation of the additive-log-ratio with the mean grain size and distance, a second log ratio representation was applied to the RGBD data. This transformation is called the centered-log-ratio transformation (CLR) and is expressed as follow:

$$clr(x) = [\ln\left(\frac{x_1}{geom(x_D)}\right); \ldots; \ln\left(\frac{x_{D-1}}{geom(x_D)}\right)]$$

Following the same steps, a multivariate regression of CLR data against mean grain size and distance was carried out giving correlation coefficients of 0.0524 and 0.0525 respectively. These values show that the relationship of RGBD data at the acquisition points with grain size and distance are remarkably weak. This low correlations could be associated to the random color noise, which can be the result of the salt content present in the area and to the small number of sample points that were taken into account. For these reasons, a second GSD model based on Eigen vectors of RGBD data was developed. As will be described in the next section, this model uses the whole satellite image in order to deal with the problem related to the scattered samples.

b. 3D GSD Model based on RGB processed data.

Another robust correlation between distance and RGBD data along the whole crevasse splays was established. This correlation is based on the RGBD data at every single pixel within the crevasse splays and the distance of those pixels with respect to the closest channel. In order to obtain the

data regarding to the distance of every single pixel to the channels, a geometrical grid property called *distance* was built in Petrel (Fig 44). This grid was created based on the digitalized polygons of the identified channels by changing the color attribute of the satellite images.

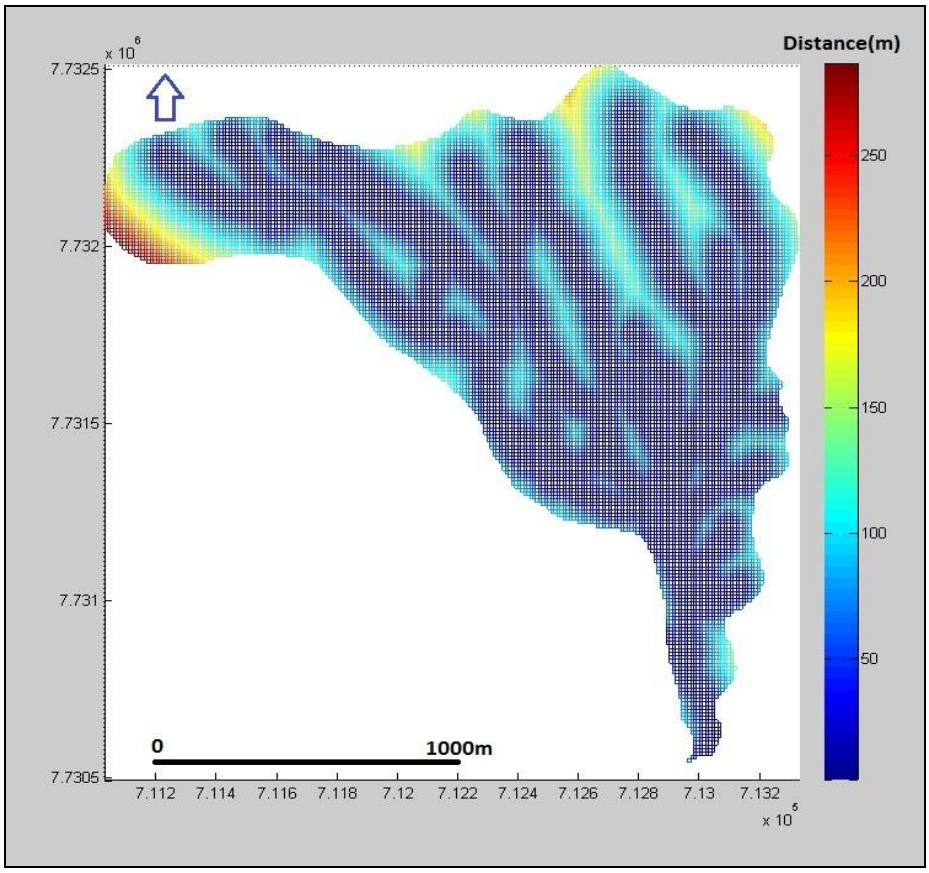

Figure 44. Distance with respect to channels. Crevasse Splay 1.

The second component of the correlation is the RGBD data but because of the low correlation of the transform data (ALR-CLR), it was found that in theory the Eigen vectors of the RGBD data could provide better information about that attribute (Rehna & Jeyakumar, 2012; Jia, 2012). The Eigen Vectors and its scores are in theory good descriptors of data with large volume of noise, which in the crevasse splays can be linked to the salt and super dry areas.

In order to obtain the scores of the Eigen vectors from the RGBD data, the singular value decomposition technique was applied to the RGBD data (Rehna & Jeyakumar, 2012; Jia, 2012). With this technique is possible to obtain as many scores as the components present in the data. A linear regression was carried to predict the distance to the channel from RGBD data. This regression consisted of correlating the first score of the RGBD data (Fig. 45) and the distance to the closest channel at every pixel within the crevasse splays (Fig. 44). The results of the linear regression between the first score and the distance were not conclusive. As shown in figure 46, at short distances to the channels the corresponding scores has a large variation, while at large distances this variability becomes narrower. In the same way, the second score of the Eigen vector and the

distance to the channels were correlated. The results of this correlation were again poor, showing that the Eigen vectors for this particular case does not describe properly the distance with respect to the channels.

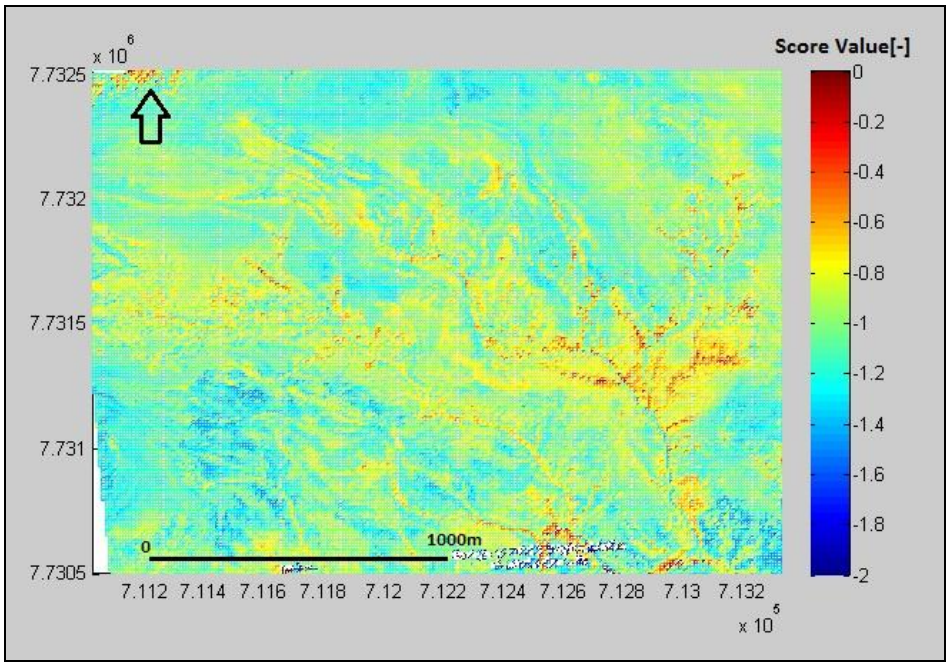

Figure 45. 1st score of the Eigen vector form the RGBD data Crevasse Splay 1.

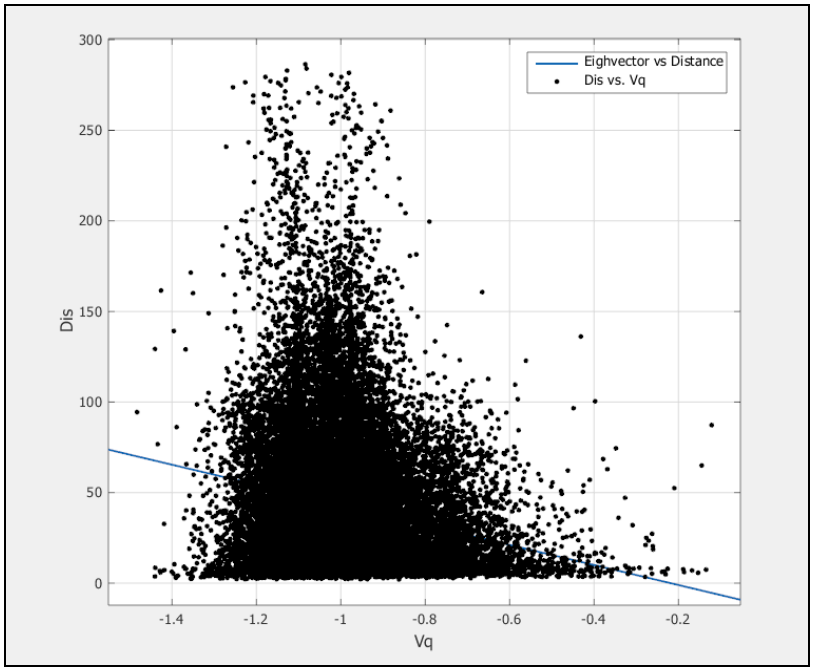

Figure 46. Distance to the Channels vs. 1st score of the Eigen vector. Crevasse Splay 1.(Dis=Distance[m];Vq= Eigen vector score[-])

Additionally, the scores of the first and second Eigen vector were plotted in order to recognize anomalous data that could be filtered to obtain a better match with the distance. However, after plotting this information (Fig. 47), we can see that there is not anomalous data that can be filtered or linked with abnormal process during the deposition of the crevasse splay.

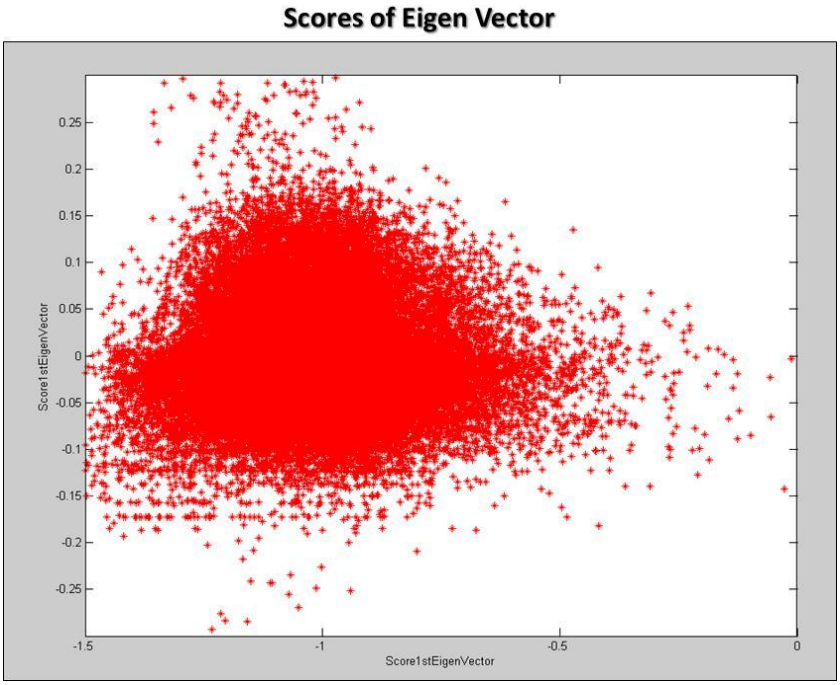

Figure 47. First score vs. Second score of the Eigen vector from the RGBD data Crevasse Splay 1.

c. 3D GSD Model based on channels splays.

A new model associated to physical characteristics like channels was built, due to the low correlations of the previous models. This model was based on the idea that the colors of the satellite images are not good predictors but the channels, which are identifiable by visual checking, can be the clue to the grain size distribution along crevasse splays. In order to develop this model, every single channel present in the crevasse splays and the edge of such sediment bodies were digitalized. Using the data about distance to such features from the sample location and the measurement of the grain size at those locations, several models were built. The results of these models depend on the locations of the channels, which act as local sediment sources. Therefore, several models with different number of channels acting as a source point were analyzed to find the best case to be considered in the grain size modeling.

The first analyzed case was based on the assumption that all sediments that constituted the crevasse splays were expulsed from a specific source point, which in this case would be the breaking point of the river levee. According to this, a radial distance grid was created following the boundaries of the Crevasse Splay 1(Fig. 48). With this information, the distance from the sample points to the source point was extracted and plotted against the mean size. The result of a linear correlation plot (Fig. 49) gave a correlation factor of -0.413. This coefficient in comparison with the

previous models is considerable better but it cannot be considered as a good predictor for grain size distribution yet.

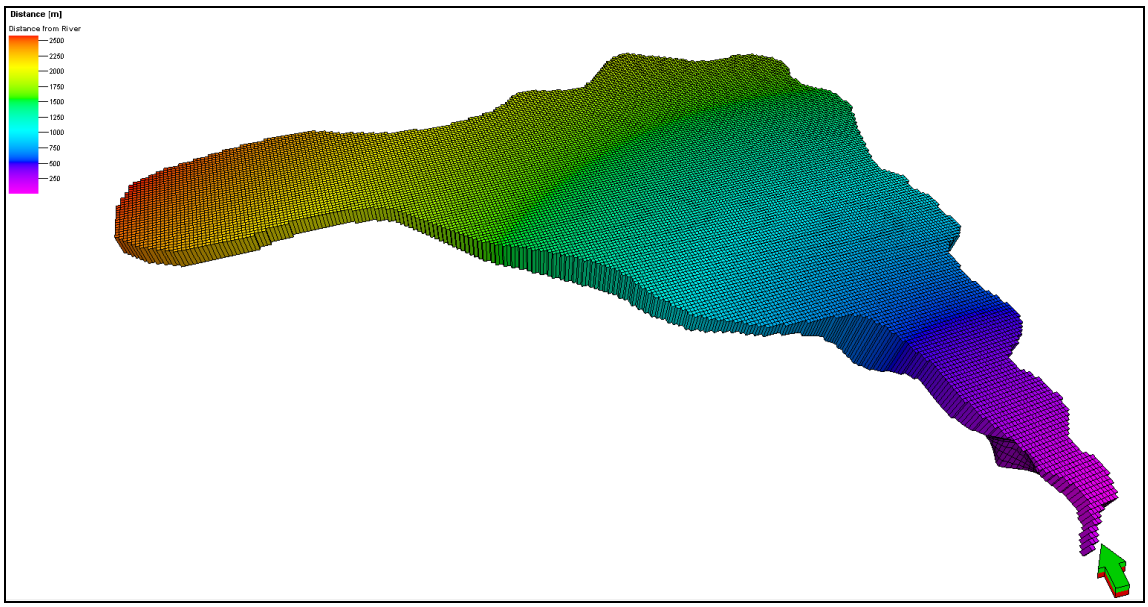

Figure 48. Distance from the breaking levee point (Colorado River). Crevasse Splay_1.

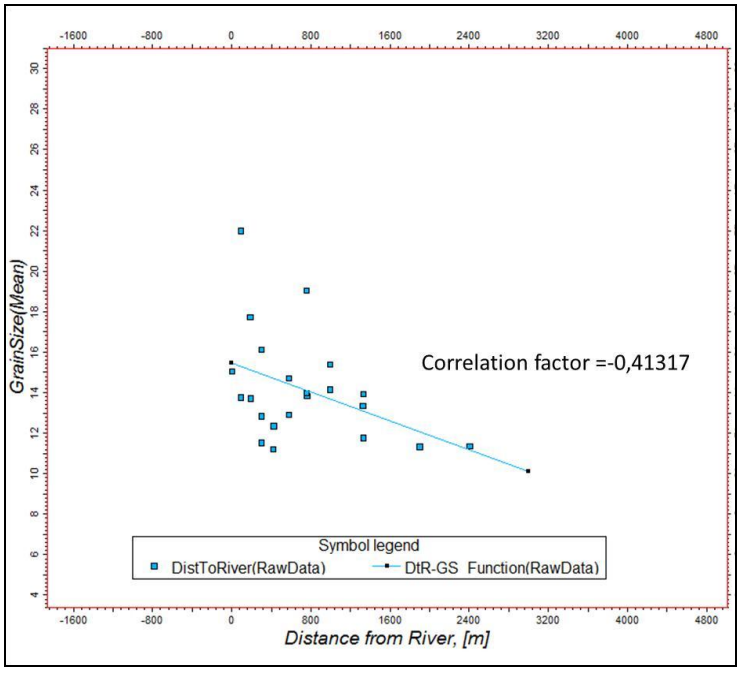

Figure 49. Linear Correlation between Distance from the breaking levee point and Mean Grain size. Crevasse Splay 1.

The second analyzed case considered the central channel of the crevasse splay as a unique source area (Fig 50). After generating the distance grid, the respective property was extracted at the sample locations and plotted against its respective mean size. The results of a log base correlation gave us a correlation factor of -0.406, which is relatively similar to the previous one. From this

correlation, it is important to remark that some data points are out of range from the predicted curve (Fig 51).

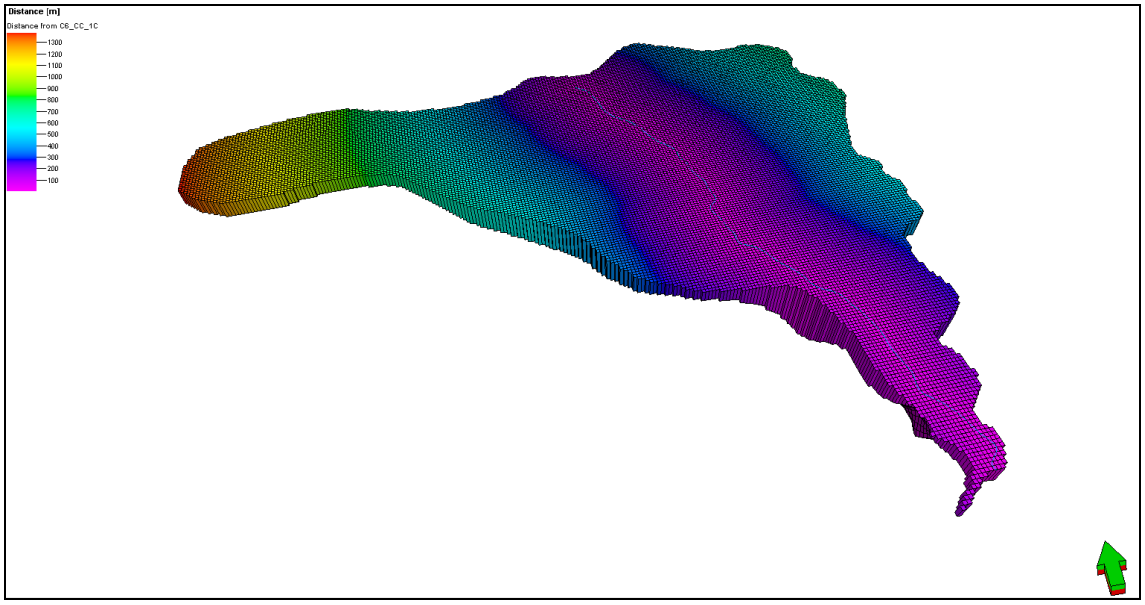

Figure 50. Distance Grid from a Central Channel. Crevasse Splay_1.

Therefore, a data check was performed to identify the points that could be filtered to get a better match. After checking the data, some of the non-correlationable data points coincide with the lower residual squared sums (RSS) from the fitting experiment of the Weibull function. These data points exhibit a better RSS under the Gaussian fitting experiment, which makes those data points less trustable than the others. After that, those points were identified and excluded from the correlation, resulting in a better correlation coefficient of -0.487 (Fig. 51).

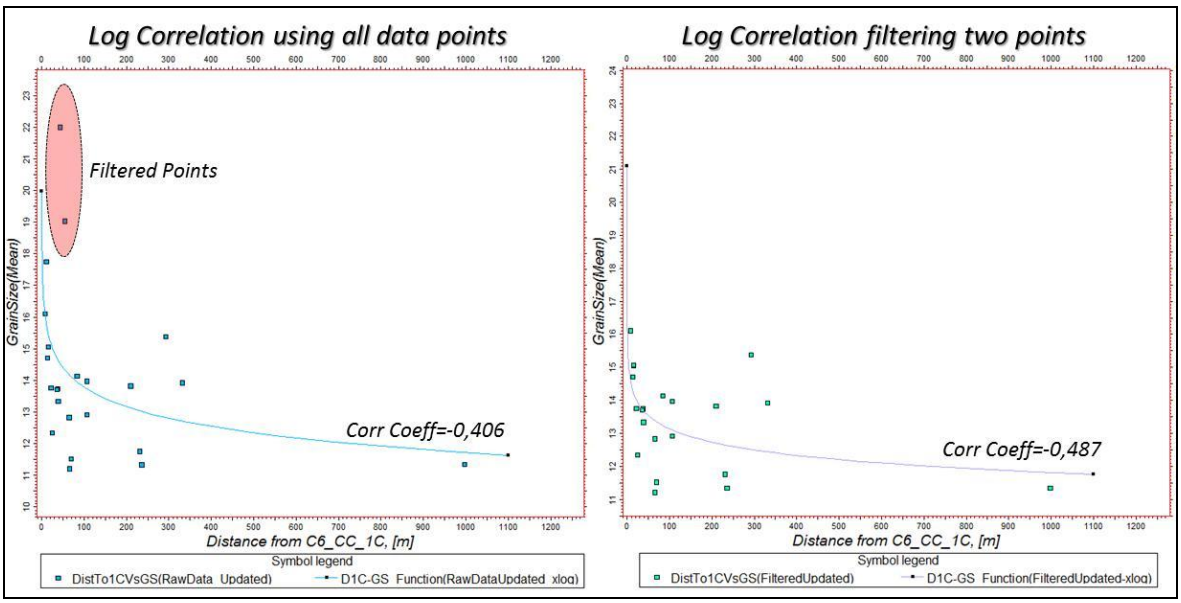

Figure 51. Log Correlation between Distance from the Central Channel and Mean Grain size. Crevasse Splay_1.

Afterwards, a third case was constructed (Fig. 52) based on the largest channels within the crevasse splays. As in previous cases, the distance from the channels was plotted against the mean sizes. A log base correlation using all data points gave a correlation coefficient of -0.393, while filtering some data under the conditions mentioned, the correlation factor increased to -0.626 (Fig. 53).

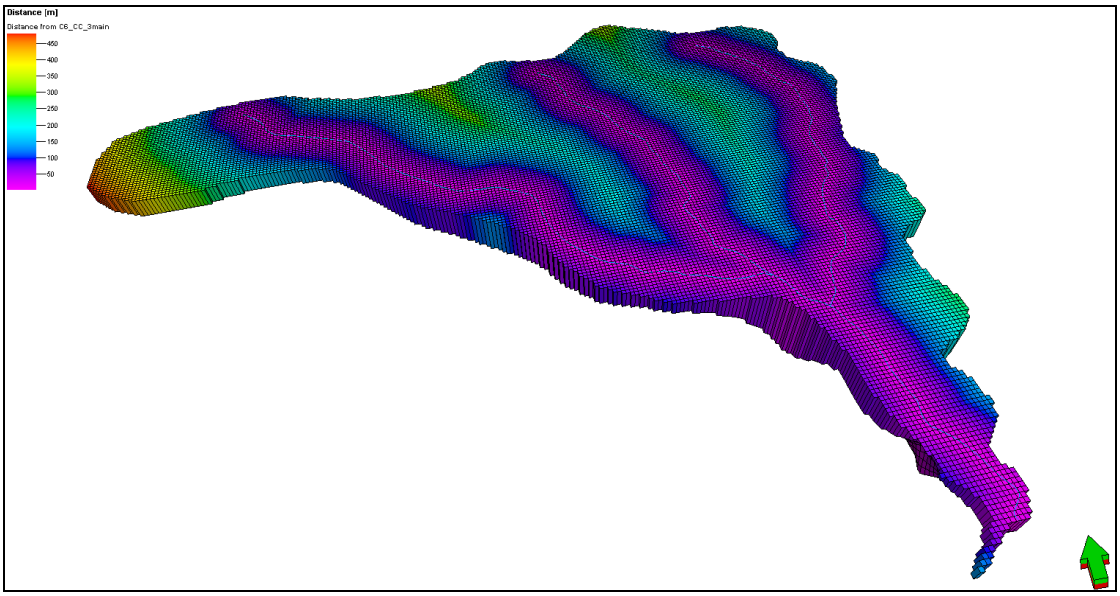

Figure 52. Distance Grid from main channels within crevasse splay_1.

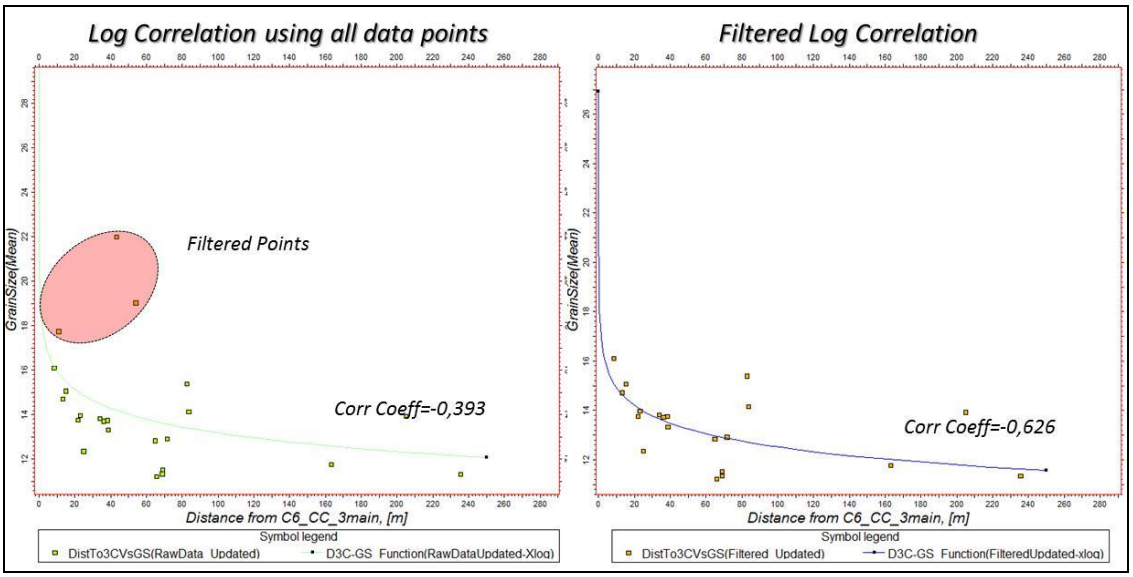

Figure 53. Log Correlation between Distance from main channels and Mean Grain size. Crevasse Splay_1.

The last analyzed case to build a 3D GSD model was constructed by using all the visible channels present into the satellite image (Fig 54). In this case, the log base correlations using all data points and the filtering the data gave correlations coefficients of -0.309 and -0.415 respectively.

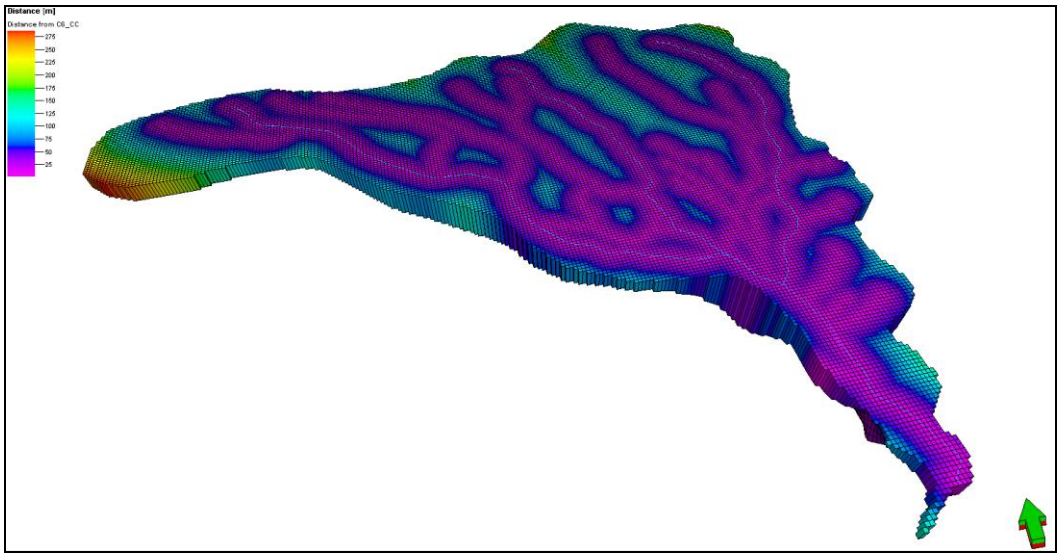

Figure 54. Distance Grid from all channels within crevasse splay_1.

4.2.2. Model results

Based on the correlations coefficients given by the models (Table 7), it was found that the grain size distribution has a good relationship with the main channels found in the satellites images. On the other hand, it has been shown that the grain size distribution does not have a good correlation with the color spectrum obtained from the satellite images. These satellites images did not show good results because they color spectrum can be affected by different process such as salt precipitation. Therefore, the physical channels that have not changed considerably during the last ten years are the best input to build up a good grain size model.

Table 7. Correlation Coefficients. Crevasse Splay 1.

Method		Correlation Coefficient
Grain Size - RGB data(ALR) Crevasse splay 1	With respect to Red	0,0525
	With respect to Blue	0,0279
	With respect to Green	0,0525
	With respect to Dakness	0,0525
Grain Size - RGB data(CLR) Crevasse splay 1		0,0525
Distance To Channels - RGB data(ALR) Crevasse splay 1	With respect to Red	0,0942
Distance To Channels - RGB data(CLR) Crevasse splay 1		0,0525
Grain Size -EigenVector Crevasse splay 1	1st Score	0,0040
	2nd score	0,0023
Distance To Breaking Point - Mean Grain Size on Crevasse Splay 1	All data	-0,3366
	Filtered data	-0,3605
Distance To Central Channel - Mean Grain Size on Crevasse Splay 1	All data	-0,4060
	Filtered data	-0,4875
Distance To Main Channels - Mean Grain Size on Crevasse Splay 1	All data	-0,3931
	Filtered data	-0,6261
Distance To All Channels - Mean Grain Size on Crevasse Splay 1	All data	-0,3096
	Filtered data	-0,4150

In addition, distance to the main channels will be used as the predictor for grain size distribution based on the theory that grain size is associated with the energy of the environment and the strength of the medium (Weltje & Prins, 2003).

According to this, the final 3D grain size models for Crevasse Splays 1 and 2 were built (Fig. 55 - Appendix 5) using the equations that describe the relationship between grain size and distance. These final models show that grain size has a logarithmic variation from 16 um to 11 um at the channels and at the edges of the crevasse splay respectively (Fig. 55).

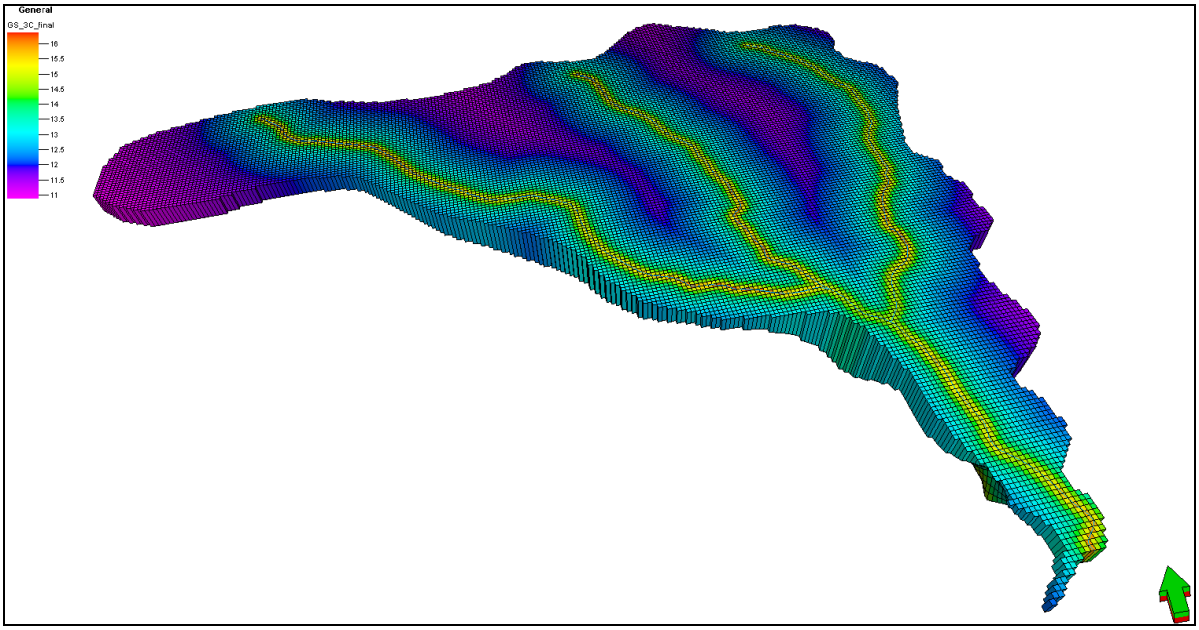

Figure 55. Final Grain Size Model based on distance to the main channels within Crevasse Splays 1 and 2.

5. Crevasse Splay Static Model

After building a 3D grain size distribution model, it is necessary to create a crevasse splay static model to rank and understand these sediment bodies as a hydrocarbon reservoir. In this chapter, we will discuss the property modeling, which is one of the main ingredients that form a static model. The property model will be divided into a porosity model and a permeability model, which will be described in terms of the grain size distribution due to their relationship with this property.

Another aim of the project is to define what can be the hydrocarbon storage capacity of crevasse splays in dry land river systems. This systems in turns are well know because of their characteristic low net to gross. However, crevasse splays are sediment bodies that cover large areas as was discussed in chapter 3, which makes them remarkable in terms of hydrocarbons storage. Based on the static model, we will describe the way to obtain gas resources and how to understand these resources in terms of tight gas reservoirs. Likewise, advantages and disadvantages of crevasse splay as gas reservoirs and its chances of being an important target for futures developments in the oil industry will be discussed in the next sections.

5.1. Property Modeling

The property model is subdivided into a porosity model and a permeability model. These models are based on the pillar grid, which was filled with the properties that describe each model. The porosity model will be derived from the grain size distribution, while the permeability model will be derived from the results of the porosity model.

5.1.1. Porosity Model

This model describes how porosity behaves in crevasse splays based on the grain size data. The input data for the *initial porosity distribution* is the mean grain size and the standard deviation (sorting) of the sediments that describe the crevasse splays. In other words, the silty component that was described in chapter 4, will be the main input for the initial porosity model.

The assumption that porosity can be derived from grain size and sorting is based on previous works (Fraser, 1935; Rogers, 1961; Beard & Weyl, 1973; Yu & Standish, 1991). The main idea of these works converges to that sediments with moderate to low sorting have a linear relationship between grain size and sorting with respect to porosity. So, if sorting decreases then porosity will decrease, and if the grain size decreases then porosity can increase (Rogers, 1961).

Likewise, porosity has been studied widely in terms of its relationship with the texture of the sediments. This shows that grain size and sorting are not exclusive to carry out porosity predictions in which sphericity and angularity could also plays an important role (Beard & Weyl, 1973). As a result, many authors have described why sphericity and angularity could affect porosity and to which extent these properties for instance can be related to the grain size. In spite of the influence of sphericity and angularity on porosity, in this study such property will be derived only from grain size and sorting due to the large impact of these parameters over porosity.

Initial porosity takes in account the texture of the sediments, which is just the first condition to create porosity in any sediment body. This porosity could be reduced by many factors such as burial history, diagenetic processes, secondary cementation, etc. (Beard & Weyl, 1973) resulting in the current porosity of several reservoirs over the world. In this study, the initial porosity will be described in detail, and after that such property will be transformed to subsurface conditions at different scenarios using empirical algorithms described in the literature.

a. Initial Porosity Model

In order to obtain initial porosity (porosity right after deposition), many authors such as Hembree, Colby, Swenson, & Davis (1952), Scherer (1987), Yu & Standish (1991), Yu et al. (2003) and Wu & Wamg (2006) have published equations for porosity predictions. For example, Scherer (1987) formulated an equation based on Beard & Weyl's theory (1973), who inferred that porosity is mainly affected by sorting. In Dullien (1979), packing involves random assemblies giving an equation in which porosity is just dependent on sorting. On the other hand, other authors such as Wu & Wamg (2006) express that porosity in uniform deposits is related to the grain size of the sediments, which in theory could affect the packing assemblies that at last impacts the initial porosity.

According to these theories, initial porosity is strongly related to the particles packing but due to the difficulty to characterize the packing structure most of the porosity predictions assume fixed assemblages. Therefore, geometrical and analytical models have been developed in which the packing of particles has been related to porosity. The geometrical model is based on statistical geometrical analysis that can be used to predict contact points of a packing of spheres, which in turns is the base of a mathematical model for porosity estimation (Yu & Standish, 1991). The second model that includes a packing of spheres is the analytical model. This model is the pillar of the mathematical model that will be used for the estimation of porosity for the crevasse splays under this study (Weltje & Alberts, 2011).

The analytical model that will be considered for initial porosity predictions is known as the linear-mixture model. This model depends on the size ratio (small/large) of several components that

defines the packing of the controlling mixture (Yu & Standish, 1991). Based on this, initial porosity can be derived as a function of the particle size. However, it is important to keep in mind that the mathematical model was based on spherical particles, which limits this model for non-spherical particles (Yu & Standish, 1993).

The initial porosity model developed by Yu & Standish (1991) is defined by gravitational forces, which is not the only force acting over the fine particles packing. Packing of fine particles involves other inter-particle forces such as van de Waals and electrostatic forces (Yu et al., 2003). For example, several experiments have demonstrated that van der Waals forces are more significant than gravity forces over particles below 100 µm. Based on these results, initial porosity, grain size and inter-particle forces were correlated by Yu et al (2003) developing the following equation for initial porosity.

$$\varepsilon = \varepsilon_0 + (1 - \varepsilon_0) * \exp(\alpha * d^{\beta})$$

where, ε is the initial porosity, ε_0 is the porosity without any inter-particle forces, *d* is the particle diameter (µm) and *α* and *β* are constants that depend on the inter-particle forces, which in turn are related to the particle diameter.

Based on this model, initial porosity was calculated using the grain size distribution of the silty component at the sample locations by Dr. Weltje at TU Delft. The values of porosity without any inter-particle forces (ε_0) and the coefficients *α* and *β* were estimated for average sediments at surface by Dr. Weltje giving a value of 0.4, -0.4 and 0.5 respectively. The results of the initial porosity prediction are shown in the table 8.

Table 8. Porosity results from the grain size distribution of the silty component.

Crevasse Splay 1		***Crevasse Splay 2***	
Sample	Porosity(fracc)	Sample	Porosity(fracc)
C1	0,536	C2-1	0,506
C1-2	0,534	C2-3	0,524
C1-4	0,536	C2-4	0,531
C1-6	0,549	C2-6	0,528
C1-7	0,551	C2-8	0,522
C1-8	0,505	C2-9	0,555
C1-9	0,553	C2-10	0,524
C1-10	0,555	C2-11	0,526
C1-11	0,547	C2-12	0,549
C1-12	0,512	C2-13	0,539
C1-13	0,535	C2-15	0,552
C1-15	0,533	C2-17	0,548
C1-17	0,526	C2-18	0,506
C1-18	0,520	C2-20	0,538
C1-19	0,546	C2-22	0,553
C1-21	0,537	C2-23	0,504
C1-22	0,539	C2-24	0,543
C1-23	0,552	C2-25	0,549
C1-25	0,484	C2-26	0,561
C1-26	0,554	C2-27	0,543
C1-27	0,552		
C1-28	0,549		

After initial porosity was derived at the sample locations, this property was plotted against the mean size of the silty component at those locations (Fig 56). The correlation between initial porosity and mean grain size gave a correlation coefficient of -0.896, which is acceptable for porosity prediction along the Crevasse Splay 1. Based on this correlation, initial porosity was populated along the crevasse splays resulting in initial porosities that vary from 52.4% to 55% in Crevasse Splay 1 (Fig. 57) and 49.9% to 55.37% in Crevasse Splay 2.

The initial porosity model (Fig. 57 – Appendix 8) represents porosities without taking in account any post-depositional process. In hydrocarbon reservoirs, this is not the case because they have been buried several kilometers changing their porosities. Therefore, the initial porosity model was adjusted by compaction.

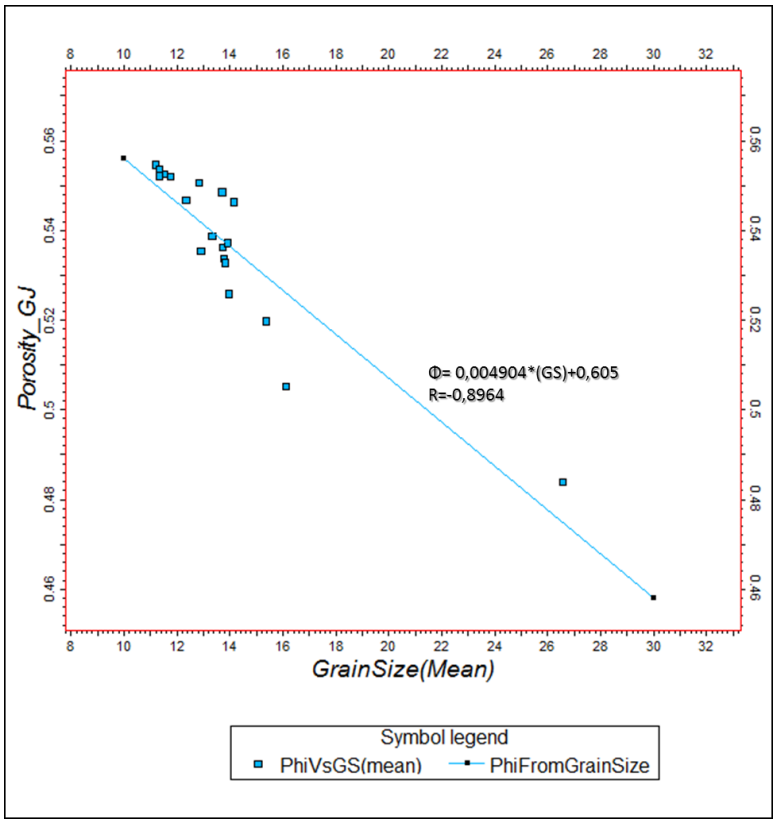

Figure 56. Porosity vs. Mean Grain Size at location samples. Crevasse Splay 1.

b. Initial Porosity Model Under Compaction

The porosities described in the initial porosity model (Fig 57) are too high to be considered as an input for hydrocarbon reserves estimation. Therefore, these porosities were adjusted by mechanical compaction at different depths. However, the mechanical compaction is not the only factor that modifies porosity. For this reason, and due to the lack of information about temperature gradients, cement minerals and dissolution process, porosity will be estimated assuming that the sediments are only affected by mechanical compaction process.

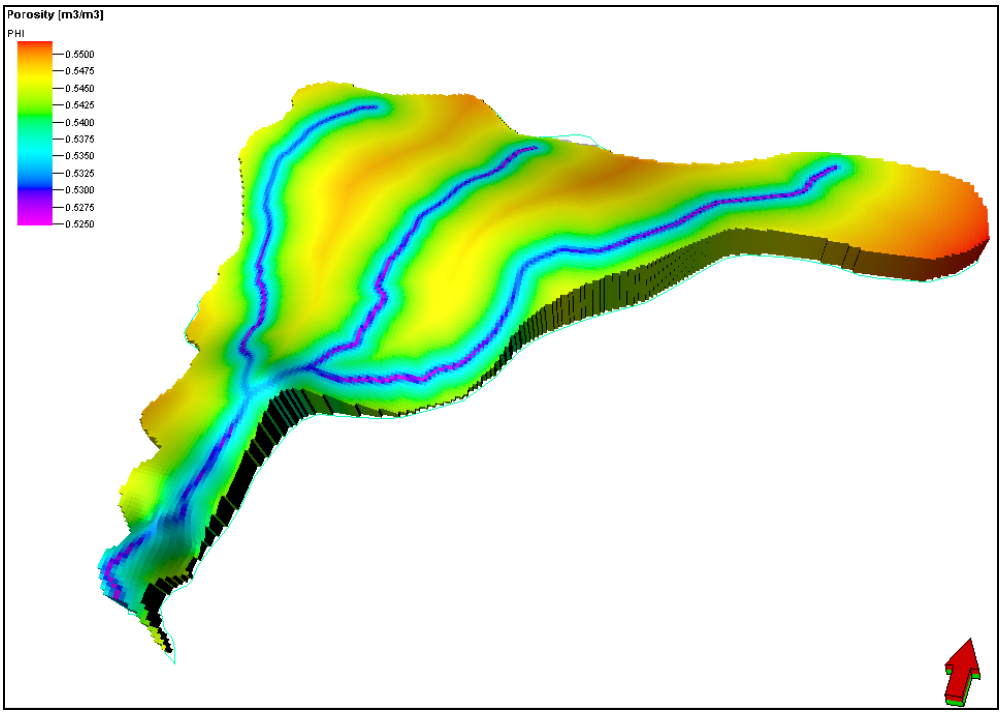

Figure 57. Initial Porosity Model. Crevasse Splay 1

Regarding to the compaction process, many authors have developed different approximations on sand and shale deposits. For example, Athy (1930) described that porosity of a shale is reduced exponentially with respect to the burial depth. According to this, many authors agree that the following expression captures the relation between porosity and mechanical compaction in fine-grained clastic reservoirs (Busch, 1989; Ramm, 1991).

$$\emptyset = \emptyset_o * e^{(-\alpha * Z)}$$

Where ϕ_0 is the initial porosity, Z is the depth at which porosity will be predicted and α is a constant that depends on to which extent the material has already been repacked (Bahr et al., 2001). This constant has been obtained empirically (Busch, 1989) and due to it depends on many factors such as texture, composition of the grains, effective stress, time, etc., three different constants ($2.7X10^{-4}$ – Ramm , 1991 ; $6.5X10^{-4}$ and $15.5\ X10^{-4}$ – Bahr, 2001) were used to evaluate porosity at different scenarios (Fig. 58).

As is shown in figure 58, porosity at subsurface conditions has the same distribution as initial porosity. This distribution is not true, because the inter-particles forces are weak and do not survive burial. Therefore, fine grains sediments experience more compaction than coarse grains sediments, (Kominz, Patterson, & Odette, 2011) resulting in lower porosities in finer grains than in coarser grains. According to this, porosity in crevasse splays at sub-surface conditions should show high porosities at the channels, while in the distal parts of the crevasse splays porosity will be lower, contrary to the porosity distributions showed in figure 58.

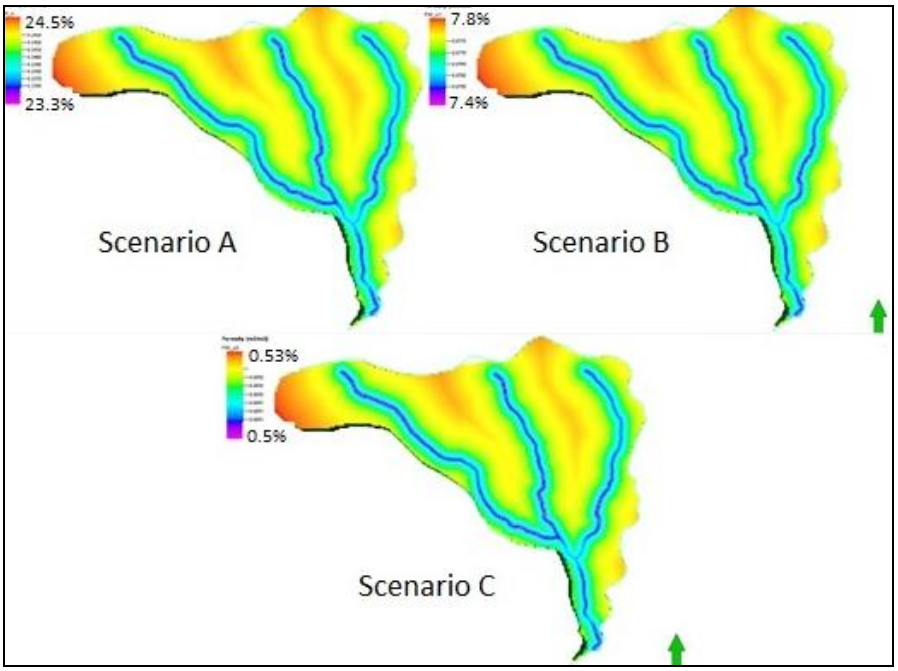

Figure 58. Porosity Model Scenarios under mechanical compaction at 3000 m depth. Crevasse Splay 1.

For this reason, another porosity estimation was performed based on the model developed by Kominz, Patterson, & Odette (2011). This model was derived empirically by correlating porosity and depth for diferent lithologies. In this case, we will use the following equation (Kominz, Patterson, & Odette, 2011), which works on rocks composed by +/-90% of silt.

$$\emptyset = 75.5e^{\left(\frac{-z}{1091}\right)}$$

After using this equation, the estimated porosity at 3000m is around 5%. This result is similar to the scenario B result, which shows porosities between 7.4 and 7.8%. This suggests that porosity in crevasse splays in dry river systems will be around 5 to 7%. Regarding to porosity distribution in crevasse splays, this will be assume constant due to the small variation (+/-0.4%) in porosity based on the scenario B. Likewise, the lack of information to properly describe porosity at subsurface conditions lead us to establish a constant porosity model to avoid erroneous porosity distributions that can impact the hydrocarbon volumes.

5.1.2. Permeability Model

The permeability model was obtained by using an expression derived in the literature, in which permeability is highly impacted by the grain size. For example, in the early 1942, Krumbein and Monk developed an equation that relates permeability with grain size and standard deviation. This equation was applied for median to coarse grain sand with a porosity of 40%. After that, this equation was discussed by Berg (1970), who showed that that formulation did not work properly with finer and poorly sorted sand, which could be the result of using uniform packing and the constant porosity.

In the same way, Carman (1937) modified the expression given by Kozeny (1927), who related permeability with a porous medium treated as a bundle of tubes, including a factor that accounts for the surface irregularity of rock, ending up with the following Carman-Kozeny (CK) equation.

$$k = \frac{\emptyset^3}{2\tau(1-\emptyset)^2 * a_v^2}$$

Where k is permeability in length squared units (mm^2), $\emptyset$ is porosity in fraction, τ is tortuosity (dimensionless) and a_v is the specific internal surface area of the medium (ratio of exposed area to solid volume) in $length^{-1}$ units. Afterwards, based on this formulation Dullien (1992) revised the CK equation and linking the specific surface area (a_v) with the mean particle size (d in length units) as $a_v=6/d$, the Carman-Kozeny (CK) equation becomes in:

$$k = \frac{d^2\emptyset^3}{180(1-\emptyset)^2}$$

This expression is one of the most accepted derivations of permeability but because this was derived on uniform grain sizes, it does not applied for mixed particle sizes. Therefore, any of the modified equations of Krumbein and Carman-Kozeny cannot be applied for fine natural sediments. This is the case of the crevasse splays that exhibit sediments that are in silt range and have a moderate to large standard deviation as was described in the previous chapter. Consequently, we will use the expression derived by Panda and Lake (1994), in which based on Carman-Kozeny modified equation, the mean particle size is expressed as a function of the second and the third moment of a particle size distribution such as $d=E_3/E_2$, where E_2 and E_3 can be described by the following expressions:

$$E_2 = e^{[-(2\varphi \ln(2) + 4\sigma^2 \ln(2)^2)]}$$

$$E_3 = e^{[-(3\varphi \ln(2) + 4.5\sigma^2 \ln(2)^2)]}$$

where φ is the mean grain size (phi scale), σ is the standard deviation (phi scale). Using the expressions above and simplifying terms the Carman-Kozeny modified equation can be described as:

$$k = \frac{\emptyset^3}{180(1-\emptyset)^2} e^{-[2\varphi \ln(2) + (\sigma \ln(2))^2]}$$

With this expression, permeability was estimated for all the samples using the grain size distributions described in the previous chapter. Permeability in turns is highly affected by porosity, which is largely impacted by different factors such as mechanical compaction. Therefore, permeability was calculated at surface and sub-surface conditions. At surface conditions, permeability was derived using the initial porosity and at sub-surface conditions (3000m), permeability was estimated using a constant porosity of 5% according with Kominz, Patterson, &

Odette, (2011). Based on these porosity models, permeability was obtained and it is shown in table 9.

Table 9. Permeability from Porosity model at surface conditions and at 3000m below surface.

Crevasse Splay 1			***Crevasse Splay 2***		
Sample	Permeability (mD) at Surface	Permeability (mD) at 3000 m	Sample	Permeability (mD) at Surface	Permeability (mD) at 3000 m
C1	425,06	0,0824	C2-1	438,303	0,114
C1-2	389,42	0,0771	C2-3	459,854	0,100
C1-4	390,08	0,0753	C2-4	380,609	0,077
C1-6	400,48	0,0685	C2-6	385,647	0,081
C1-7	373,45	0,0626	C2-8	421,605	0,094
C1-8	451,47	0,1187	C2-9	380,172	0,061
C1-9	348,95	0,0573	C2-10	408,299	0,089
C1-10	341,97	0,0550	C2-11	393,462	0,084
C1-11	365,93	0,0637	C2-12	351,323	0,060
C1-12	499,78	0,1223	C2-13	379,015	0,071
C1-13	375,09	0,0731	C2-15	355,700	0,059
C1-15	401,39	0,0803	C2-17	358,277	0,062
C1-17	397,31	0,0851	C2-18	451,152	0,118
C1-18	431,49	0,0982	C2-20	391,841	0,074
C1-19	421,49	0,0737	C2-22	353,975	0,058
C1-21	387,05	0,0740	C2-23	570,170	0,151
C1-22	389,69	0,0734	C2-24	369,054	0,067
C1-23	360,06	0,0596	C2-25	360,061	0,061
C1-25	673,66	0,2194	C2-26	390,878	0,059
C1-26	349,69	0,0569	C2-27	394,849	0,071
C1-27	346,59	0,0572			
C1-28	383,10	0,0652			

After obtaining permeability at the sample locations, this property was correlated with porosity at the same locations in order to find an equation to populate both crevasse splays at surface conditions. A permeability-porosity cross plot was made for Crevasse Splay 1 at surface conditions giving a correlation factor of 0.79. At sub-surface conditions (-3000m), a different cross plot permeability-mean grain size was made. This cross-plot was based on the theory that permeability is dependent on porosity and grain size distribution. Permeability at subsurface conditions was correlated to the grain size distribution due to porosity was taken as constant at this conditions. The results of this correlation gave a correlation factor of 0.91. On Crevasse Splay 2, permeability and porosity were correlated at surface conditions giving a correlation factor of 0.65 and at sub-surface conditions permeability and grain size gave a correlation factor of 0.85.

The results of the permeability models show that (Fig. 59 – Appendix 9) such property varies between 350 to 500 mD at surface conditions. This property decreases from the major channels to the distal areas, showing a close relationship with the grain size distribution that decreases gradually from the channel to the edges. At sub-surface conditions, the permeability model exhibits values from 0.05 mD to 0.13 mD showing the same distribution that at surface conditions.

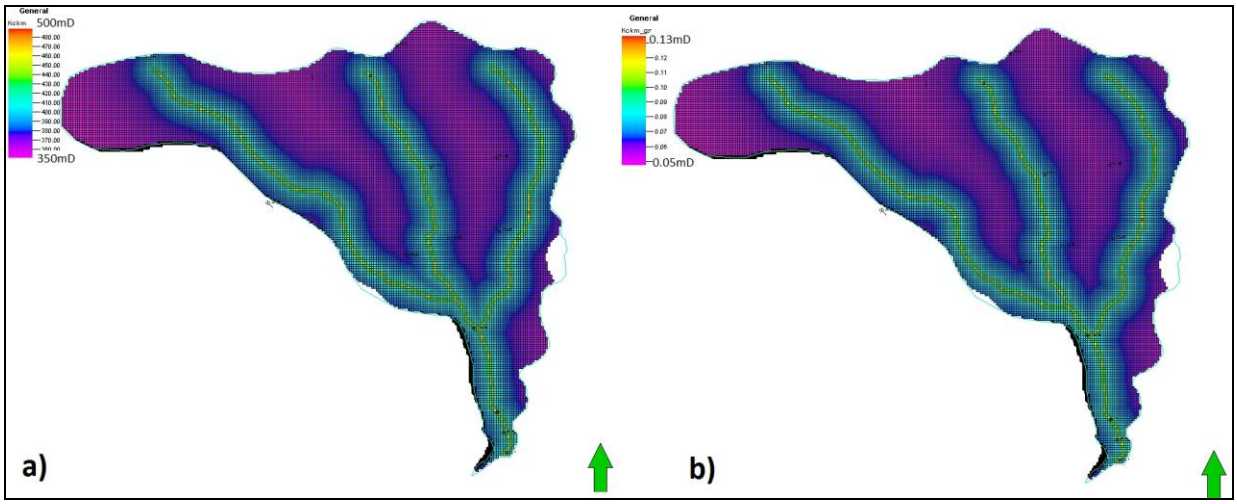

Figure 59. Permeability Model at a) surface conditions and b) subsurface conditions (3000m below surface level). Crevasse Splay 1.

5.2. Hydrocarbon Resources

Before start with the volumetric estimations, it is necessary to define which kind of fluid is going to be considered. Due to the low porosity and permeability of the crevasses at sub-surface conditions (ϕ=5-7% and K=0.05-0.13mD), this kind of reservoirs should be considered gas-bearing in order to be produced economically. Consequently, the amount of gas in place (GIIP) present in any siliciclastic reservoir can be obtained by the following formula, which in turns will be used to obtain the gas resources present in both single crevasse splays.

$$GIIP = BRV * NTG * \emptyset * Sg * Bgi$$

where *BRV* is the bulk rock volume (m^3), which is derived from the product between the reservoir area (m^2) and the gross thickness of the formation (m), *NTG* is the ratio of reservoir with certain shale volume cutoff over the total gross thickness of the reservoir, ϕ is porosity (fraction), S_g is the gas saturation (fraction) and Bg_i is the initial gas formation volumetric factor (sm^3/rm^3).

5.1.3. Deterministic Volumes

Most of the parameters that are present in such equation have a certain uncertainty because of the acquisition method or the low accuracy in the measurements. Therefore the *GIIP* was calculated deterministically at two different scenarios, which were based on the uncertainty of porosity.

The first parameter*, BRV* was taken as a fixed and it is the product of the area times the gross thickness. The area has a low uncertainty because it was delimited by satellite images in which the horizontal resolution is about 0.5m. Likewise, thickness has a low uncertainty as it was directly measured in the field.

The second parameter is net to gross, which in the crevasse splays will be taken as constant for both scenarios due to the absence of clay layers. Based on such observation, net to gross in a single

crevasse splay will be assume equal to one. Therefore this will not change significantly over the whole area.

The next parameter is porosity, which in contrast to the previous parameters has a large uncertainty. This uncertainty is related of how porosity is derived. Porosity at sub-surfaces conditions can be derived from initial porosity or relating this to a certain lithology with depth. Both methods use algorithms derived from experimental data. Therefore, the results of both methods, which fluctuate between 5 and 7% were compared with some analogue formations such as Travis peak formation at East Texas-US (Davles, Williams, & Vessel, 1993). This formation is composed by similar crevasse splay facies showing porosities between 4% and 10% at depths between 6000ft (1800m) and 8500ft (2600m). Such porosity range suggests that the estimated porosity can be used to define two deterministic volumes, one assuming a constant porosity of 5% and another with a constant porosity of 7%.

The gas saturation (S_g) was defined by assuming that the reservoir is completely filled by gas and it has an average connate water saturation (S_{wc}) of 0.2. Consequently, the gas saturation is equal to 0.8 and it will be taken as constant in all three scenarios due to the lack of information about it. In the same way, the gas formation volumetric factor (B_g), which is the last parameter to be considered in the *GIIP* calculations, will be derived from a rule of thumb. This rule states that the gas formation volumetric factor (B_g) is equal to depth (feet) of the reservoir divided by 36.9 for normal pressured reservoirs.

After all parameters were determined for both scenarios, the *GIIP* was obtained using the volumetrics module in petrel as it is shown in table 10.

Table 10. Deterministic Volumes Crevasse Splay one and two.

Deterministic Volumes					
Scenario		**Crevasse Splay 1**		**Crevasse Splay 2**	
		Parameter	GIIP[m3]	Parameter	GIIP[m3]
Kominz	BRV[m3]	1,50E+05	1,56E+06	7,70E+04	8,36E+05
	NTG[-]	1		1	
	ϕ [-]	0,05		0,05	
	Sg[-]	0,8		0,8	
	Bgi[sm3/rm3]	271		271	
Busch	BRV[m3]	1,50E+05	2,19E+06	7,70E+04	1,17E+06
	NTG[-]	1		1	
	ϕ [-]	0,07		0,07	
	Sg[-]	0,8		0,8	
	Bgi[sm3/rm3]	271		271	

5.1.4. Stochastic Volumes

The *GIIP* is better described by stochastic models due to the geological uncertainties. These models include the chance of finding gas resources related to different geological assumptions. The mean *GIIP* value for the crevasse splays can be determined using the same formula for the deterministic

volumes, which is included in a forecast spreadsheet developed at TU Delft (FDP Course, 2012). With this spread sheet, frequency distributions for all the input parameters were generated and GIIP results were obtained (Fig. 60). The GIIP results can be expressed by cumulative distributions curves. These curves in turn will provide the most well-known descriptors of gas resources in the oil industry such as P90, P50, P10 and mean.

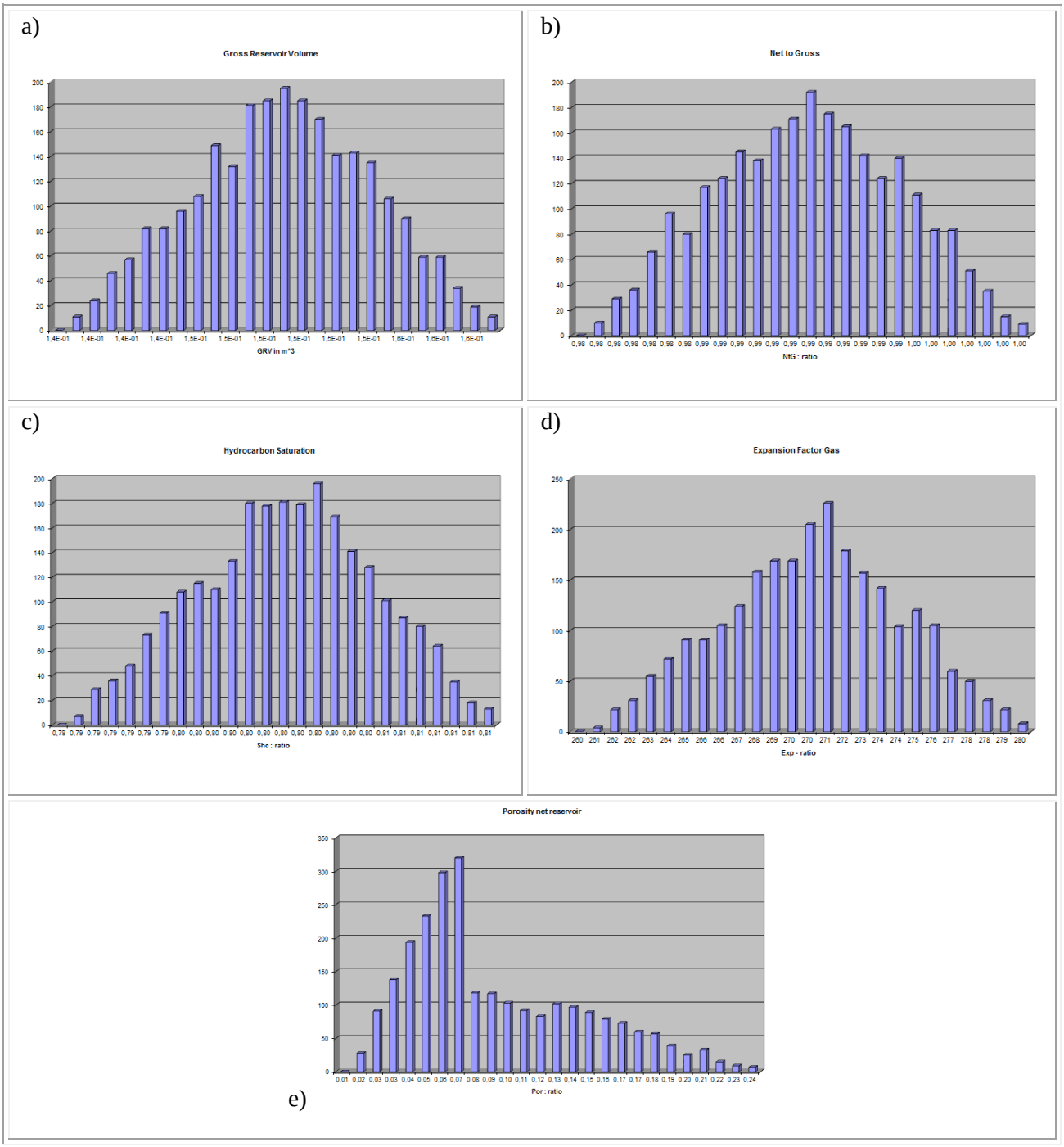

Figure 60. Input parameters for GIIP Monte Carlo simulation a) BRV, b)NTG, c)Sg, d) Bgi, e) Porosity. Crevasse Splay 1.

The first step to create a gas resource probability distribution is to define the minimum, most likely and maximum input parameter in the *GIIP* determination, which was defined by using the deterministic model. Most of the input parameters (*RBV*, *NTG*, S_g and B_{gi}) have a low uncertainty, which is expressed by narrow triangular distributions (Fig. 60), while porosity that has a large uncertainty can be represented by a wide lognormal distribution. The result of the Monte Carlo simulations show that the gas resources are represented by log-normal distributions skewed to the left for both crevasse splays (Fig 61).

The results of Monte Carlo simulations for gas resources associated to crevasse splays in one single flooding event can be expressed on cumulative curves (Fig. 61). From these curves, different probabilities of occurrence were extracted to define the Swanson's mean, which is defined by the following expression:

$$S_{Mean} = (0.3 * P10) + (0.4 * P50) + (0.3 * P90)$$

Consequently, the gas resources for Crevasse Splay 1 and 2 from Monte Carlo simulations and the Swanson's mean are compiles in table 11.

Table 11. Stochastic Volumes and Swanson's mean Crevasse Splay one and two.

Stochastic Volumes								
	Crevasse Splay 1				**Crevasse Splay 2**			
Input Parameter	P10	P50	P90	Swanson's Mean	P10	P50	P90	Swanson's Mean
BRV[MSCM]	0,1495	0,1500	0,1505		0,07672	0,07700	0,07727	
NTG[-]	0,9844	0,9901	0,9955		0,98434	0,99011	0,99576	
ϕ [-]	0,0357	0,0702	0,1625		0,03558	0,07089	0,16365	
Sg[-]	0,7846	0,7899	0,7955		0,78443	0,79003	0,79571	
Bgi[SCM/RCM]	267,74	271,07	274,33		267,71	270,95	274,23	
GIIP[MSCM]	1,099	2,216	5,217	2,810	0,576	1,154	2,633	1,460

5.3. Discussion

Based on the gas resources obtained on both crevasse splays, a comparison between these reserves and the average tight gas field reserves associate with crevasse splays such as the Ameland Field - 28 BCM (Glennie & Provan, 1990), Agua Dulce - 1.6 TCF and Stratton Filed – 1.8 TCF (Kerr, 1990) shows that gas resources in the Crevasse Splays 1 & 2 are relatively low. This can be related to the resources calculation that was based on one crevasse splay at one flooding event. This implies that the bulk rock volume per crevasse splay could increase considerably due to the total thickness of a crevasse splay is composed by many flooding events as it shown in the figure 62.

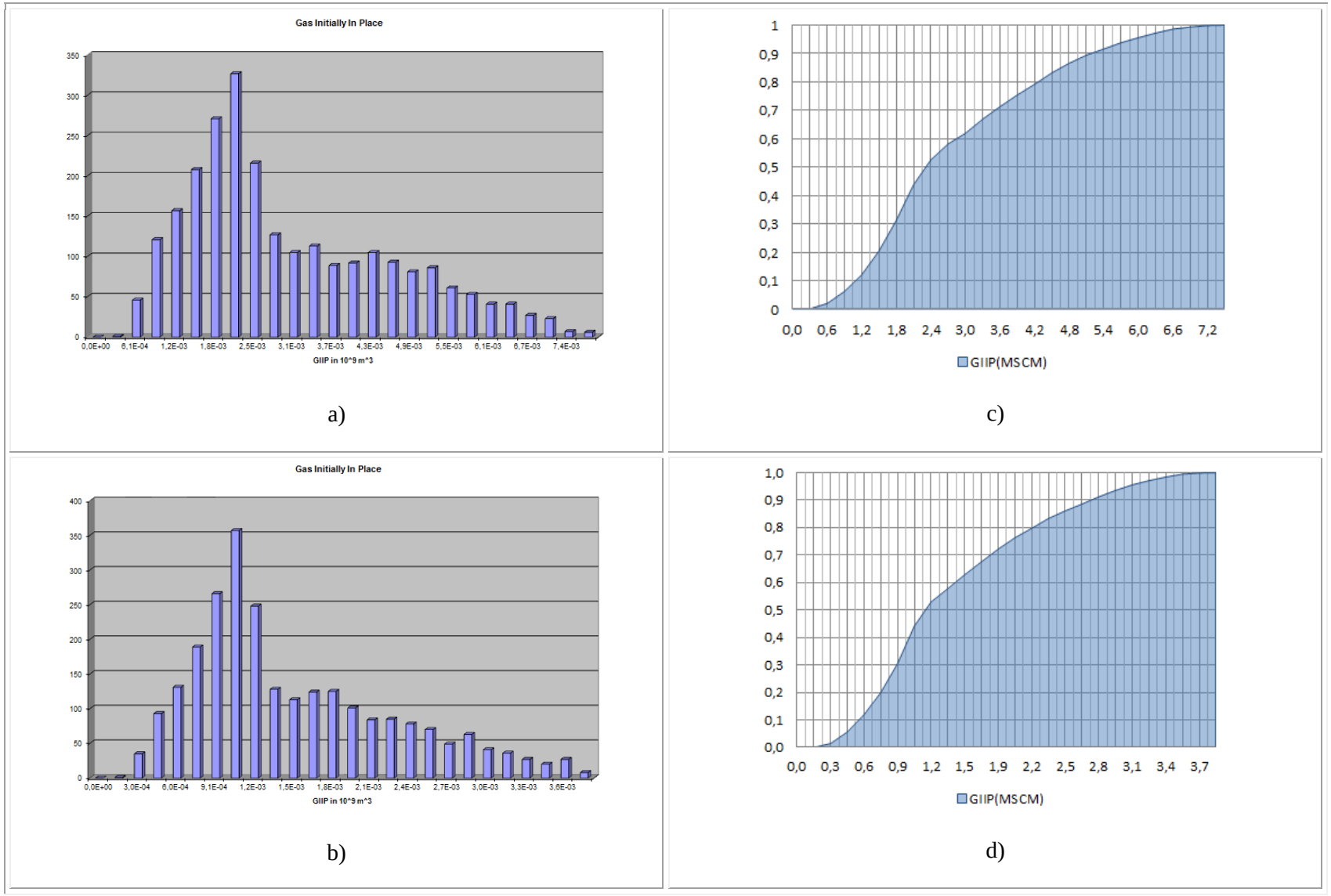

Figure 61. GIIP Monte Carlo simulation a) Histogram Crevasse Splay 1, b) Histogram Crevasse Splay 2, c) Cumulative Curve Crevasse Splay 1, d) Cumulative Curve Crevasse Splay 2.

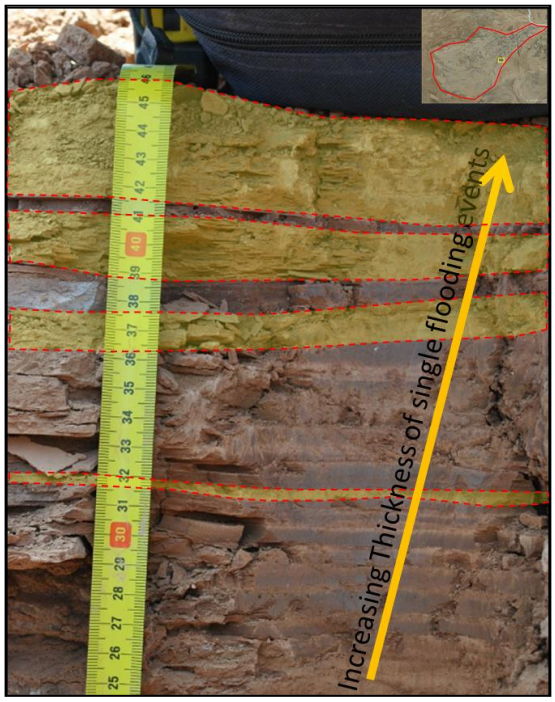

Figure 62. Flooding events (yellow) at Distal area of Crevasse Splay 2.

Several papers on crevasse splay were consulted to have a better understanding of the average thickness that a crevasse splay could reach. One of those is the study of the Middle Frio formation-US (Kerr, 1990) in which the total thickness of a splay deposit varies between 3 to 6 m. Another example is the Iles Formation north of Rangely, Colorado-US (Anderson, 2005), which describes that the average thickness of a crevasse splay is about 6 m. Based on these examples, we could infer that the total thickness of a crevasse splay is in order of meters. This shows that the gas resources depend on the number of flooding events that can happen during the formation of a crevasse splay. Consequently, the gas resources calculated on Crevasse Splays 1&2 could be at least hundred times bigger than the ones obtained on one flooding event.

Besides the gas volume that can be stored in the crevasse splays, the reservoir quality of such bodies should be considered because of the impact on the development plan of the gas resources. Properties such as porosity and permeability are in general terms homogeneous with a slight variation between the main channels to the edge of the crevasse splay, which could be represented by a single fluid flow compartment at least within bodies deposited at the same flooding event. Therefore, there is a high probability of having an accelerated gas production in crevasse splays than comparing to the production rates in isolated point bars. These unstable rates can be related to remarkable permeability variations, due to lateral accretion in isolated bars.

Likewise due to the areal extent of the crevasse splays, which covers nearly three times the area covered by an isolated point bar, it might be possible to have denser drilling campaigns (Anderson, 2005), which also might result in accelerated production. On the other hand, due to the large area

covered by the crevasse splays, it could be possible to have a better effective vertical contact within crevasse splays at different formation times, leading us to have a better stacked fluvial reservoirs.

6. Results & Conclusions

6.1. Results

After taking several sediment samples over the study area and analyzing them by different means, the highest proportion of both crevasse splays is represented by silt sediments with 79% in Crevasse Splay 1 and by 83% in Crevasse Splay 2. Likewise, the silt component in the Crevasse Splay 1 shows a grain size distribution that varies from 11.2 to 26.5µm and the silt component in Crevasse Splay 2 has a grain size distribution that varies from 11.4 to 21.7µm.

In addition, initial porosity was derived from grain size distribution, resulting in porosities from 48.4% to 55.4% in Crevasse Splay 1 and from 50.4% to 56.1% at Crevasse Splay 2. Permeability in Crevasse Splay 1 was obtained based on porosity and grain size distribution, giving permeabilities of 342mD to 674mD at surface conditions. Permeability on Crevasse Splay 2 varies from 351mD to 570mD at the same conditions.

Going back to the measurements taken into the field, the gross thickness in one flooding event at the Crevasse Splay 1 fluctuates from 2 cm to 18 cm with a mean value of 7.90 cm. In the same way, Crevasse Splay 2 shows a gross thickness from 1cm to 24 cm with a mean of 7.27cm. Additionally, along the total vertical sequence, on the crevasse splays two main facies were defined. The first one is represented by silt sediments deposited in moderate to low energy environment, which is characterized by cross lamination and climbing ripples. The second facies is defined by silt sediments with wavy and horizontal laminations.

Finally, the gas resources on both crevasse splays were calculated using the measurements at surface with the exception of porosity, which had to be transformed to subsurface conditions. However, this porosity model was not taken in account for *GIIP* calculations because of the lack of information. Instead of this model, porosity was taken from some analogues at subsurface conditions to calculate *GIIP,* giving mean resources of 2.8 MSCM on Crevasse Splay 1 and 1.4 MSCM at Crevasse Splay 2.

6.2. Conclusions

From the information giving above, it is possible to conclude that the models developed on the crevasse splays related to the Colorado River are good analogues for tight gas reservoirs. These models describe how can be the areal extension, grain size distribution, initial porosities, surface permeabilities and most likely gas resources of those sediment bodies deposited in one flooding event. In the same way, we can conclude that the information collected and analyzed is representative of such kind of reservoirs. This is explained by the good exposition of the crevasse splays, which is the result of the arid conditions that dominates the area, which in turns reduces the geological uncertainty during the gas resources estimation.

In the same way, the grain size distribution extracted from the crevasse splay models moves in the range of silt, which differs with some publications in which crevasse splays are characterized by very fine sand to fine sand. This finding is an important factor to keep in mind, due to some of the techniques applied in the field were based on a theoretical grain size distribution. Therefore, some of the devices and techniques used in the field did not give useful information about grain size. Contrary to this, the results obtained from the laser device were less time consuming and more accurate for such kind of sediments.

In addition to the range of the grain size distribution on the crevasse splays, it is plausible to say that grain size is extensively dependent to the distance with respect to the main channels splays, showing bigger particles at the channels and ending with smaller particles to the edges of the crevasse splays. The main physical process behind this grain size areal distribution is the waning process. This process is expressed on the facies found, showing cross lamination and climbing ripples facies at the base of the bodies at the proximal areas. These becomes gradually into parallel laminae facies in vertical section and at the distal areas of the splays. Besides the good correlation between grain size and distance to the channels, it would be possible to obtain a better predictor for grain size distribution, if raw specialized satellite data would be used instead of the RGBD data extracted from Google images.

Another conclusion that comes out from the crevasse splay models is that the initial porosity distribution, which was derived from the grain size distribution in silt sediments, increase with decreasing grain size due to inter-particles forces. This porosity does not exhibit a large variation within the crevasse splays, fact that makes these sediment bodies homogeneous. On the other hand, the results of the porosity at subsurface conditions should be recalculated to improve the *GIIP* estimations using data such as mineral composition, reservoir temperature and confining pressure.

Permeability that was derived from porosity and grain size distribution increases towards the main channel splays keeping the same homogenous behavior as porosity, which is beneficial for gas production purposes. However, it is important to keep in mind that the values of such property at surface conditions are not accurate for tight gas reservoirs. Therefore, the permeability model at subsurface conditions can be only used as an indicator of the order of magnitude of permeabilities present in such sediment bodies. This in turns must be updated after the subsurface porosity model would be updated to obtain more accurate permeability values, which can be used later on a gas flow simulation stage.

Finally, the GIIP results can be taken as an illustration for the gas resources present in one flooding event within a crevasse splay. Therefore, in order to obtain the total gas resources present in a crevasse splay, it is recommended to measure in the field the amount of flooding events that could be present in a crevasse splay, which would give a better estimation of the rock bulk volume in such bodies. Additionally, in future research projects is recommended to determine the gas resources of a crevasse splay complex considering that the large areal extension of this bodies has a large impact over the stacking architecture of such complexes.

6.3. Recommendations

On the grain size measurements, based on the results of the grain size distributions, the sampling acquisition grid should be re-designed based on the most remarkable channels identified along the crevasse splays to characterize better the grain size distribution. In addition, in order to improve the results obtained in this research, specialized satellite images should be acquired to find a better predictor for the grain distribution model. This images could reduce the noisy data present in commercial satellite images, which provoke low correlations with the mean grain size data.

Regarding to porosity at subsurface conditions, this model should be updated using data related to digenetic process such as mineralogy and temperature gradients. These information can be used as an input parameter in more robust algorithms that transform initial porosity to porosity at any depth. This will give better porosity results that also will impact the gas resources obtained beforehand.

The GIIP resources were calculated on one flooding event of a crevasse splay, therefore to have a better estimation of the resources associated with the crevasse splays, it is necessary to measure the amount of flooding events, which constitute them. In addition by measuring the amount of crevasse splays that form them, it will be possible to characterize these deposits in terms of internal baffles, which are related to the periods between crevasse splays deposition.

References

Anderson, D. (2005). Architecture of crevasse splay and point-Bar of the Nonmarine Iles Formation north of Rangely, Colorado: Implicaions for Reservoir Description. *The Mountain Geologist*, 109-122.

Argollo Bautista, J., & Irondo, M. (2008). *El Cuaternario de Bolivia y regiones vecinas.* Santafe.

Ashley, G. (1978). Interpretation of polymodal sediments. *The Journal of Geology* , Vol. 86, No. 4, pp. 411-421

Athy, J. (1930). Density, Porosity and Compaction of Sedimentary Rocks. *American association of Petroleum Geologist Bulletin*, 1-22.

Bahr, D., Hutton, E., Syvistdki, J., & Pratson, l. (2001). Exponential approximations to compacted sediment porosity profiles. *Computers & Geosciences*, 691-700.

Banerjee, I. (1977). Experimental study on the effect of deceleration on the vertical sequence of sedimentary structures in silty sediments. *Journal of Sedimentary Petrology Vol. 47 No. 2., Pages 771-783*

Baucom, P., & Rigsby, C. (1999). Climate and lake-levels history of the northern Altiplano, Bolivia, as recorded Holocene sediments of the rio Desaguadero. *Journal of sedimentary Research*, Vol 69, pp. 597-611.

Beard, D., & Weyl, P. (1973). Influence of Texture on Porosity and Permeability of Unconsolidated sand. *The American Association of Petroleum Geologist Bulletin*, 349-369.

Berg, R. (1970). Method of determining permeability from reservoir rock properties. *Gulf coast association of geological societies*, 303-317.

Blott, S. J., Croft, D. J., Pye, K., Saye, S. E., & Wilson, H. E. (2004). Particle size analysis by laser diffraction. *Geological Society*, 63-73.

Bridge, J. (1984). Large-Scale Facies Sequences in Alluvial Overbank Enviornments. *Journal of Sedimentary Petrology*, 583-588.

Bristow, C.S., Skelly, R.L., & Ethridge, F.G. (1999). Crevasse splays from the rapidly aggrading, sand-bed, braided Niobrara River, Nebraska: effect of base-level rise. *Sedimentology*, 1029-1047.

Busch, W. (1989). Patterns of sediment compaction at Ocean Drilling Program Sites 645, 646, and 647, Baffin Bay and Labrador Sea. . *Proc. ODP, Sci*, 781–790.

Carman, P. (1937). *Fluid flow through granular beds.* Transactions of the Institute of Chemical Engineers London, 15, 150 - 156..

Davles, D., Williams, B., & Vessel, R. (1993). Reservoir Geometry and Internal Permeability Distribution in Fluvial, Tight, Gas Sandstones, Travis Peak Formation, Texas. *Reservoir Engineering*, 7-12.

Donselaar, M., Cuevas Gonzalo, M., & Moyano, S. (2012). Avulsion processes at the terminus of low-gradient semi-arid fluvial systems: Lessons from the Río Colorado, Altiplano endorheic basin, Bolivia. *Sedimentary geology*, 1-14.

Duleba, A., & Olive, D. (1996). Regression analysis and multivariate analysis. *Semin Reprod Endocrinol*, (pp. 139-153). Connecticut.

Dullien, F. (1991). *Porous Media: Fluid Transport and Pore structure.* San Diego: Academic Press. pp 250-275

Ericksen, G., & Salas, R. (1989). Geology and Resources of Salars in the Central Andes. *Circum-Pacific Council for Energy and Mineral Resorces*, (pp. 155-164). Houston.

Farrell, K. M. (1984). Sedimentology and facies architecture of overbank deposits of the Mississippi River, False River region, Louisiana. *The Society of Economic Paleontologists and Mineralogists*, 111-120.

Farrell, K. M. (2001). Geomorphology, facies architecture, and high-resolution, non-marine sequence stratigraphy in avulsion deposits, Cumberland Marshes. *Sedimentary Geology 139*, pp. 93-150.

Fraser, H. (1935). Experimental study of the porority and permeability of clastic sediments. *Journal Geology*, 910-1010.

Glennie, K., & Provan, D. (1990). Lower Permian Rotliegend reservoirof the Southern North Sea gas province. *The Geological Society*, 399-416.

Hembree, C. H., Colby, B. R., Swenson, H. A., & Davis , J. R. (1952). Sedimentation and Chemical quality of water odf the Powder River drainage basin, Wyoming and Montana. *US Geological Survey*, 150-158.

Hoffstetter, R. (1971). Le gisement d'Ayo Ayo (Bolivie), une succession stratigraphique Pliocéne-Pléistocéne datée par des mammiféres. *Comptes Rendus Académie des Sciences*, (pp. 2472–2475). Paris.

Jaillard, E., Hérail, G., Monfret, T., Díaz Martínez, E., Baby, P., Lavenu, A. (2000). Tectonic evolution of the Andes of Ecuador, Peru, Bolivia and northernmost Chile. In U. Cordani, E. Milani, A. Thomaz Filho, & D. Campos, *Tectonic Evolution of South America* (pp. 481–559). Rio de Janeiro.

Johansen, S. (1983). The thick-splay depositional style of the Crevasse Canyon Formation, Cretaceous of west-central New Mexico. *New Mexico Geological Society Guidebook*, 173-178.

Kerr, D. (1990). Reservoir Heterogeneity in the Middle Frio Formation case studies in Stratton and Agua Dulce Fields, Nueces Country, Texas. *Gulf Coast association of geological Societies*, 363-372.

Kominz, M. A., Patterson, K., & Odette, D. (2011). Lithology Dependence of Porosity in Slope and Deep Marine Sediments. *Journal of Sedimentary Research*, 730-742.

Kozeny, J. (1927). *Ueber kapillare Leitung des Wassers im Boden.* Wien: Sitzungsber Akad.

Lavenu, A. (1984). Age pliocene de la Formation Remedios dans l'Altiplano bolivien. *C.R Acad. Sciences*, 1051-1054.

Lavenu, A. (1991). Formacion Geologica y Evolucion. In C. Dejoux, & A. Iltis, *El Lago Titicaca: síntesis del concocimiento limnológico actual* (pp. 19-27). La Paz: Hisbol.

Marshak, J. W., Kuykendall, J., & Zhixiong, S. (2011). Grain Size of Crevasse-Splay Deposits in the Mississippi Delta; Implications for Coastal Restoration. *The Geological Society of America* , 8-11.

Marshall, L., & Sempere, T. (1991). The Eocene to Pleistocene vertebrates of Bolivia and their stratigraphic context : a review. *Revista Tecnica de Yacimientos Petroliferos Fiscales Bolivianos*, 631-652.

McCabe, P. J. (1987). Facies studies of coal and coal-bearing strata. *Geological Society*, 51-66.

McCave, I. (2008). Size sorting during transport and deposition of fine sediments: Sortable silt and flow speed. *Developments in Sedimentology*, 121-142.

McCave, I., Manighetti, B., & Robinson, S. (1995). Sortable silt and fine sediment size/composition slicing: parameters for palaeocurrrent speed and Paleoceanography. *Paleoceanography*, 593-610.

Middleton, G. (1976). Hydraulic interpretation of sand size distributions. *Journal of Geology*, 405-426.

O'Brien, P., & Wells, A. (1986). A small, alluvial crevasse splay. *Journal of Sedimentary Petrology*, 876-879.

Panda, M. N., & Lake, L. W. (1994). Estimation of Single-Phase Permeability from Parameters of Particle-Size Distribution. *The American Association of Petroleum Geologist*, 1028-1037.

Pawlowsky-Glahn, V., & Egozcue, J. (2006). Compositional data and their analysis: an introduction. *Geological Society*, 1-10.

Ramm, M. (1991). Porosity distribution in Jurassic sandstones of the Viking Graven, North sea. In M. Ramm, *Porosity trends in Sanstones* (pp. 550-570). Oslo: Univ Oslo.

Rehna, V., & Jeyakumar, M. (2012). Singular Value Decomposition Based Image Coding For Achieving Additional Compression To JPEG Images. *International Journal of Image Processing and Vision Sciences*, 2278 – 1110.

Rodriguez, A. (1985). Las Cuencas Intramontanas Andinas. *II Simposio Bolivariano.* Bogota. 12-15

Rogers, J. (1961). Relationships between porosity, median size and sorting coefficients of synthetic sands. *Journal of Sedimentary Petrology*, 467-470.

Scherer, M. (1987). Parameters Influecing Porosity in Sandstones: A Model for Sandstone Porosity Prediction. *The American Association of Petroleum Geologist Bulletin*, 485-491.

Servant, M., & Fontes, J. (1978). Les lacs quaternaries des hauts plateaux des Andes Boliviennes. *Cah. Orstom, Serv Geol*, 9-23.

Smith, N., Cross, T., Dufficy, J., & Clough, S. (1989). Anatomy of Avulsion. *Sedimentology*, 1-23.

Sun, D., Bloemendal, J., Rea, D., Vandenberghe, J., Jiang, F., An, Z., et al. (2002). Grain-size distribution function of polymodal sediments in hydraulic and aeolian environments, and numerical partitioning of the sedimentary components. *Sedimentary Geology*, 263-277.

van Gelder, A., van den Berg, J. H., Cheng, G., & Xue, C. (1994). Overbank and channelfill deposits of the modern Yellow River delta. *Sedimentary Geology*, 293-305.

Weltje, G. J., & Alberts, L. J. (2011). Packing states of ideal reservoir sands: Insights from simulation of porosity reduction by grain rearrangement. *Sedimentary Geology*, 52-64.

Weltje, G. J., & Prins, M. A. (2007). Genetically meaningful decomposition of grain-size distributions. *Sedimentary Geology*, 409-424.

Wu, W., & Wamg, S. (2006). Formulas for sediment porosity and settling velocity. *Hydraulic Engineering*, 858-862.

Yu, A. B., & Standish, N. (1993). Limitation of Proposed Mathematical Models for the Porosity Estimation of Nonspherical Particle Mixtures. *Ind. Eng. Chem. Res*, 2179-2182.

Yu, A., & Standish, N. (1991). Estimation of the porosity of the particle mixtures by a linear-mixture packing model. *Ind. Eng. Chem. Res.*, 1372-1385.

Yu, A., Feng, C., Zou, R., & Yang, R. (2003). On the relationship between porosity and interparticle forces. *Powder Technology*, 70-76.

Appendices

Appendix 1

Sample Locations

Appendix 1A. Sample map location Crevasse Splay 1 along the Colorado River

Appendix 1B. Sample map location Crevasse Splay 2 along the Colorado River

Appendix 1C. Lacquer Peel map location Crevasse Splay 1 along the Colorado River

Appendix 1D. Lacquer Peel map location Crevasse Splay 2 along the Colorado River

Appendix 2

Results from Data Laser Analysis
Crevasses Splay 1 & 2

		phi	13	12,75	12,5	12,25	12	11,75	11,5	11,25	11	10,75	10,5	10,25	10	9,75	9,5	9,25	9	8,75	8,5	8,25	8	7,75	7,5	7,25	7	6,75	6,5	6,25	6	5,75
Lab.nr.	**Field Code**	µm	0,12	0,15	0,17	0,21	0,24	0,29	0,35	0,41	0,49	0,58	0,69	0,82	0,98	1,2	1,4	1,6	2	2,3	2,8	3,3	3,9	4,7	5,5	6,6	7,8	9,3	11,1	13,1	15,6	18,6
164264	C1_11	.	0,32	0,34	0,41	0,43	0,5	0,57	0,65	0,76	0,88	1,08	1,33	1,66	2,12	2,62	3,17	3,66	4,05	4,27	4,48	4,71	4,95	5,11	5,16	5,08	5,01	5,04	5,02	4,93	4,69	4,28
164263	C1_13	.	0,27	0,28	0,34	0,36	0,42	0,47	0,53	0,62	0,72	0,89	1,11	1,39	1,78	2,21	2,68	3,1	3,45	3,66	3,89	4,19	4,56	4,98	5,39	5,75	6,17	6,6	6,77	6,56	5,93	4,91
164262	C1_15	.	0,21	0,22	0,26	0,28	0,32	0,37	0,42	0,51	0,6	0,77	1	1,32	1,78	2,33	3	3,68	4,41	5,03	5,56	6,03	6,39	6,55	6,54	6,34	6,13	5,97	5,65	5,08	4,19	3,14
164261	C1_17	.	0,23	0,24	0,29	0,31	0,36	0,41	0,48	0,57	0,68	0,87	1,11	1,44	1,91	2,45	3,06	3,62	4,14	4,49	4,77	5,07	5,39	5,66	5,83	5,85	5,84	5,85	5,69	5,31	4,67	3,82
164266	C1_2	.	0,2	0,21	0,25	0,27	0,31	0,35	0,4	0,47	0,55	0,68	0,84	1,06	1,37	1,7	2,08	2,41	2,7	2,88	3,08	3,34	3,63	3,9	4,11	4,24	4,42	4,7	4,99	5,24	5,39	5,41
164259	C1_21	.	0,19	0,2	0,24	0,25	0,29	0,33	0,38	0,45	0,52	0,65	0,81	1,02	1,32	1,64	2	2,32	2,59	2,76	2,95	3,18	3,46	3,74	4	4,21	4,5	4,94	5,38	5,75	6,01	6,02
164258	C1_23	.	0,2	0,21	0,25	0,27	0,31	0,35	0,4	0,48	0,57	0,73	0,95	1,25	1,68	2,2	2,84	3,48	4,18	4,8	5,38	5,91	6,29	6,32	6,02	5,38	4,64	3,98	3,36	2,82	2,33	1,95
164257	C1_26	.	0,4	0,41	0,5	0,54	0,62	0,7	0,81	0,95	1,11	1,37	1,71	2,15	2,76	3,43	4,17	4,83	5,39	5,7	5,97	6,25	6,49	6,48	6,17	5,51	4,86	4,56	4,47	4,1	3,09	1,87
164265	C1_5	.	0,2	0,21	0,25	0,26	0,31	0,34	0,4	0,46	0,54	0,67	0,84	1,06	1,37	1,71	2,09	2,43	2,73	2,93	3,13	3,39	3,7	4,01	4,27	4,47	4,74	5,12	5,51	5,81	5,98	5,88
164358	C1-1	.	0,2	0,21	0,25	0,27	0,31	0,34	0,39	0,46	0,54	0,67	0,84	1,07	1,39	1,76	2,17	2,56	2,92	3,18	3,45	3,76	4,1	4,4	4,59	4,65	4,71	4,85	4,98	5,05	4,99	4,78
164359	C1-10	.	0,18	0,18	0,22	0,24	0,27	0,31	0,35	0,42	0,49	0,63	0,8	1,04	1,4	1,82	2,33	2,85	3,43	3,98	4,54	5,12	5,64	5,98	6,08	5,94	5,76	5,64	5,46	5,21	4,85	4,39
164365	C1-12	.	0,2	0,21	0,26	0,27	0,31	0,35	0,4	0,47	0,56	0,7	0,89	1,15	1,53	1,98	2,52	3,06	3,62	4,13	4,65	5,24	5,89	6,48	6,86	6,97	6,92	6,76	6,33	5,61	4,57	3,4
164371	C1-14	.	0,16	0,16	0,2	0,21	0,24	0,27	0,32	0,37	0,43	0,54	0,68	0,86	1,12	1,41	1,73	2,03	2,3	2,49	2,69	2,92	3,17	3,39	3,57	3,68	3,84	4,1	4,36	4,61	4,89	5,14
164362	C1-16	.	0,2	0,2	0,25	0,26	0,31	0,34	0,39	0,46	0,54	0,68	0,85	1,07	1,39	1,74	2,13	2,49	2,81	3,02	3,24	3,51	3,82	4,14	4,39	4,57	4,8	5,13	5,41	5,57	5,55	5,27
164368	C1-18	.	0,2	0,21	0,26	0,27	0,32	0,36	0,41	0,49	0,57	0,72	0,91	1,17	1,54	1,95	2,41	2,84	3,24	3,51	3,76	4,04	4,33	4,57	4,72	4,75	4,79	4,88	4,88	4,85	4,79	4,66
164260	C1-19	.	0,18	0,19	0,23	0,24	0,28	0,31	0,36	0,43	0,5	0,64	0,82	1,06	1,41	1,81	2,28	2,72	3,14	3,44	3,71	3,97	4,23	4,4	4,47	4,4	4,35	4,37	4,37	4,34	4,24	4,06
164363	C1-20	.	0,24	0,25	0,31	0,32	0,38	0,42	0,49	0,58	0,68	0,85	1,07	1,37	1,8	2,28	2,84	3,37	3,86	4,23	4,58	4,97	5,38	5,71	5,9	5,91	5,87	5,8	5,56	5,18	4,65	4,01
164370	C1-22	.	0,24	0,25	0,31	0,32	0,37	0,42	0,48	0,57	0,67	0,84	1,07	1,39	1,86	2,41	3,08	3,76	4,48	5,14	5,78	6,45	7,12	7,62	7,82	7,64	7,16	6,42	5,33	4,11	2,9	1,89
164369	C1-24	.	0,17	0,18	0,21	0,22	0,26	0,29	0,34	0,4	0,48	0,61	0,79	1,03	1,39	1,83	2,37	2,92	3,54	4,16	4,79	5,46	6,11	6,58	6,8	6,75	6,62	6,47	6,14	5,58	4,74	3,75
164364	C1-25	.	0,26	0,27	0,33	0,35	0,4	0,46	0,53	0,63	0,75	0,95	1,21	1,58	2,1	2,7	3,39	4,05	4,7	5,17	5,57	5,97	6,32	6,49	6,46	6,19	5,86	5,55	5,1	4,52	3,81	3,01
164367	C1-27	.	0,31	0,33	0,4	0,42	0,49	0,55	0,64	0,76	0,89	1,12	1,41	1,81	2,37	3	3,74	4,43	5,09	5,55	5,97	6,39	6,77	6,98	6,95	6,6	6,08	5,41	4,5	3,51	2,57	1,79
164361	C1-3	.	0,16	0,16	0,2	0,21	0,24	0,27	0,31	0,36	0,43	0,54	0,69	0,9	1,21	1,58	2,03	2,49	3	3,49	3,99	4,54	5,11	5,62	5,95	6,11	6,25	6,42	6,47	6,33	5,92	5,22
164366	C1-30	.	0,17	0,18	0,22	0,22	0,24	0,26	0,29	0,32	0,36	0,44	0,56	0,74	1	1,33	1,75	2,15	2,6	2,97	3,31	3,63	3,89	4,04	4,08	3,99	3,89	3,83	3,75	3,72	3,8	4,01
164357	C1-4	.	0,18	0,19	0,23	0,25	0,28	0,32	0,36	0,42	0,5	0,63	0,79	1,03	1,37	1,77	2,26	2,74	3,25	3,71	4,18	4,71	5,25	5,73	6,04	6,16	6,24	6,33	6,29	6,03	5,46	4,62
164355	C1-6	.	0,16	0,17	0,2	0,21	0,24	0,27	0,31	0,37	0,43	0,54	0,69	0,9	1,21	1,57	2,01	2,44	2,92	3,37	3,83	4,34	4,87	5,36	5,73	5,98	6,23	6,51	6,61	6,45	5,99	5,21
164354	C1-7	.	0,17	0,18	0,21	0,23	0,26	0,29	0,34	0,4	0,47	0,59	0,75	0,96	1,27	1,62	2,03	2,42	2,81	3,12	3,43	3,76	4,09	4,36	4,53	4,6	4,72	4,94	5,15	5,31	5,39	5,31
164356	C1-8	.	0,19	0,2	0,25	0,26	0,3	0,34	0,39	0,47	0,55	0,7	0,9	1,16	1,54	1,98	2,5	2,99	3,48	3,86	4,22	4,59	4,95	5,23	5,4	5,44	5,5	5,64	5,73	5,69	5,44	4,94
164360	C1-9	.	0,31	0,32	0,39	0,42	0,49	0,55	0,64	0,76	0,89	1,11	1,39	1,76	2,27	2,83	3,46	4,03	4,52	4,82	5,09	5,4	5,73	5,98	6,11	6,05	5,9	5,69	5,23	4,62	3,91	3,16
164372	C1-end	.	0,27	0,28	0,34	0,37	0,42	0,48	0,54	0,64	0,74	0,91	1,13	1,42	1,82	2,26	2,75	3,19	3,56	3,78	3,99	4,26	4,56	4,85	5,07	5,19	5,31	5,44	5,42	5,26	4,95	4,49
164377	C6	,	0,29	0,31	0,37	0,4	0,46	0,52	0,6	0,71	0,83	1,03	1,29	1,63	2,11	2,65	3,26	3,81	4,31	4,63	4,92	5,23	5,52	5,69	5,7	5,5	5,22	4,92	4,49	3,97	3,39	2,81
164387	C6-1	,	0,17	0,18	0,22	0,23	0,27	0,3	0,35	0,41	0,48	0,6	0,75	0,96	1,26	1,59	1,97	2,32	2,64	2,86	3,09	3,36	3,67	3,97	4,21	4,37	4,59	4,94	5,31	5,58	5,71	5,63
164209	C6-10	.	0,2	0,2	0,25	0,26	0,3	0,34	0,39	0,46	0,54	0,69	0,89	1,17	1,57	2,06	2,66	3,27	3,93	4,56	5,17	5,83	6,5	7,05	7,37	7,4	7,22	6,84	6,08	5,07	3,91	2,81
164210	C6-11	.	0,19	0,2	0,24	0,26	0,3	0,34	0,39	0,47	0,56	0,72	0,94	1,23	1,66	2,17	2,8	3,44	4,15	4,79	5,41	6,01	6,54	6,82	6,84	6,55	6,16	5,79	5,3	4,66	3,81	2,9
164376	C6-12	,	0,3	0,32	0,39	0,41	0,47	0,53	0,61	0,72	0,85	1,06	1,33	1,71	2,23	2,83	3,54	4,2	4,85	5,34	5,78	6,22	6,59	6,7	6,52	5,98	5,29	4,59	3,82	3,05	2,28	1,64
164384	C6-13	,	0,2	0,21	0,25	0,26	0,3	0,34	0,39	0,46	0,54	0,67	0,86	1,11	1,47	1,9	2,41	2,92	3,44	3,89	4,34	4,84	5,35	5,81	6,09	6,17	6,19	6,21	6,08	5,74	5,13	4,31
164211	C6-14	.	0,17	0,18	0,22	0,23	0,26	0,3	0,34	0,4	0,47	0,59	0,75	0,96	1,27	1,61	2,02	2,4	2,77	3,06	3,37	3,73	4,14	4,56	4,9	5,16	5,45	5,82	6,09	6,19	6,05	5,61
164212	C6-15	.	0,16	0,16	0,2	0,21	0,24	0,27	0,31	0,36	0,43	0,55	0,71	0,93	1,27	1,69	2,23	2,78	3,43	4,07	4,73	5,43	6,13	6,72	7,07	7,15	7,09	6,93	6,51	5,81	4,79	3,62
164391	C6-16	,	0,19	0,2	0,25	0,26	0,3	0,34	0,39	0,46	0,54	0,66	0,83	1,04	1,34	1,66	2,01	2,33	2,59	2,76	2,93	3,15	3,4	3,64	3,82	3,91	4,05	4,3	4,59	4,86	5,08	5,22
164390	C6-17	,	0,18	0,18	0,22	0,24	0,27	0,31	0,36	0,42	0,5	0,63	0,81	1,04	1,38	1,76	2,2	2,62	3,04	3,36	3,67	4,04	4,46	4,87	5,18	5,38	5,59	5,83	5,95	5,86	5,52	4,93
164374	C6-18	,	0,18	0,19	0,23	0,24	0,28	0,31	0,36	0,43	0,51	0,65	0,83	1,09	1,46	1,9	2,43	2,95	3,51	4	4,48	4,97	5,4	5,66	5,72	5,55	5,34	5,16	4,92	4,63	4,27	3,88
164213	C6-19	.	0,32	0,34	0,41	0,44	0,51	0,57	0,66	0,77	0,91	1,13	1,41	1,78	2,3	2,88	3,53	4,12	4,65	4,98	5,28	5,59	5,86	5,96	5,86	5,52	5,13	4,82	4,47	4,04	3,46	2,79
164207	C6-2	.	0,17	0,18	0,22	0,23	0,27	0,3	0,35	0,43	0,51	0,66	0,85	1,12	1,51	1,98	2,58	3,18	3,87	4,51	5,11	5,65	6,06	6,22	6,2	5,98	5,74	5,51	5,14	4,68	4,17	3,63
164379	C6-20	,	0,19	0,2	0,25	0,26	0,3	0,34	0,39	0,46	0,54	0,67	0,83	1,05	1,36	1,69	2,07	2,4	2,7	2,9	3,1	3,35	3,64	3,92	4,14	4,28	4,47	4,77	5,05	5,27	5,39	5,35
164214	C6-21	.	0,27	0,28	0,35	0,37	0,43	0,48	0,56	0,67	0,79	1,01	1,29	1,68	2,24	2,88	3,63	4,34	5,03	5,55	5,99	6,43	6,81	6,96	6,86	6,43	5,84	5,18	4,36	3,55	2,78	2,13
164215	C6-22	.	0,25	0,27	0,32	0,34	0,39	0,44	0,51	0,61	0,72	0,92	1,19	1,55	2,09	2,72	3,48	4,23	5,01	5,65	6,24	6,83	7,36	7,63	7,57	7,09	6,36	5,49	4,43	3,38	2,4	1,63
164389	C6-23	,	0,21	0,21	0,26	0,28	0,32	0,36	0,42	0,5	0,6	0,77	0,99	1,29	1,73	2,25	2,89	3,53	4,22	4,84	5,42	6,01	6,57	6,98	7,16	7,02	6,7	6,22	5,43	4,44	3,34	2,34
164375	C6-25	,	0,38	0,4	0,49	0,52	0,6	0,68	0,78	0,92	1,07	1,33	1,65	2,1	2,72	3,41	4,21	4,96	5,65	6,12	6,5	6,85	7,07	6,98	6,58	5,79	4,84	3,88	2,91	2,09	1,48	1,12
164378	C6-26	,	0,2	0,21	0,26	0,27	0,31	0,35	0,39	0,46	0,54	0,69	0,88	1,15	1,56	2,05	2,66	3,29	4	4,69	5,41	6,18	6,96	7,55	7,78	7,56	7,06	6,41	5,56	4,55	3,33	2,18
164373	C6-27	,	0,2	0,21	0,26	0,27	0,31	0,34	0,39	0,46	0,54	0,68	0,88	1,17	1,6	2,12	2,79	3,48	4,28	5,07	5,86	6,68	7,45	7,96	8,11	7,81	7,23	6,44	5,37	4,21	3,06	2,08
164388	C6-28	,	0,28	0,29	0,35	0,37	0,43	0,49	0,56	0,66	0,78	0,97	1,22	1,56	2,03	2,57	3,18	3,75	4,29	4,67	5,03	5,43	5,85	6,17	6,33	6,25	6,06	5,79	5,29	4,63	3,82	3,02
164216	C6-29	.	0,31	0,32	0,39	0,42	0,49	0,56	0,65	0,77	0,91	1,14	1,43	1,83	2,38	2,99	3,68	4,32	4,88	5,25	5,59	5,97	6,34	6,59	6,64	6,39	5,97	5,41	4,6	3,7	2,79	2,02
164380	C6-3	,	0,15	0,16	0,2	0,21	0,24	0,27	0,31	0,37	0,44	0,56	0,71	0,92	1,21	1,56	1,97	2,37	2,79	3,15	3,51	3,89	4,22	4,41	4,42	4,23	4,03	3,93	3,89	3,91	4	4,16
164381	C6-4	,	0,2	0,21	0,25	0,26	0,3	0,34	0,39	0,46	0,55	0,71	0,92	1,22	1,67	2,22	2,91	3,61	4,4	5,11	5,77	6,39	6,89	7,11	7	6,52	5,88	5,26	4,61	3,92	3,13	2,41
164208	C6-5	.	0,17	0,18	0,21	0,23	0,26	0,3	0,34	0,4	0,47	0,6	0,75	0,95	1,24	1,56	1,91	2,22	2,48	2,65	2,82	3,02	3,26	3,51	3,75	3,96	4,28	4,74	5,21	5,66	6,05	6,26
164208R	C6-5-RM	,	0,2	0,21	0,26	0,27	0,32	0,36	0,41	0,48	0,55	0,68	0,84	1,06	1,35	1,67	2,02	2,32	2,56	2,7	2,85	3,04	3,28	3,5	3,68	3,81	4,03	4,45	4,95	5,43	5,8	5,95
164385	C6-6	,	0,32	0,33	0,4	0,43	0,5	0,56	0,64	0,75	0,87	1,08	1,34	1,7	2,19	2,73	3,34	3,9	4,38	4,69	4,99	5,32	5,65	5,86	5,88	5,65	5,34	5,08	4,75	4,29	3,62	2,86
164382	C6-7	,	0,28	0,29	0,36	0,38	0,44	0,5	0,57	0,67	0,78	0,97	1,2	1,52	1,96	2,45	2,99	3,48	3,91	4,19	4,46	4,78	5,13	5,45	5,66	5,72	5,75	5,76	5,57	5,16	4,55	3,79
164383	C6-8	,	0,2	0,2	0,25	0,26	0,31	0,35	0,4	0,47	0,55	0,68	0,86	1,1	1,43	1,79	2,21	2,59	2,94	3,18	3,42	3,71	4,03	4,32	4,54	4,66	4,83	5,09	5,31	5,46	5,48	5,31
164386	C6-9	,	0,21	0,22	0,27	0,28	0,32	0,36	0,41	0,48	0,56	0,72	0,93	1,22	1,67	2,21	2,91	3,62	4,44	5,21	5,94	6,66	7,28	7,64	7,68	7,34	6,79	6,13	5,25	4,26	3,2	2,24

Lab.nr.	Field Code	phi	5,5	5,25	5	4,75	4,5	4,25	4	3,75	3,5	3,25	3	2,75	2,5	2,25	2	1,75	1,5	1,25	1	0,75	0,5	0,25	0	-0,25	-0,5	-0,75	-1
		µm	22,1	26,3	31,3	37,2	44,2	52,6	62,5	74,3	88,4	105	125	149	177	210	250	297	354	420	500	595	707	841	1000	1189	1414	1681	2000
164264	C1_11	.	3,76	3,13	2,37	1,63	1,19	0,54	0,12	0,01	0	0	0	0	0	0	0	0	0	0	0	0	0	0	0	0	0	0	0
164263	C1_13	.	3,77	2,69	1,68	0,95	0,62	0,29	0,05	0	0	0	0	0	0	0	0	0	0	0	0	0	0	0	0	0	0	0	0
164262	C1_15	.	2,21	1,47	0,86	0,52	0,41	0,29	0,13	0,03	0	0	0	0	0	0	0	0	0	0	0	0	0	0	0	0	0	0	0
164261	C1_17	.	2,98	2,22	1,53	1,04	0,83	0,53	0,25	0,1	0,06	0	0	0	0	0	0	0	0	0	0	0	0	0	0	0	0	0	0
164266	C1_2	.	5,36	5,14	4,64	3,92	3,48	2,56	1,78	1,09	0,57	0,2	0,07	0,01	0	0	0	0	0	0	0	0	0	0	0	0	0	0	0
164259	C1_21	.	5,82	5,37	4,63	3,72	3,2	2,23	1,43	0,79	0,41	0,2	0,09	0,01	0	0	0	0	0	0	0	0	0	0	0	0	0	0	0
164258	C1_23	.	1,71	1,5	1,29	1,2	1,3	1,51	1,8	2,16	2,44	2,24	1,73	1,06	0,44	0,09	0	0	0	0	0	0	0	0	0	0	0	0	0
164257	C1_26	.	1,17	0,75	0,37	0,19	0,12	0,05	0	0	0	0	0	0	0	0	0	0	0	0	0	0	0	0	0	0	0	0	0
164265	C1_5	.	5,54	4,92	4,03	3,06	2,52	1,74	1,19	0,78	0,54	0,38	0,26	0,15	0,05	0,01	0	0	0	0	0	0	0	0	0	0	0	0	0
164358	C1-1	.	4,55	4,23	3,76	3,22	2,99	2,48	2	1,45	0,89	0,39	0,17	0,03	0	0	0	0	0	0	0	0	0	0	0	0	0	0	0
164359	C1-10	.	3,88	3,29	2,58	1,9	1,52	0,87	0,33	0,07	0	0	0	0	0	0	0	0	0	0	0	0	0	0	0	0	0	0	0
164365	C1-12	.	2,4	1,63	1	0,66	0,58	0,53	0,4	0,24	0,16	0,08	0,01	0	0	0	0	0	0	0	0	0	0	0	0	0	0	0	0
164371	C1-14	.	5,37	5,49	5,44	5,17	5,09	4,22	3,13	1,96	1,12	0,6	0,36	0,16	0,02	0	0	0	0	0	0	0	0	0	0	0	0	0	0
164362	C1-16	.	4,81	4,24	3,58	2,98	2,73	2,17	1,58	1,03	0,74	0,63	0,53	0,33	0,1	0,01	0	0	0	0	0	0	0	0	0	0	0	0	0
164368	C1-18	.	4,48	4,16	3,66	3,07	2,76	2,02	1,32	0,74	0,45	0,35	0,3	0,23	0,05	0	0	0	0	0	0	0	0	0	0	0	0	0	0
164260	C1-19	.	3,91	3,72	3,44	3,16	3,15	2,9	2,59	2,18	1,73	1,18	0,73	0,31	0,07	0,01	0	0	0	0	0	0	0	0	0	0	0	0	0
164363	C1-20	.	3,34	2,67	1,96	1,36	1,06	0,57	0,16	0,02	0	0	0	0	0	0	0	0	0	0	0	0	0	0	0	0	0	0	0
164370	C1-22	.	1,14	0,65	0,27	0,04	0	0	0	0	0	0	0	0	0	0	0	0	0	0	0	0	0	0	0	0	0	0	0
164369	C1-24	.	2,8	1,98	1,26	0,84	0,72	0,61	0,43	0,23	0,12	0,05	0,01	0	0	0	0	0	0	0	0	0	0	0	0	0	0	0	0
164364	C1-25	.	2,2	1,46	0,82	0,43	0,28	0,11	0,03	0	0	0	0	0	0	0	0	0	0	0	0	0	0	0	0	0	0	0	0
164367	C1-27	.	1,2	0,75	0,4	0,24	0,22	0,19	0,13	0,02	0	0	0	0	0	0	0	0	0	0	0	0	0	0	0	0	0	0	0
164361	C1-3	.	4,34	3,38	2,36	1,54	1,15	0,67	0,29	0,07	0	0	0	0	0	0	0	0	0	0	0	0	0	0	0	0	0	0	0
164366	C1-30	.	4,41	4,87	5,31	5,55	5,81	5	3,6	2,01	0,92	0,41	0,24	0,12	0,02	0	0	0	0	0	0	0	0	0	0	0	0	0	0
164357	C1-4	.	3,72	2,84	1,97	1,32	1,05	0,74	0,49	0,27	0,16	0,07	0,01	0	0	0	0	0	0	0	0	0	0	0	0	0	0	0	0
164355	C1-6	.	4,29	3,33	2,36	1,6	1,27	0,87	0,53	0,28	0,17	0,11	0,06	0,01	0	0	0	0	0	0	0	0	0	0	0	0	0	0	0
164354	C1-7	.	5,1	4,69	4,05	3,32	2,94	2,25	1,67	1,12	0,68	0,32	0,13	0,04	0	0	0	0	0	0	0	0	0	0	0	0	0	0	0
164356	C1-8	.	4,26	3,44	2,53	1,73	1,33	0,82	0,42	0,17	0,12	0,15	0,11	0,06	0	0	0	0	0	0	0	0	0	0	0	0	0	0	0
164360	C1-9	.	2,42	1,7	1,02	0,54	0,34	0,15	0,02	0	0	0	0	0	0	0	0	0	0	0	0	0	0	0	0	0	0	0	0
164372	C1-end	.	3,93	3,3	2,61	1,98	1,68	1,12	0,6	0,27	0,24	0,2	0,17	0,13	0,06	0,01	0	0	0	0	0	0	0	0	0	0	0	0	0
164377	C6	,	2,32	1,91	1,51	1,21	1,13	0,98	0,82	0,7	0,71	0,75	0,66	0,46	0,21	0,04	0	0	0	0	0	0	0	0	0	0	0	0	0
164387	C6-1	,	5,45	5,1	4,48	3,69	3,24	2,38	1,67	1,04	0,58	0,26	0,07	0,01	0	0	0	0	0	0	0	0	0	0	0	0	0	0	0
164209	C6-10	.	1,95	1,31	0,77	0,44	0,32	0,19	0,04	0	0	0	0	0	0	0	0	0	0	0	0	0	0	0	0	0	0	0	0
164210	C6-11	.	2,17	1,6	1,1	0,8	0,73	0,67	0,57	0,41	0,22	0,08	0,01	0	0	0	0	0	0	0	0	0	0	0	0	0	0	0	0
164376	C6-12	,	1,24	0,98	0,78	0,73	0,81	0,91	0,95	0,96	0,96	0,8	0,5	0,18	0,03	0	0	0	0	0	0	0	0	0	0	0	0	0	0
164384	C6-13	,	3,47	2,66	1,86	1,25	0,98	0,67	0,42	0,25	0,19	0,17	0,13	0,04	0	0	0	0	0	0	0	0	0	0	0	0	0	0	0
164211	C6-14	.	5,01	4,28	3,39	2,53	2,09	1,47	1	0,63	0,36	0,14	0,05	0	0	0	0	0	0	0	0	0	0	0	0	0	0	0	0
164212	C6-15	.	2,61	1,81	1,14	0,73	0,6	0,46	0,3	0,17	0,12	0,06	0,01	0	0	0	0	0	0	0	0	0	0	0	0	0	0	0	0
164391	C6-16	,	5,33	5,29	4,99	4,37	3,96	2,88	1,89	1,13	0,8	0,76	0,72	0,52	0,22	0,04	0	0	0	0	0	0	0	0	0	0	0	0	0
164390	C6-17	,	4,23	3,49	2,68	2	1,71	1,32	1,02	0,76	0,65	0,58	0,45	0,24	0,06	0,01	0	0	0	0	0	0	0	0	0	0	0	0	0
164374	C6-18	,	3,53	3,16	2,69	2,22	2	1,58	1,21	0,86	0,6	0,35	0,19	0,09	0,01	0	0	0	0	0	0	0	0	0	0	0	0	0	0
164213	C6-19	.	2,22	1,74	1,3	1	0,92	0,79	0,63	0,46	0,3	0,13	0,06	0,01	0	0	0	0	0	0	0	0	0	0	0	0	0	0	0
164207	C6-2	.	3,1	2,57	2,02	1,57	1,39	0,99	0,54	0,22	0,2	0,16	0,14	0,1	0,01	0	0	0	0	0	0	0	0	0	0	0	0	0	0
164379	C6-20	,	5,19	4,85	4,28	3,56	3,17	2,4	1,75	1,19	0,86	0,63	0,46	0,25	0,07	0,01	0	0	0	0	0	0	0	0	0	0	0	0	0
164214	C6-21	.	1,61	1,17	0,76	0,49	0,39	0,25	0,14	0,02	0	0	0	0	0	0	0	0	0	0	0	0	0	0	0	0	0	0	0
164215	C6-22	.	1,09	0,7	0,37	0,22	0,19	0,15	0,1	0,05	0	0	0	0	0	0	0	0	0	0	0	0	0	0	0	0	0	0	0
164389	C6-23	,	1,59	1,05	0,64	0,44	0,42	0,41	0,32	0,25	0,29	0,4	0,39	0,3	0,16	0,04	0	0	0	0	0	0	0	0	0	0	0	0	0
164375	C6-25	,	0,95	0,87	0,78	0,71	0,71	0,51	0,23	0,08	0,1	0,29	0,38	0,25	0,06	0,01	0	0	0	0	0	0	0	0	0	0	0	0	0
164378	C6-26	,	1,39	0,87	0,49	0,35	0,37	0,46	0,5	0,45	0,36	0,18	0,07	0,01	0	0	0	0	0	0	0	0	0	0	0	0	0	0	0
164373	C6-27	,	1,35	0,8	0,36	0,13	0,05	0	0	0	0	0	0	0	0	0	0	0	0	0	0	0	0	0	0	0	0	0	0
164388	C6-28	,	2,34	1,79	1,29	0,92	0,77	0,49	0,2	0,05	0	0	0	0	0	0	0	0	0	0	0	0	0	0	0	0	0	0	0
164216	C6-29	.	1,47	1,08	0,75	0,58	0,55	0,45	0,27	0,12	0,01	0	0	0	0	0	0	0	0	0	0	0	0	0	0	0	0	0	0
164380	C6-3	,	4,42	4,62	4,63	4,4	4,33	3,69	2,98	2,18	1,4	0,7	0,34	0,12	0,01	0	0	0	0	0	0	0	0	0	0	0	0	0	0
164381	C6-4	,	1,94	1,6	1,26	1,03	0,98	0,86	0,7	0,49	0,32	0,17	0,05	0	0	0	0	0	0	0	0	0	0	0	0	0	0	0	0
164208	C6-5	.	6,22	5,86	5,14	4,16	3,55	2,38	1,4	0,7	0,4	0,3	0,24	0,17	0,03	0	0	0	0	0	0	0	0	0	0	0	0	0	0
164208R	C6-5-RM	,	5,94	5,66	5,04	4,17	3,65	2,64	1,8	1,09	0,6	0,26	0,11	0,01	0	0	0	0	0	0	0	0	0	0	0	0	0	0	0
164385	C6-6	,	2,26	1,77	1,3	0,99	0,89	0,78	0,65	0,48	0,31	0,14	0,08	0,07	0,1	0,11	0,15	0,18	0,15	0,11	0,02	0	0	0	0	0	0	0	0
164382	C6-7	,	3,04	2,35	1,7	1,22	1,04	0,77	0,5	0,27	0,17	0,12	0,08	0,01	0	0	0	0	0	0	0	0	0	0	0	0	0	0	0
164383	C6-8	,	4,99	4,49	3,79	3,02	2,63	1,95	1,4	0,9	0,53	0,25	0,12	0,02	0	0	0	0	0	0	0	0	0	0	0	0	0	0	0
164386	C6-9	,	1,5	0,94	0,49	0,26	0,2	0,12	0,06	0	0	0	0	0	0	0	0	0	0	0	0	0	0	0	0	0	0	0	0

		phi	X50/D50 µm	0.1-2000 micron (Phi)				63-2000 micron (Phi)				< 8 µm	8-63 µm	8-16 µm	16-32 µm	32-63 µm	63-2000 µm	63-125 µm	125-250 µm
Lab.nr.	Field Code	µm	Median	Mean	St. Dev.	Skewness	Kurtosis	Mean	St. Dev.	Skewness	Kurtosis	%Clay	%Silt	%Very Fine Silt	%Fine Silt	%Coarse Silt	%Sand	%Very Fine San	%Fine Sand
164264	C1_11	.	4,94	7,78	1,78	0,45	2,84	3,88	0	<E15,1300>	<E15,1300>	63,98	36,01	19,59	13,2	3,23	0,01	0,01	0
164263	C1_13	.	5,99	7,65	1,66	0,7	3,23	<E15>	<E15>	<E15>	<E15>	60,07	39,93	25,68	12,49	1,75	0	0	0
164262	C1_15	.	4,52	7,88	1,51	0,48	3,38	3,88	0	<E15,1300>	<E15,1300>	70,87	29,1	20,53	7,29	1,28	0,03	0,03	0
164261	C1_17	.	4,97	7,77	1,64	0,44	3,11	3,78	0,13	-0,57	1,72	65,92	33,92	21,28	10,16	2,49	0,15	0,15	0
164266	C1_2	.	9,24	7,02	1,88	0,58	2,95	3,72	0,21	-1,31	4,25	46,07	52,04	20,42	20,4	11,22	1,89	1,88	0,01
164259	C1_21	.	9,62	7	1,83	0,65	3,1	3,69	0,24	-1,16	3,59	44,65	53,89	22,24	21,58	10,07	1,47	1,46	0,01
164258	C1_23	.	4,76	7,4	2,09	-0,33	2,84	3,41	0,37	-0,49	2,46	65,67	24,27	12,19	6,35	5,74	10,06	8,47	1,58
164257	C1_26	.	3,31	8,35	1,57	0,46	3,09	<E15>	<E15>	<E15>	<E15>	79,9	20,1	15,87	3,89	0,33	0	0	0
164265	C1_5	.	8,79	7,08	1,84	0,55	3,1	3,53	0,35	-0,83	2,82	47,19	50,66	22,54	20,03	8,09	2,15	1,94	0,21
164358	C1-1	.	8,04	7,1	1,89	0,42	2,88	3,68	0,24	-1,15	3,76	49,84	47,29	19,87	17,13	10,29	2,87	2,84	0,03
164359	C1-10	.	5,79	7,5	1,62	0,45	3,2	3,88	0	<E15,1300>	<E15,1300>	60,79	39,14	20,99	13,82	4,34	0,07	0,07	0
164365	C1-12	.	5,29	7,7	1,54	0,49	3,63	3,7	0,21	-0,85	2,79	66,58	32,94	22,84	8,02	2,08	0,49	0,49	0
164371	C1-14	.	12,24	6,66	1,93	0,63	2,96	3,63	0,29	-1,12	3,49	39,33	56,53	18,09	21,48	16,97	4,14	3,96	0,18
164362	C1-16	.	8,47	7,07	1,89	0,42	3	3,47	0,37	-0,55	2,3	48,3	48,38	21,7	17,6	9,07	3,32	2,89	0,44
164368	C1-18	.	7,16	7,24	1,87	0,36	2,86	3,49	0,37	-0,62	2,27	53,02	44,89	19,36	16,77	8,76	2,09	1,81	0,28
164260	C1-19	.	7,95	7,01	2	0,24	2,65	3,56	0,31	-0,82	2,93	50,15	43,74	17,28	15,01	11,45	6,11	5,73	0,38
164363	C1-20	.	5,22	7,71	1,66	0,48	3,12	3,88	0	<E15,1300>	<E15,1300>	64,46	35,52	20,96	11,62	2,94	0,02	0,02	0
164370	C1-22	.	4,18	8,07	1,4	0,74	3,76	<E15>	<E15>	<E15>	<E15>	78,18	21,82	18,12	3,67	0,04	0	0	0
164369	C1-24	.	5,4	7,63	1,52	0,45	3,57	3,72	0,2	-1,08	3,29	65,19	34,41	22,58	9,36	2,48	0,4	0,4	0
164364	C1-25	.	4,15	8,01	1,54	0,49	3,24	<E15>	<E15>	<E15>	<E15>	73,46	26,54	18,64	7,12	0,78	0	0	0
164367	C1-27	.	3,67	8,22	1,51	0,49	3,4	3,88	0	<E15,1300>	<E15,1300>	79,84	20,14	15,48	3,91	0,75	0,02	0,02	0
164361	C1-3	.	6,65	7,39	1,56	0,62	3,47	3,88	0	<E15,1300>	<E15,1300>	56,7	43,24	25,02	14,8	3,42	0,06	0,06	0
164366	C1-30	.	10,94	6,71	1,94	0,52	2,76	3,67	0,28	-1,42	4,42	43,16	53,21	15,09	18,83	19,29	3,63	3,49	0,14
164357	C1-4	.	6,13	7,48	1,61	0,52	3,41	3,71	0,2	-0,99	3,12	59,48	40,02	23,92	12,69	3,41	0,5	0,5	0
164355	C1-6	.	6,92	7,34	1,6	0,56	3,48	3,64	0,26	-0,84	2,74	55,23	44,15	25,42	14,7	4,04	0,61	0,6	0,01
164354	C1-7	.	8,5	7,05	1,82	0,47	2,97	3,67	0,25	-1,17	3,84	48,24	49,52	20,85	18,91	9,75	2,24	2,2	0,04
164356	C1-8	.	6,17	7,47	1,69	0,45	3,14	3,46	0,34	-0,27	1,97	58,18	41,22	22,44	14,74	4,04	0,6	0,54	0,06
164360	C1-9	.	4,24	8,02	1,62	0,49	3,08	<E15>	<E15>	<E15>	<E15>	71,99	28,01	19,11	7,93	0,97	0	0	0
164372	C1-end	.	5,96	7,54	1,82	0,39	2,99	3,41	0,39	-0,48	2,2	58,89	40,05	20,96	13,98	5,11	1,06	0,86	0,19
164377	C6	,	4,56	7,75	1,9	-0,05	3,19	3,35	0,39	-0,33	2,22	67,69	28,8	16,48	8,32	4	3,51	2,79	0,72
164387	C6-1	,	9,36	6,99	1,83	0,58	3,05	3,7	0,22	-1,11	3,54	45,5	52,58	21,65	20,44	10,49	1,92	1,92	0,01
164209	C6-10	.	4,83	7,84	1,44	0,63	3,7	<E15>	<E15>	<E15>	<E15>	71,25	28,75	21,35	6,48	0,92	0	0	0
164210	C6-11	.	4,69	7,78	1,57	0,27	3,49	3,73	0,19	-1,15	3,58	70,01	29,3	19,17	7,46	2,67	0,7	0,7	0
164376	C6-12	,	3,88	7,97	1,81	-0,19	3,55	3,52	0,31	-0,55	2,54	75,45	21,15	13,32	4,5	3,33	3,4	3,19	0,21
164384	C6-13	,	5,83	7,54	1,63	0,44	3,4	3,53	0,31	-0,45	2,16	61,26	37,97	22,94	11,88	3,15	0,77	0,73	0,04
164211	C6-14	.	7,98	7,17	1,72	0,56	3,24	3,71	0,22	-1,21	3,91	50,07	48,79	24,15	17,89	6,74	1,15	1,14	0
164212	C6-15	.	5,51	7,61	1,47	0,51	3,76	3,69	0,21	-0,81	2,73	65,28	34,37	23,62	8,76	1,99	0,35	0,35	0
164391	C6-16	,	10,26	6,87	1,97	0,5	2,91	3,41	0,4	-0,42	2,12	43,63	52,24	18,96	20,76	12,52	4,13	3,36	0,78
164390	C6-17	,	7,17	7,25	1,78	0,33	3,2	3,47	0,35	-0,52	2,37	53,49	43,78	23,07	14,93	5,78	2,73	2,42	0,31
164374	C6-18	,	5,9	7,4	1,77	0,21	3,02	3,61	0,29	-0,94	3,05	59,37	38,57	18,8	13,05	6,72	2,06	1,97	0,1
164213	C6-19	.	4,09	7,97	1,75	0,18	3,1	3,68	0,23	-1,04	3,4	71,55	27,53	16,52	7,79	3,21	0,93	0,92	0,01
164207	C6-2	.	5,19	7,6	1,64	0,23	3,24	3,46	0,34	-0,37	1,98	64,64	34,54	19,23	11,04	4,27	0,81	0,71	0,1
164379	C6-20	,	9,2	6,99	1,91	0,48	2,96	3,52	0,35	-0,75	2,68	46,16	50,42	20,55	19,46	10,41	3,42	3,09	0,33
164214	C6-21	.	3,8	8,13	1,53	0,39	3,37	3,88	0	<E15,1300>	<E15,1300>	77,92	22,06	15,43	5,43	1,2	0,02	0,02	0
164215	C6-22	.	3,8	8,16	1,43	0,52	3,67	3,88	0	<E15,1300>	<E15,1300>	80,6	19,35	15,14	3,58	0,63	0,05	0,05	0
164389	C6-23	,	4,57	7,84	1,59	0,07	4,04	3,26	0,39	-0,12	2,2	72,42	25,78	18,9	5,34	1,55	1,81	1,31	0,49
164375	C6-25	,	3,18	8,33	1,67	-0,07	3,85	3,19	0,32	0,3	2,8	83,19	15,64	9,93	3,66	2,06	1,17	0,85	0,32
164378	C6-26	,	4,64	7,84	1,5	0,31	4,03	3,65	0,24	-0,86	3,03	73,38	25,56	19,27	4,65	1,64	1,05	1,05	0,01
164373	C6-27	,	4,35	7,98	1,36	0,72	3,93	<E15>	<E15>	<E15>	<E15>	77,09	22,91	18,46	4,29	0,16	0	0	0
164388	C6-28	,	4,53	7,91	1,63	0,43	3,2	3,88	0	<E15,1300>	<E15,1300>	70,4	29,55	19,16	8,13	2,26	0,05	0,05	0
164216	C6-29	.	3,84	8,13	1,59	0,35	3,29	3,85	0,08	-2,8	9,58	76,99	22,88	16,01	5,11	1,76	0,13	0,13	0
164380	C6-3	,	9,2	6,86	1,95	0,38	2,65	3,65	0,27	-1,09	3,53	46,83	48,52	15,74	17,91	14,87	4,65	4,53	0,12
164381	C6-4	,	4,44	7,81	1,6	0,11	3,52	3,67	0,23	-0,93	3,09	72,02	26,97	16,51	7,02	3,44	1,01	1	0
164208	C6-5	.	10,53	6,89	1,83	0,66	3,14	3,53	0,36	-0,72	2,42	42,15	56,04	21,87	23,25	10,91	1,82	1,61	0,2
164208R	C6-5-RM	,	10,37	6,94	1,9	0,66	3,01	3,69	0,23	-1,19	3,74	43,02	54,95	20,85	22,4	11,7	2,03	2,01	0,01
164385	C6-6	,	4,38	7,87	1,83	-0,02	3,59	2,89	0,9	-0,37	1,6	69,55	28,57	17,45	7,92	3,2	1,88	0,99	0,43
164382	C6-7	,	5,12	7,74	1,74	0,39	3,09	3,61	0,28	-0,69	2,42	64,68	34,68	20,8	10,53	3,36	0,64	0,63	0,01
164383	C6-8	,	8,01	7,16	1,83	0,49	2,97	3,67	0,24	-1,13	3,59	49,97	48,26	21,38	18,29	8,59	1,77	1,75	0,02
164386	C6-9	,	4,28	7,98	1,4	0,6	3,78	<E15>	<E15>	<E15>	<E15>	76,23	23,77	18,3	4,87	0,6	0	0	0

Appendix 3

Isopach Maps Crevasse Splay 1 & 2

Isopach Map(cm) Crevasse Splay 1

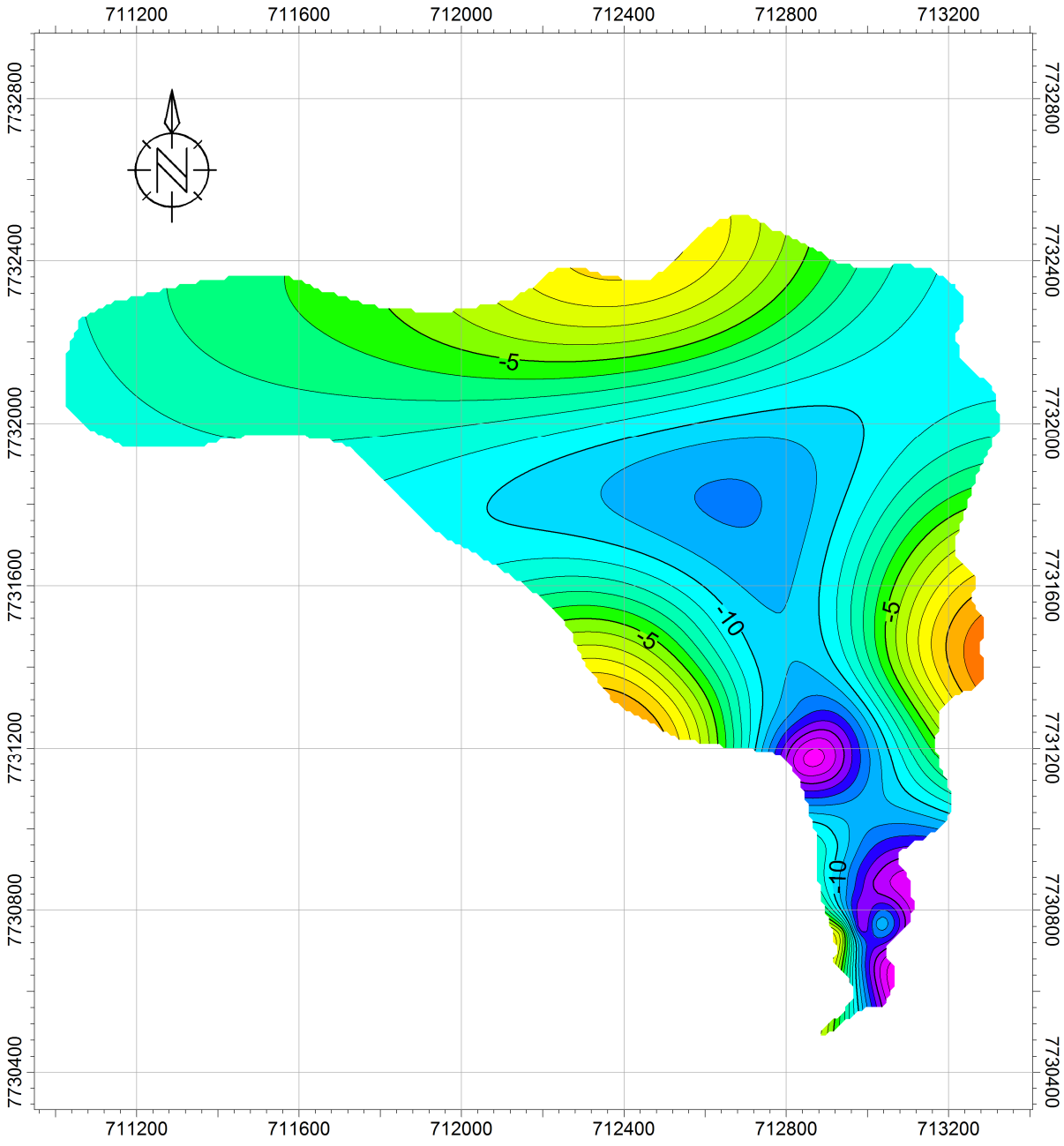

0 200 400 600 800 1000m

1:16384

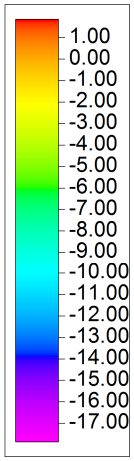

Isopach Map

Bolivia	*Scale* 1:16384
Potosi Dept	*Contour inc* 1
Crevasse splay 1	*Created by* ytorrescarranz
Thichness (cm)	*Date* 05/14/2013
Horizon name	*Signature*

PETREL

Isopach Map(cm)_Crevasse Splay 2

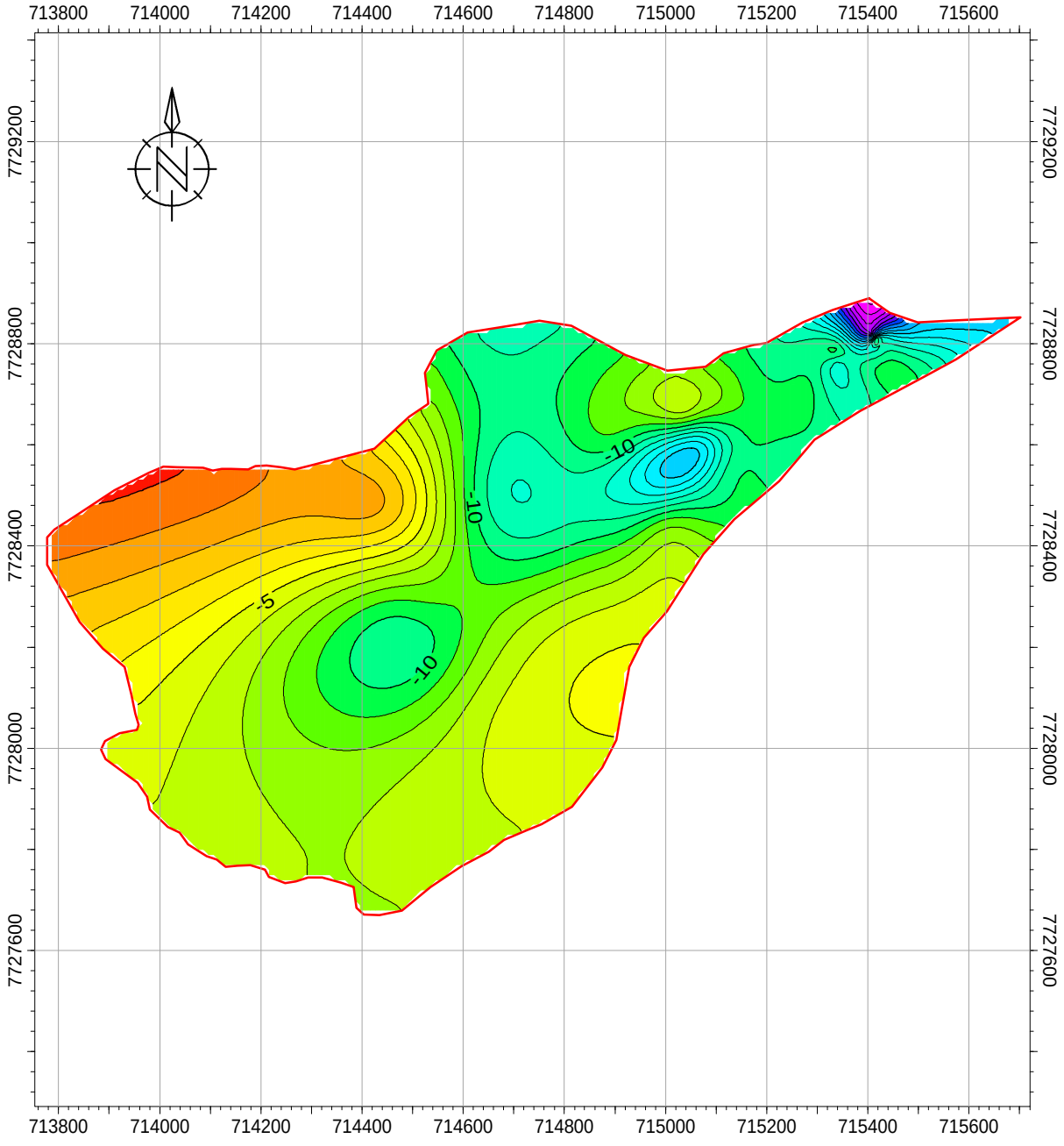

0 100 200 300 400 500m

1:13107

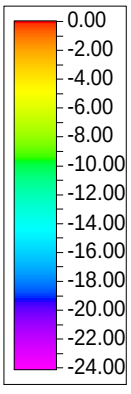

Isopach Map Crevasse Splay 2

Bolivia	*Scale* 1:13107
Uyuni	*Contour inc* 1
Potosi Dept	*User name* ytorrescarranz
Crevasse Splay 2	*Date* 05/14/2013
Thickness (cm)	*Signature*

PETREL

Appendix 4

Sedimentary Logs Crevasse Splay 1 & 2

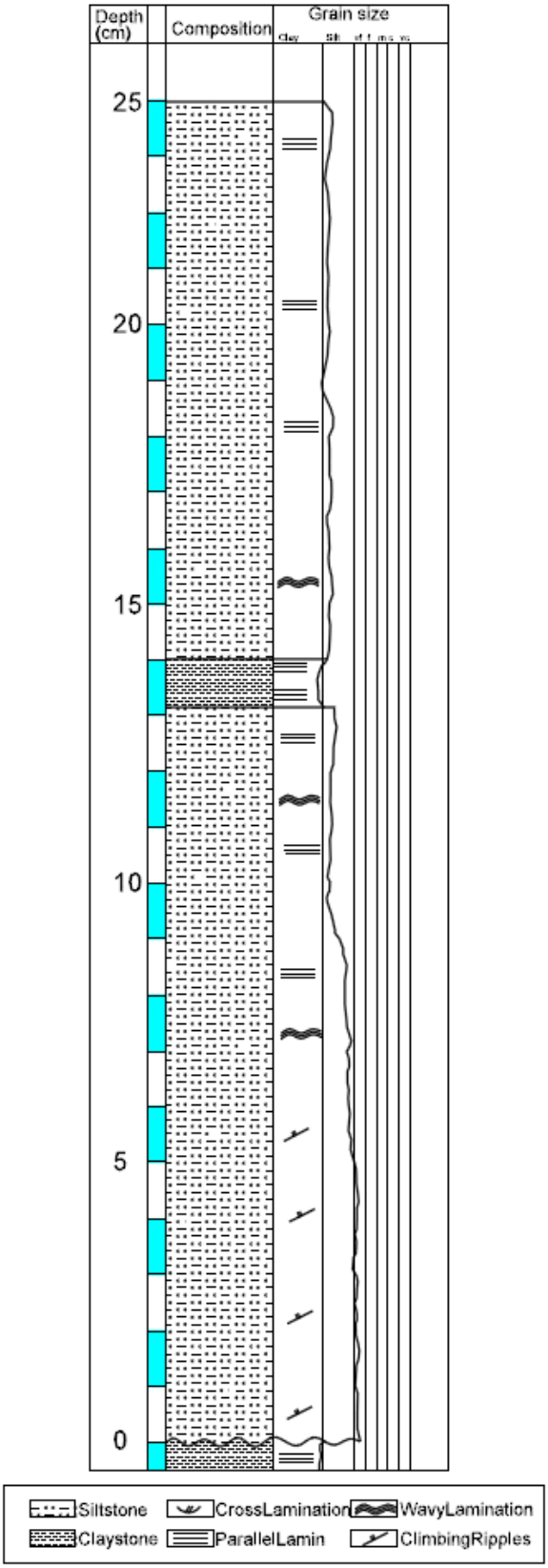

Appendix 7a. Sedimentary Log Crevasse Splay 1_Sample Location 21.

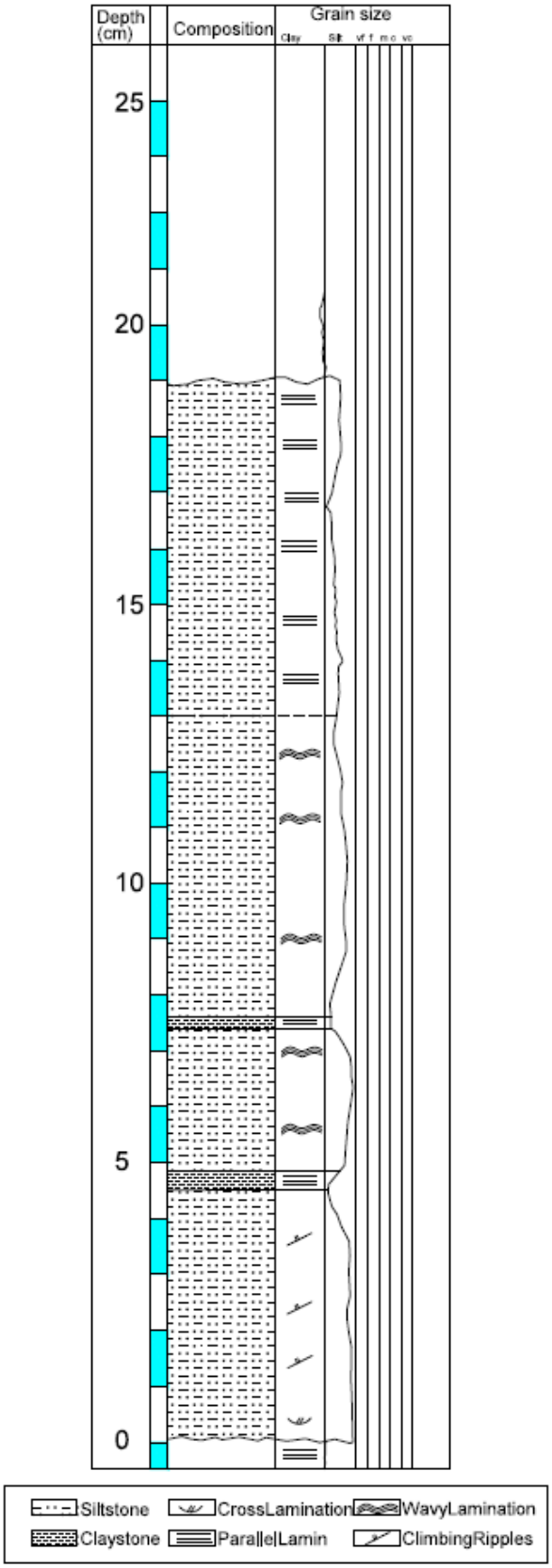

Appendix 7b.Sedimentary Log Crevasse Splay 2_Sample Location 1.

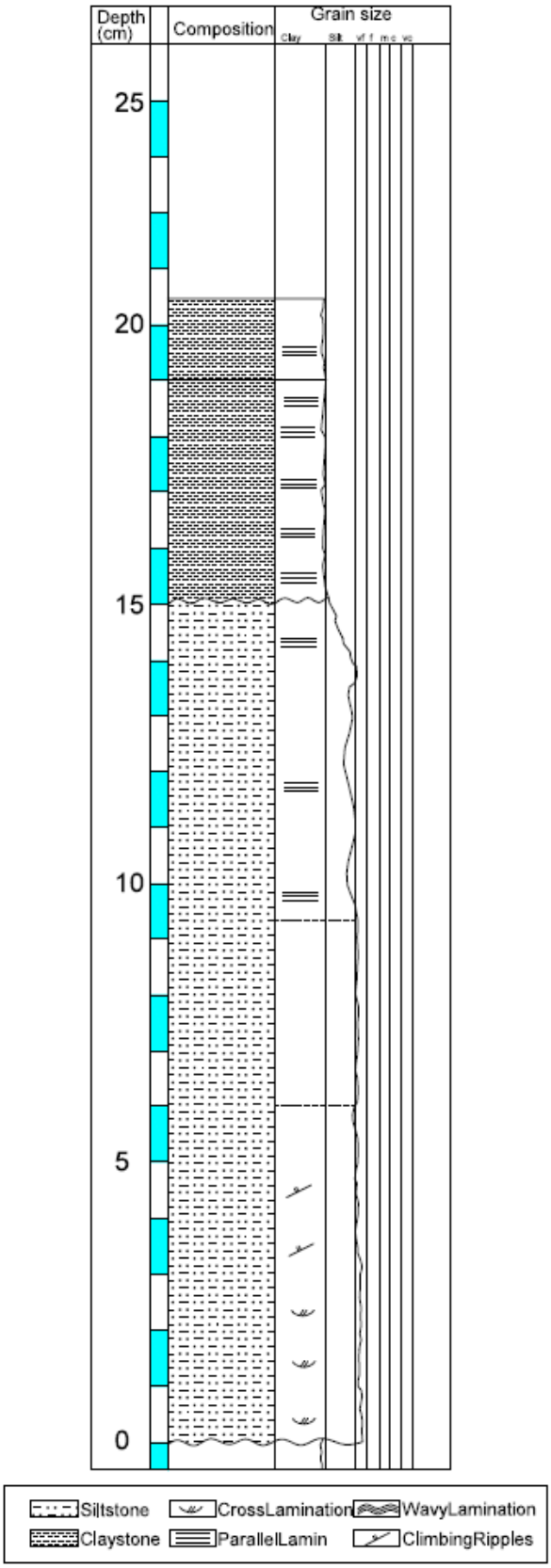

Appendix 7c. Sedimentary Log Crevasse Splay 2_Sample Location 14

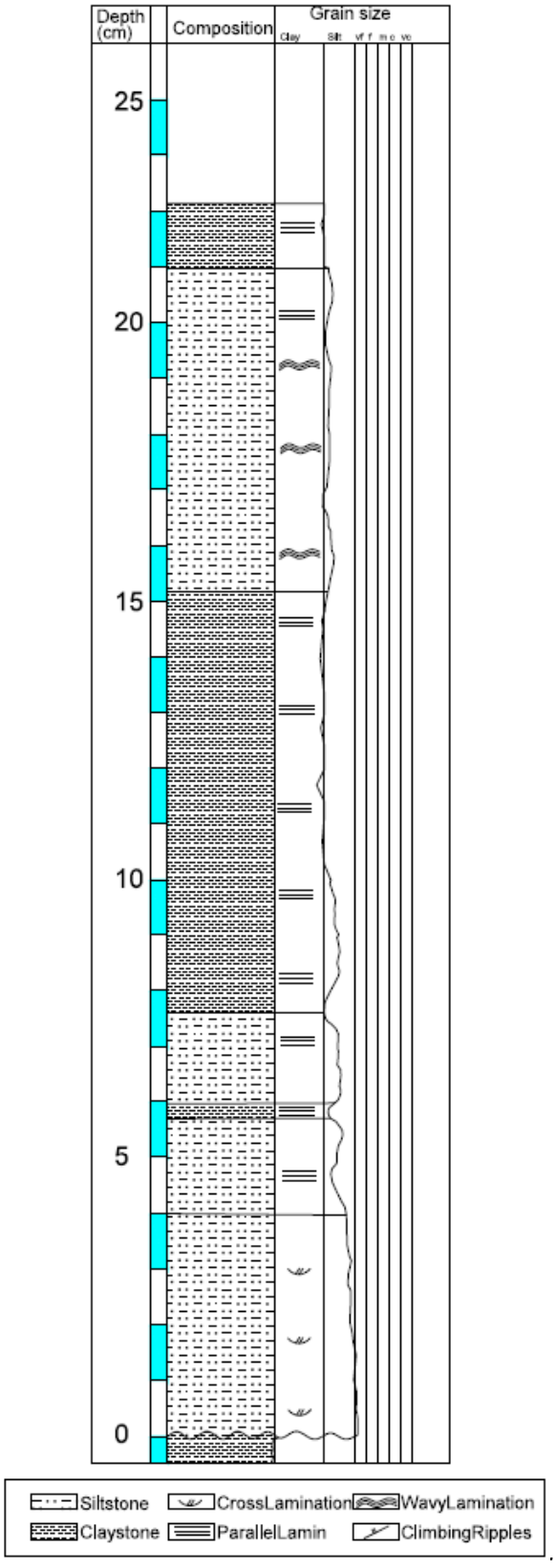

Appendix 7d. Sedimentary Log Crevasse Splay 2_Sample Location 19.

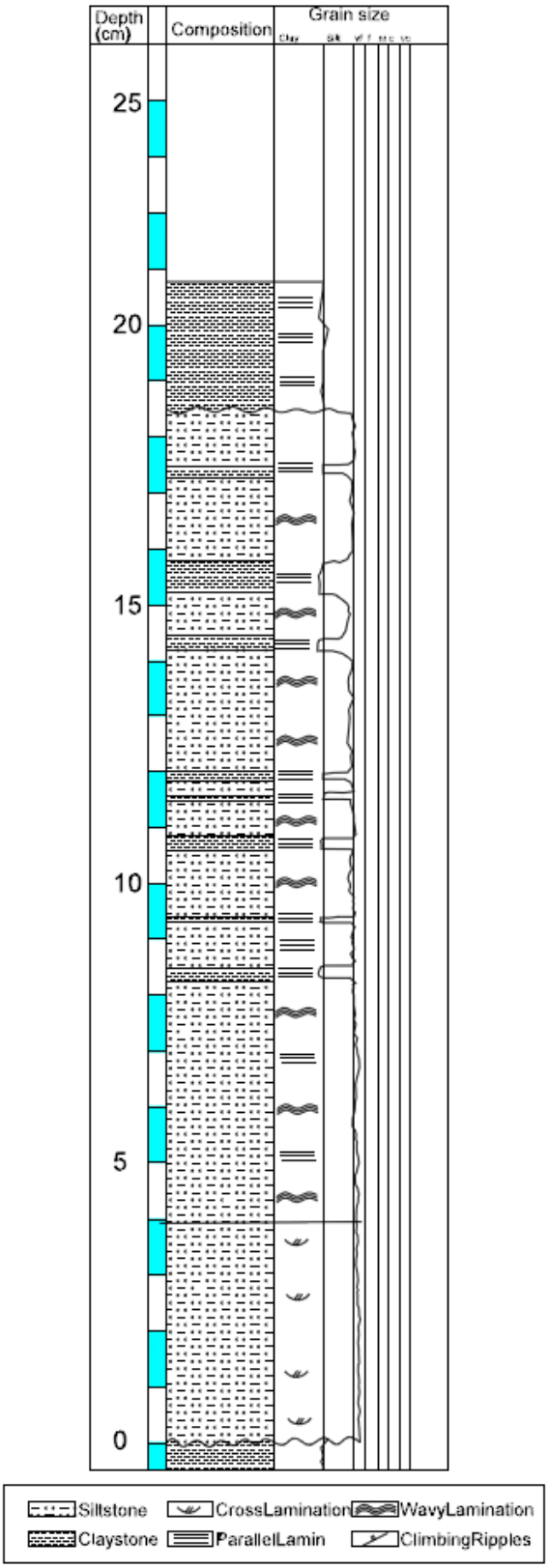

Appendix 7e. Sedimentary Log Crevasse Splay 2_Sample Location 23.

Appendix 5

Grain Size Maps Crevasse Splay 1 & 2

Median Grain Size Map(LaserAnalysis)_CS1

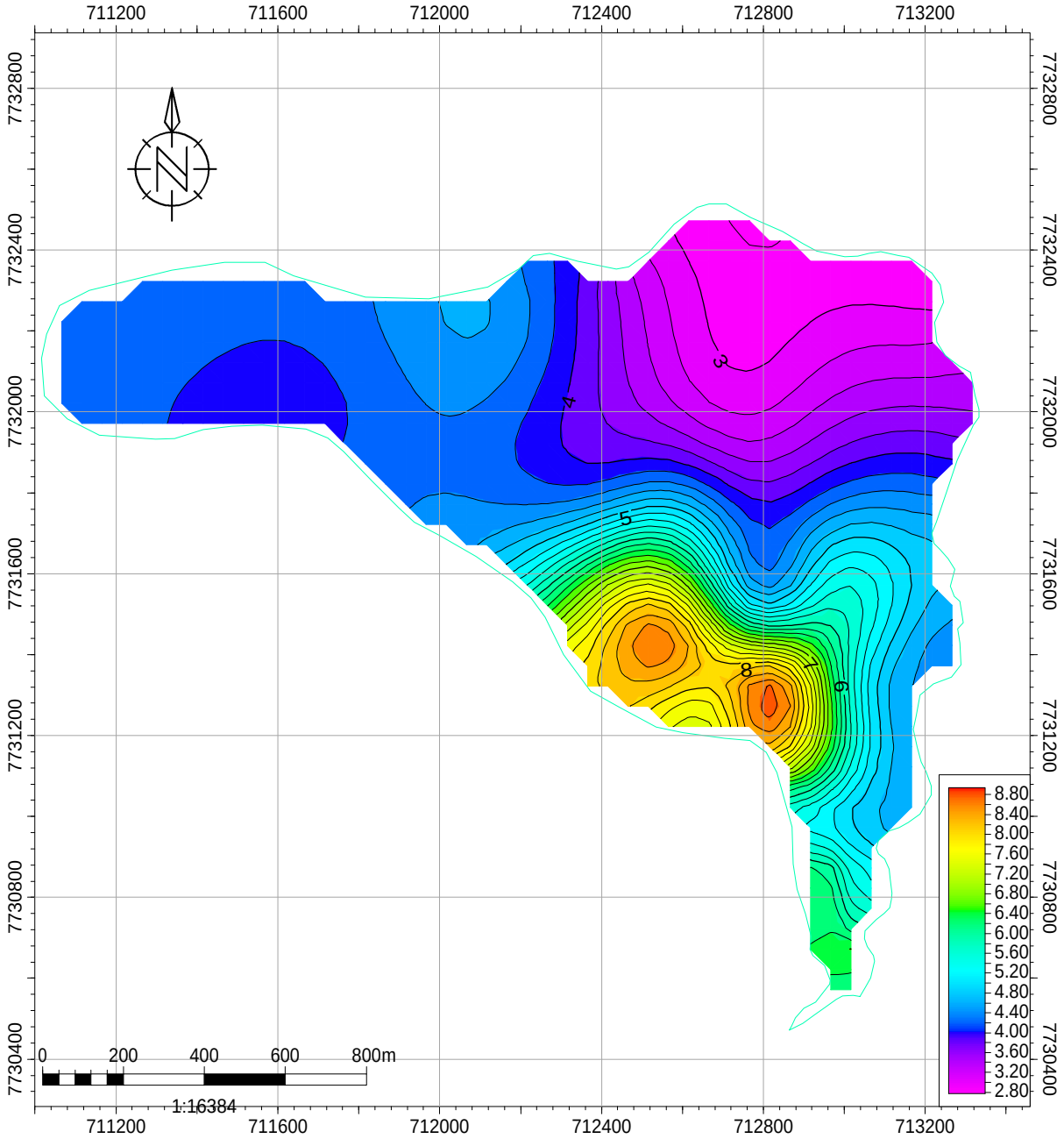

Map	
Bolivia	*Yadir Torres* ytorrescarranz
Area	*03/05/2013* 08/03/2013
Scale 1:16384	*Signature*
Cont Increment 0.2	

PETREL

Mean Grain Size Map(Silt_Weibull)_CS1

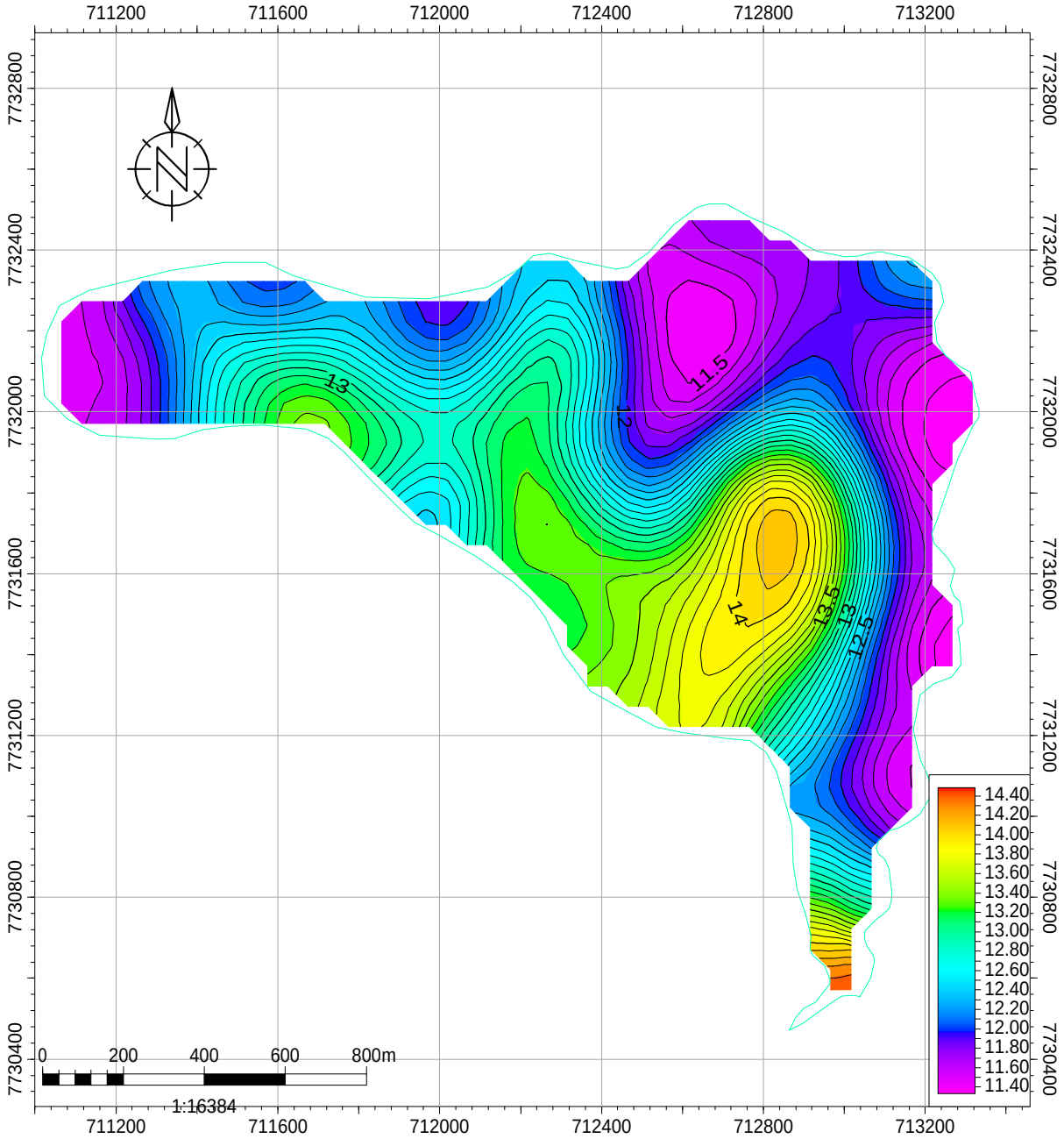

Map	
Bolivia	*Yadir Torres* ytorrescarranz
Area	*03/05/2013* 08/03/2013
Scale 1:16384	*Signature*
Cont Increment 0.1	

PETREL

Median Grain Size(um)-C.S_2

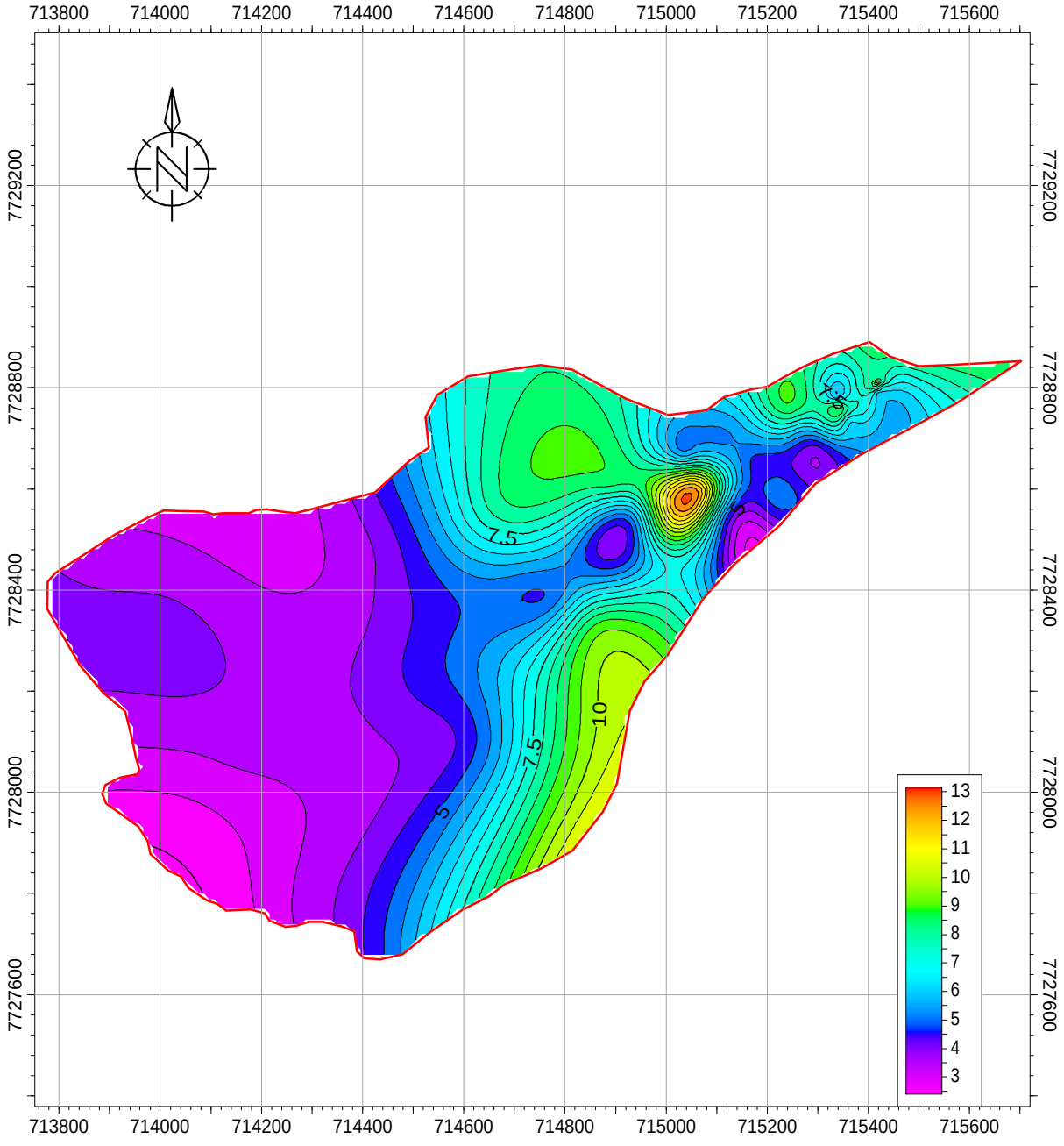

0 100 200 300 400 500m

1:13107

Map

Country	*Scale* 1:13107
Block	*Contour inc* 0.5
License	*User name* ytorrescarranz
Model name	*Date* 05/03/2013
Horizon name	*Signature*

PETREL

Mean Grain Size Weibull(um)-C.S_2

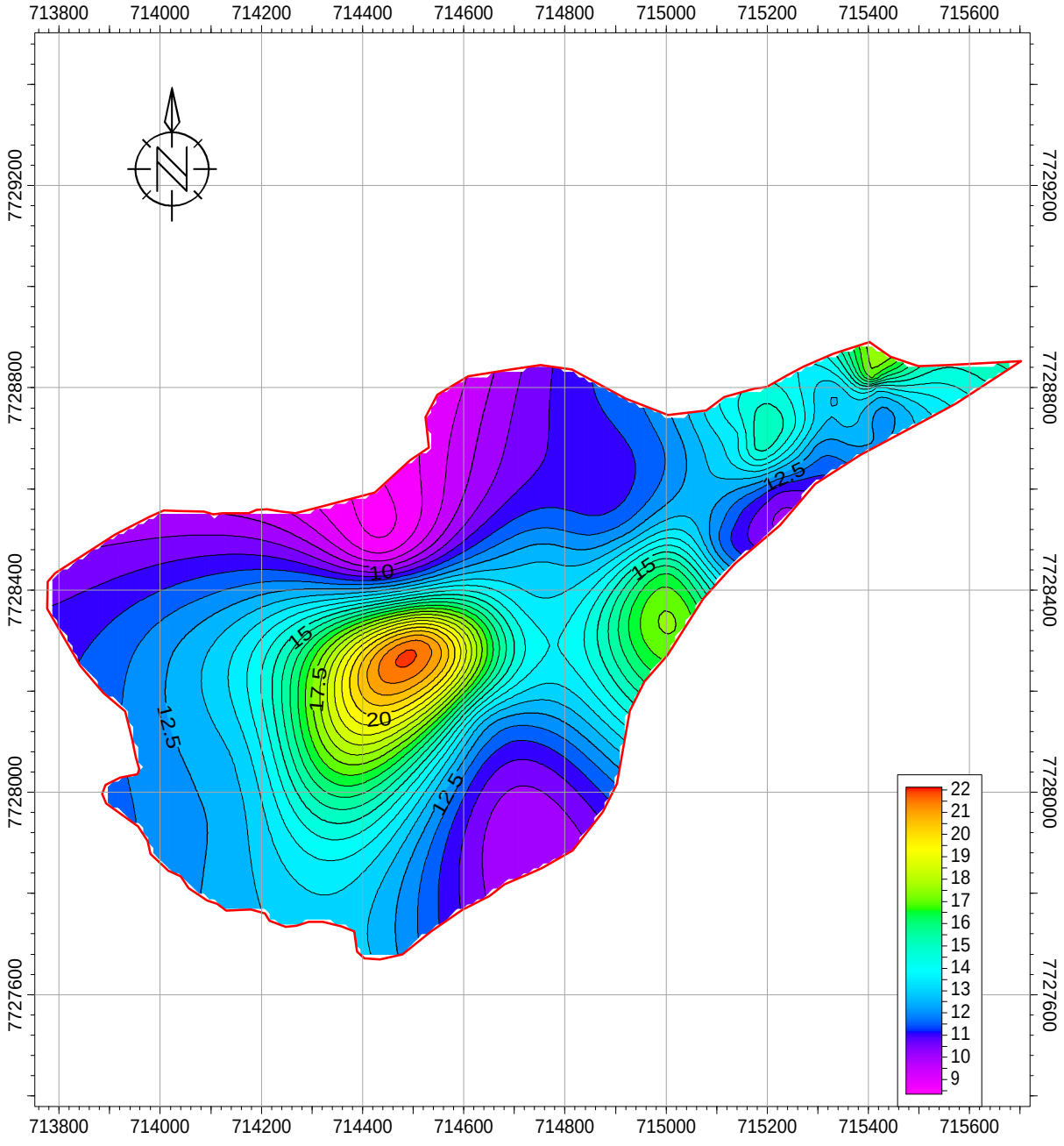

0 100 200 300 400 500m

1:13107

Map

Country	*Scale* 1:13107
Block	*Contour inc* 0.5
License	*User name* ytorrescarranz
Model name	*Date* 05/03/2013
Horizon name	*Signature*

PETREL

Mean Grain Size Map(Final Model)_CS1

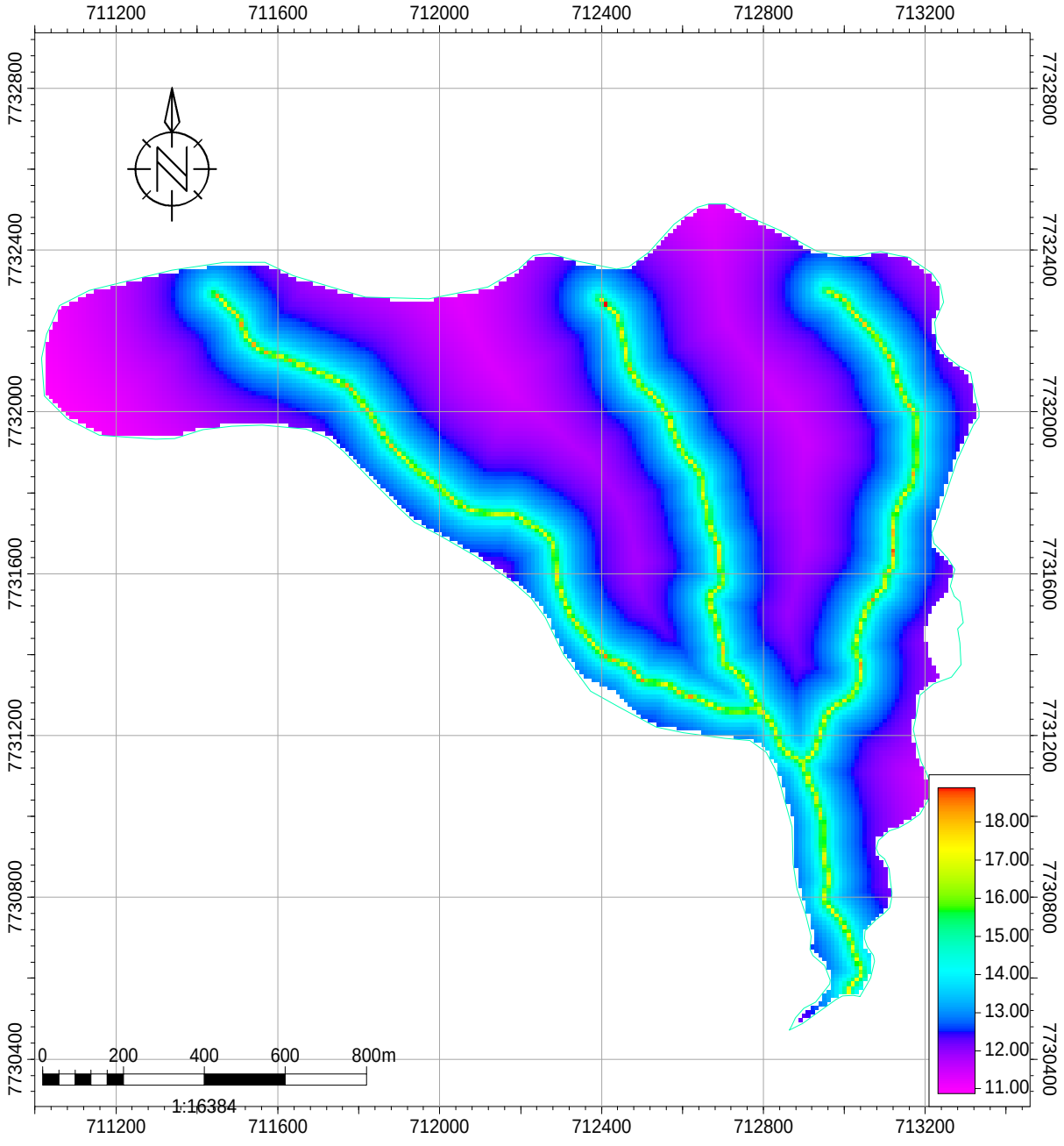

Map	
Bolivia	*Yadir Torres* ytorrescarranz
Area	*03/05/2013* 08/03/2013
Scale 1:16384	*Signature*
Cont Increment	

PETREL

Mean Grain Size Map(FinalModel)_CS2

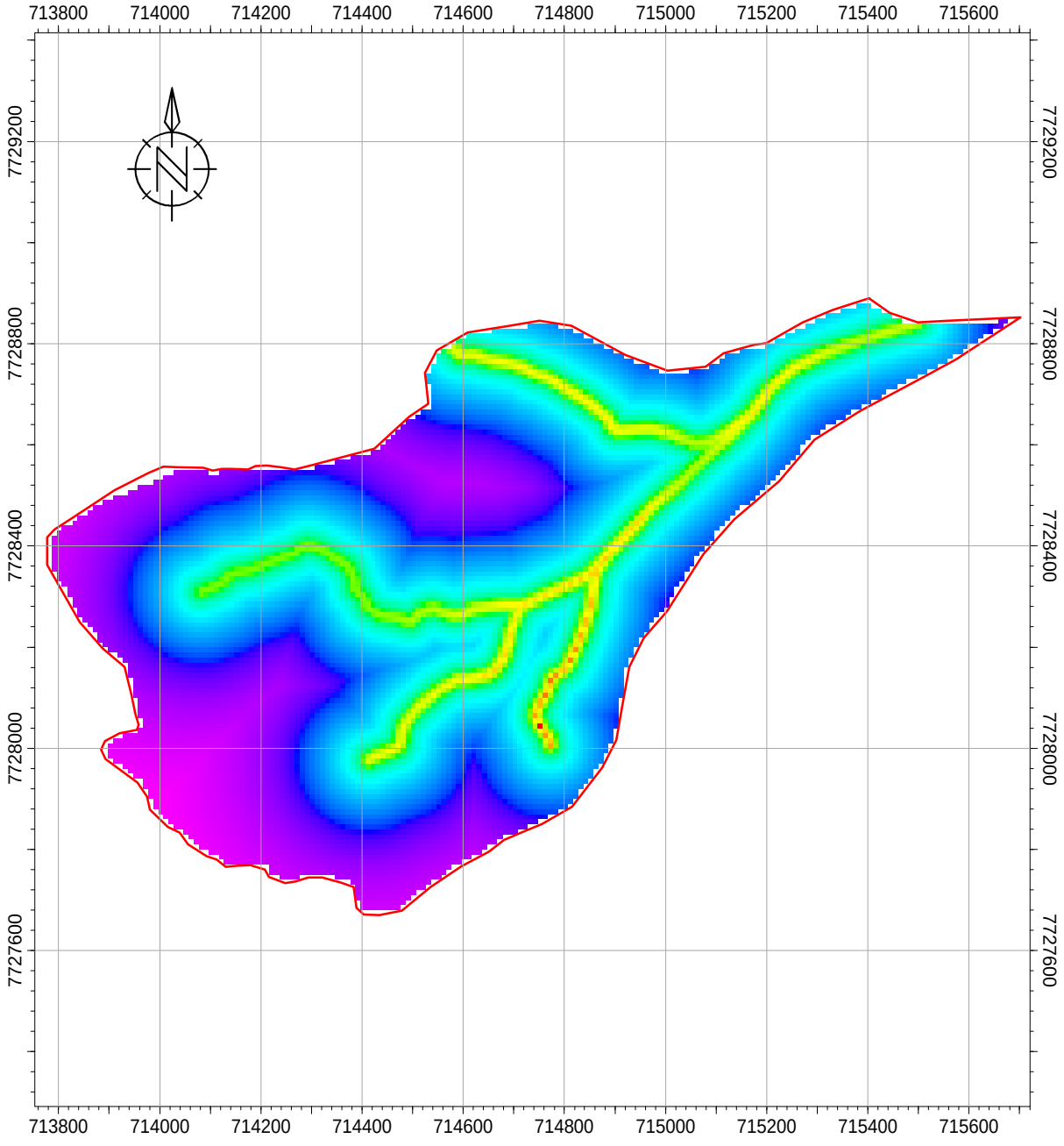

0 100 200 300 400 500m

1:13107

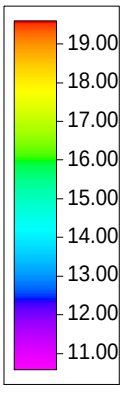

Final Grain Size Model[um]

Bolivia	*Scale* 1:13107
Uyuni	*Contour inc*
Potosi Dept	*User name* ytorrescarranz
Crevasse Splay 2 New model	*Date* 08/03/2013
Mean Size[um]	*Signature*

PETREL

Appendix 6

Cumulative Distributions Crevasse Splays 1 & 2

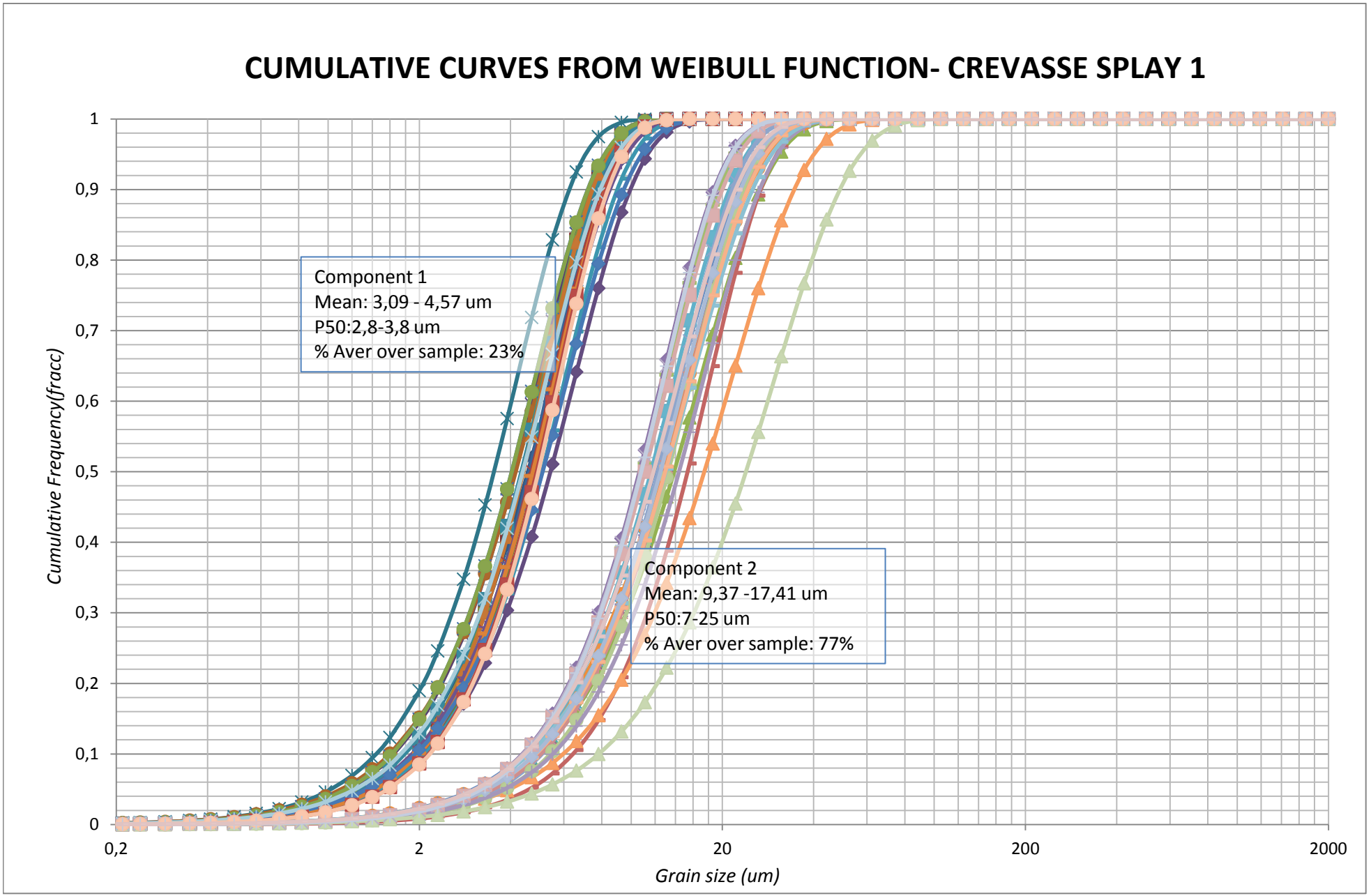
CUMULATIVE CURVES FROM WEIBULL FUNCTION- CREVASSE SPLAY 1
Component 1
Mean: 3,09 - 4,57 um
P50:2,8-3,8 um
% Aver over sample: 23%
Component 2
Mean: 9,37 -17,41 um
P50:7-25 um
% Aver over sample: 77%
Cumulative Frequency(fracc)
Grain size (um)
1
0,9
0,8
0,7
0,6
0,5
0,4
0,3
0,2
0,1
0
0,2
2
20
200
2000

CUMULATIVE CURVES FROM WEIBULL FUNCTION- CREVASSE SPLAY 2

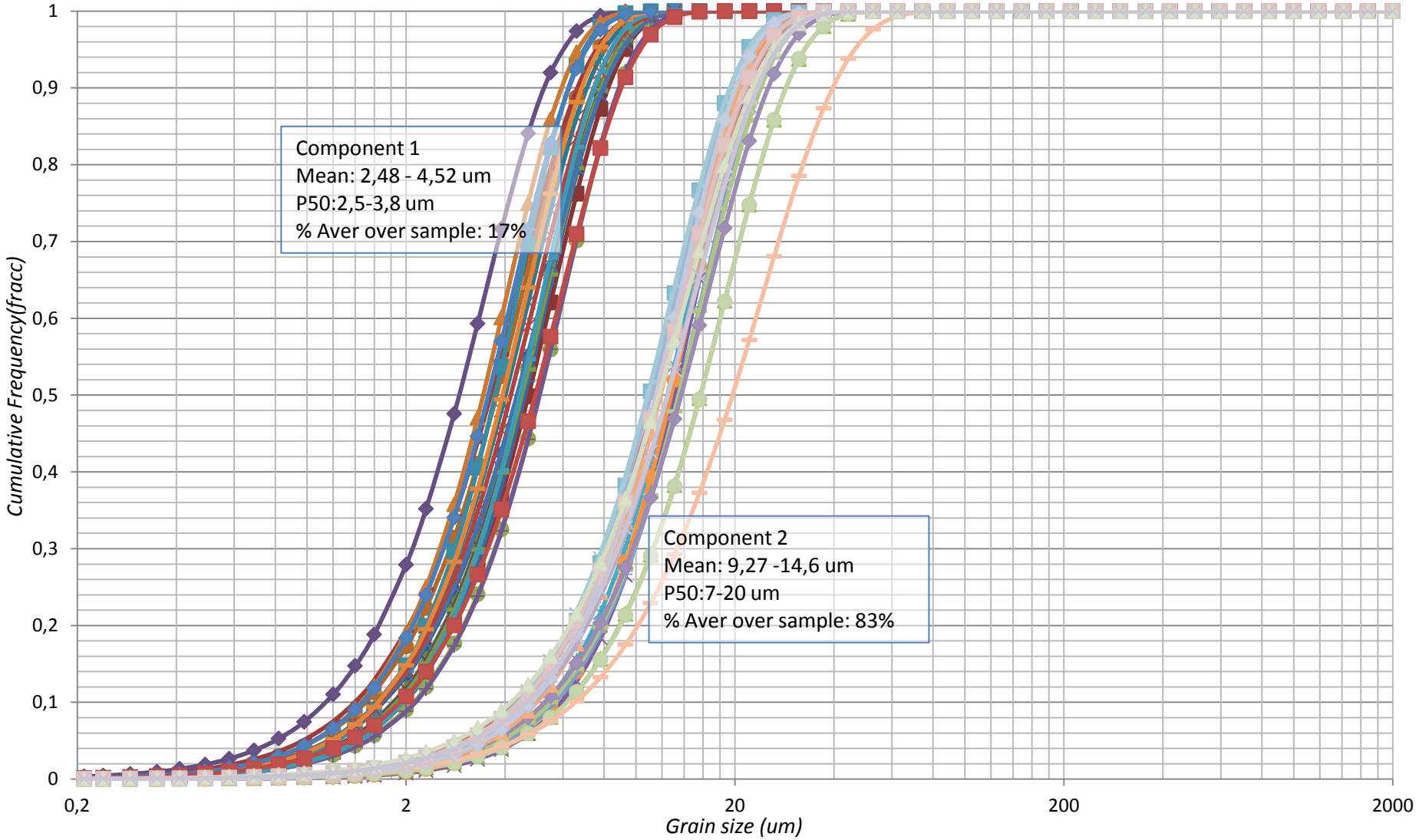

Appendix 7

ClayVolume Maps Crevasse Splays 1 & 2

Clay Volume Map(%)_CS1

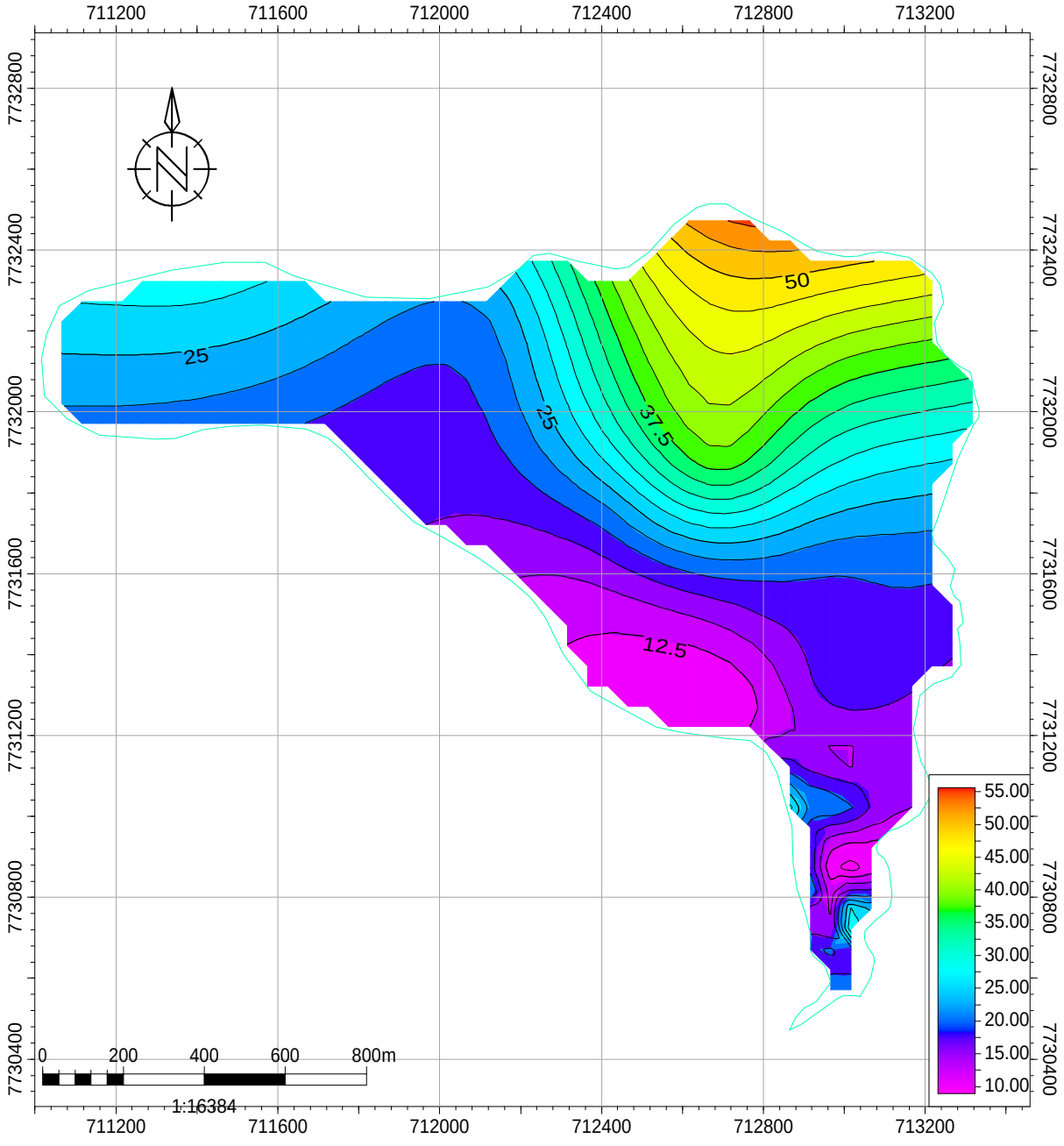

Map	
Bolivia	*Yadir Torres* ytorrescarranz
Area	*03/05/2013* 08/03/2013
Scale 1:16384	*Signature*
Cont Increment 2.5	

PETREL

Clay Volumen _C.S 2 (%)

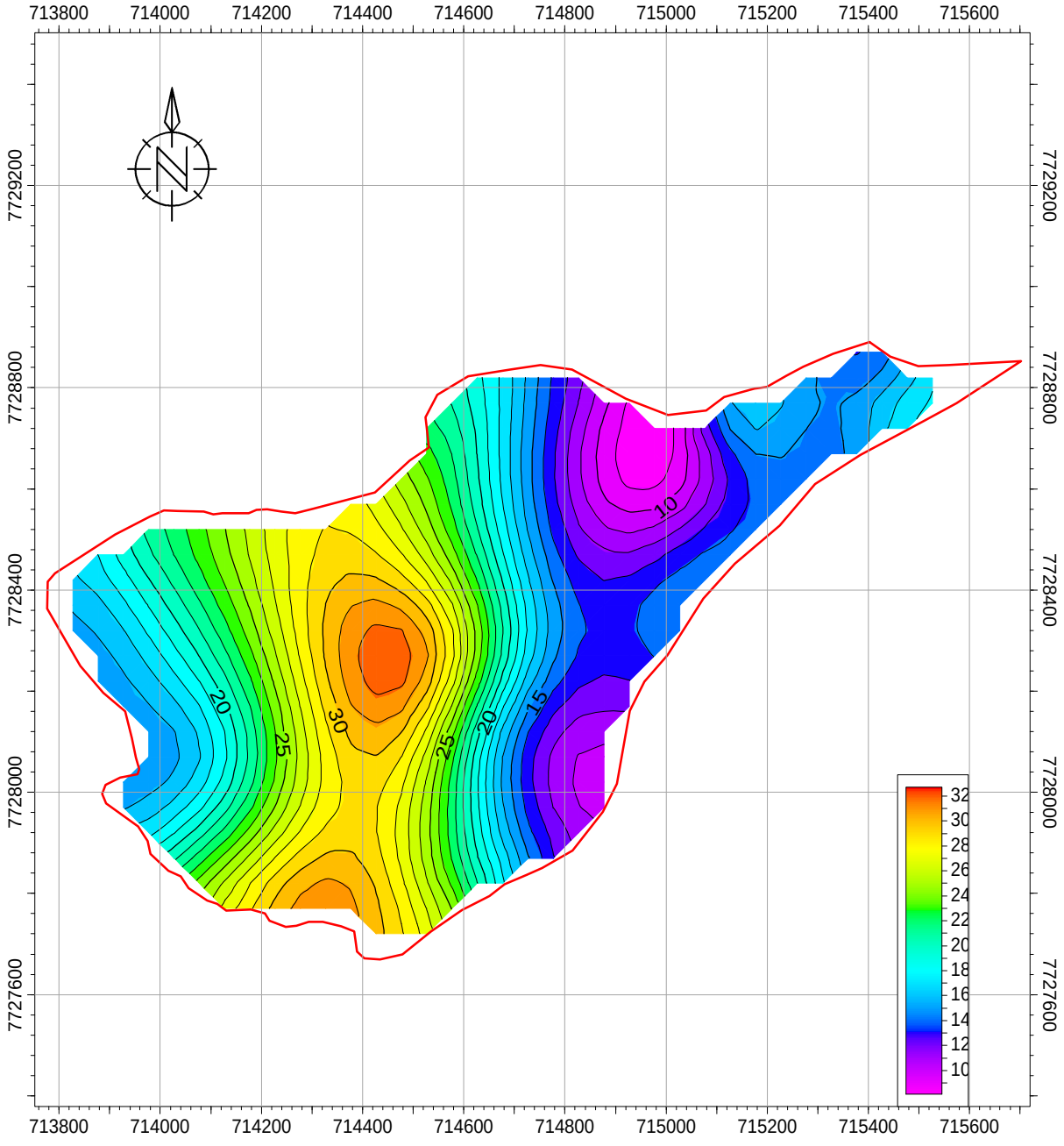

Map

Country	*Scale* 1:13107
Block	*Contour inc* 1
License	*User name* ytorrescarranz
Model name	*Date* 05/03/2013
Horizon name	*Signature*

0 100 200 300 400 500m

1:13107

PETREL

Appendix 8

Porosity Maps Crevasse Splay 1 & 2

Initial Porosity[-] Crevasse Splay 1

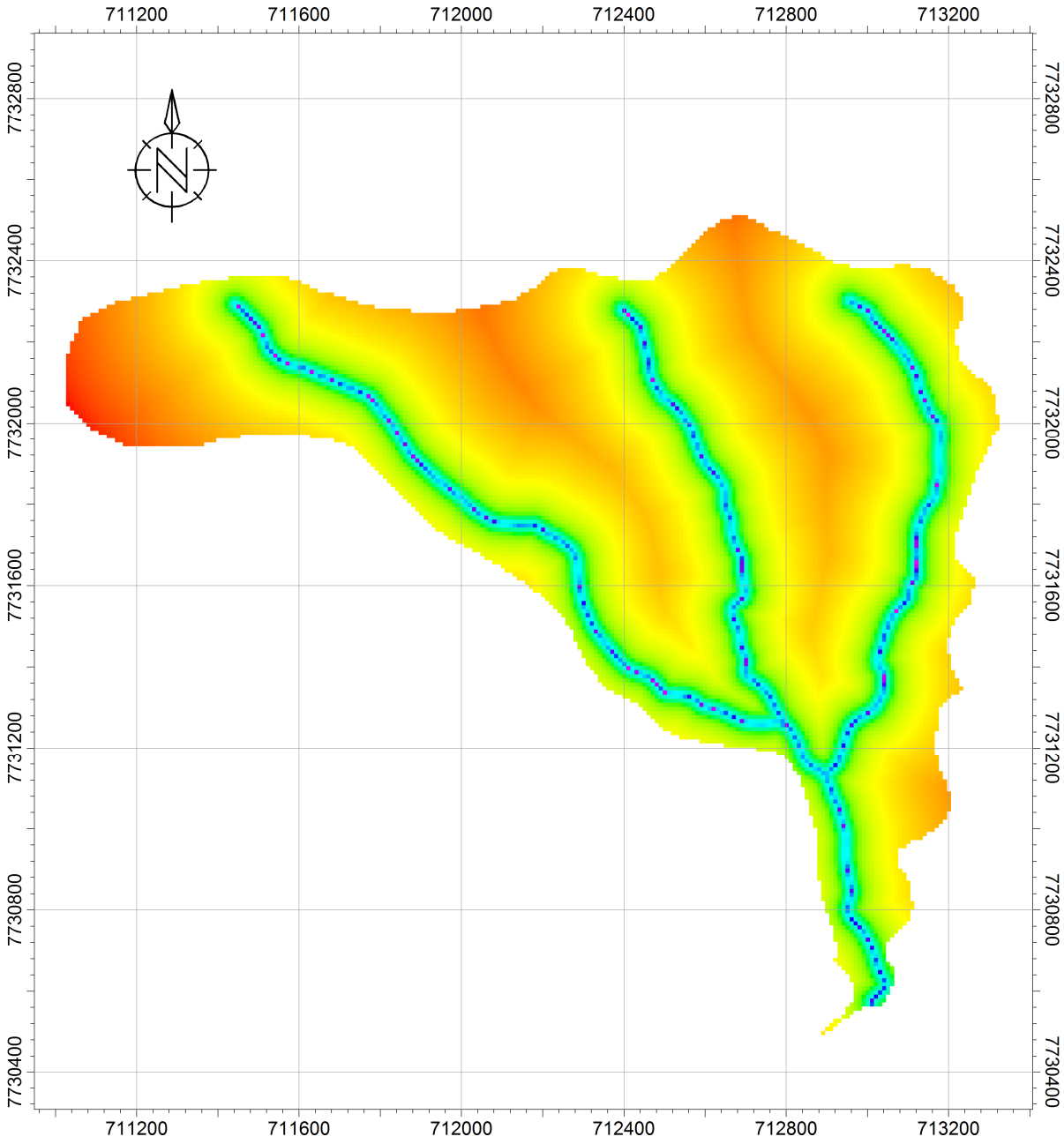

0 200 400 600 800 1000m

1:16384

0.5500
0.5450
0.5400
0.5350
0.5300
0.5250
0.5200
0.5150

Initial Porosity Map

Bolivia	*Scale* 1:16384
Potosi Dept	*Contour inc*
Crevasse splay 1 Crevasse Splay Finer Grid	*Created by* ytorrescarranz
Porosity[-] PHI	*Date* 06/26/2013
Horizon name	*Signature*

PETREL

Initial Porosity Map(-)_Crevasse Splay 2

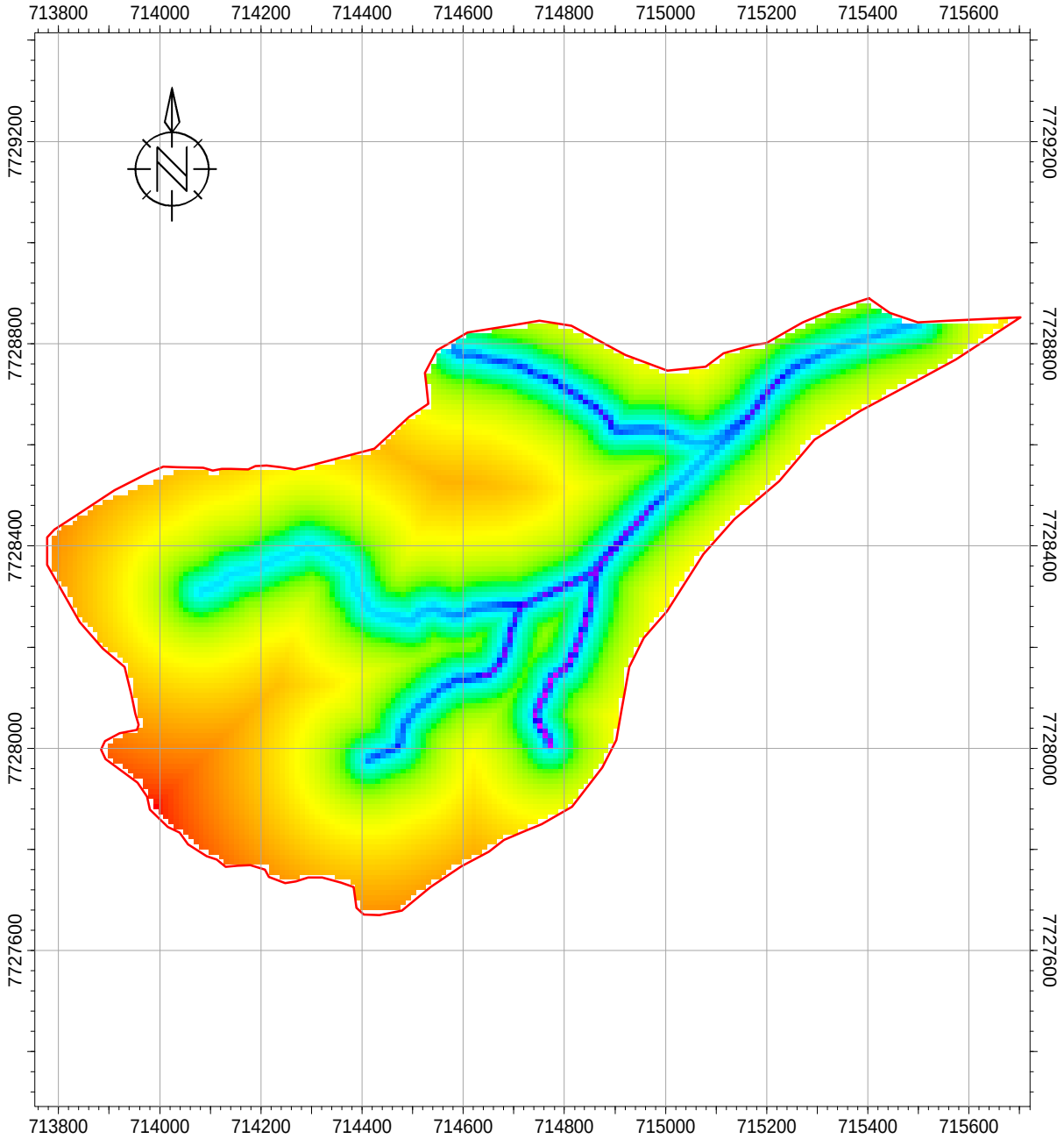

0 100 200 300 400 500m

1:13107

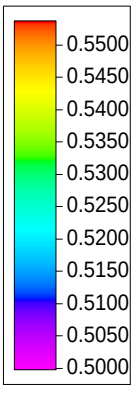

Initial Porosity Map Crevasse Splay 2

Bolivia	*Scale* 1:13107
Uyuni	*Contour inc*
Potosi Dept	*User name* ytorrescarranz
Crevasse Splay 2 New model	*Date* 06/26/2013
Porosity(-)	*Signature*

PETREL

Appendix 9

Permeability MapsCrevasse Splay 1 & 2

Permeability[mD] Crevasse Splay 1

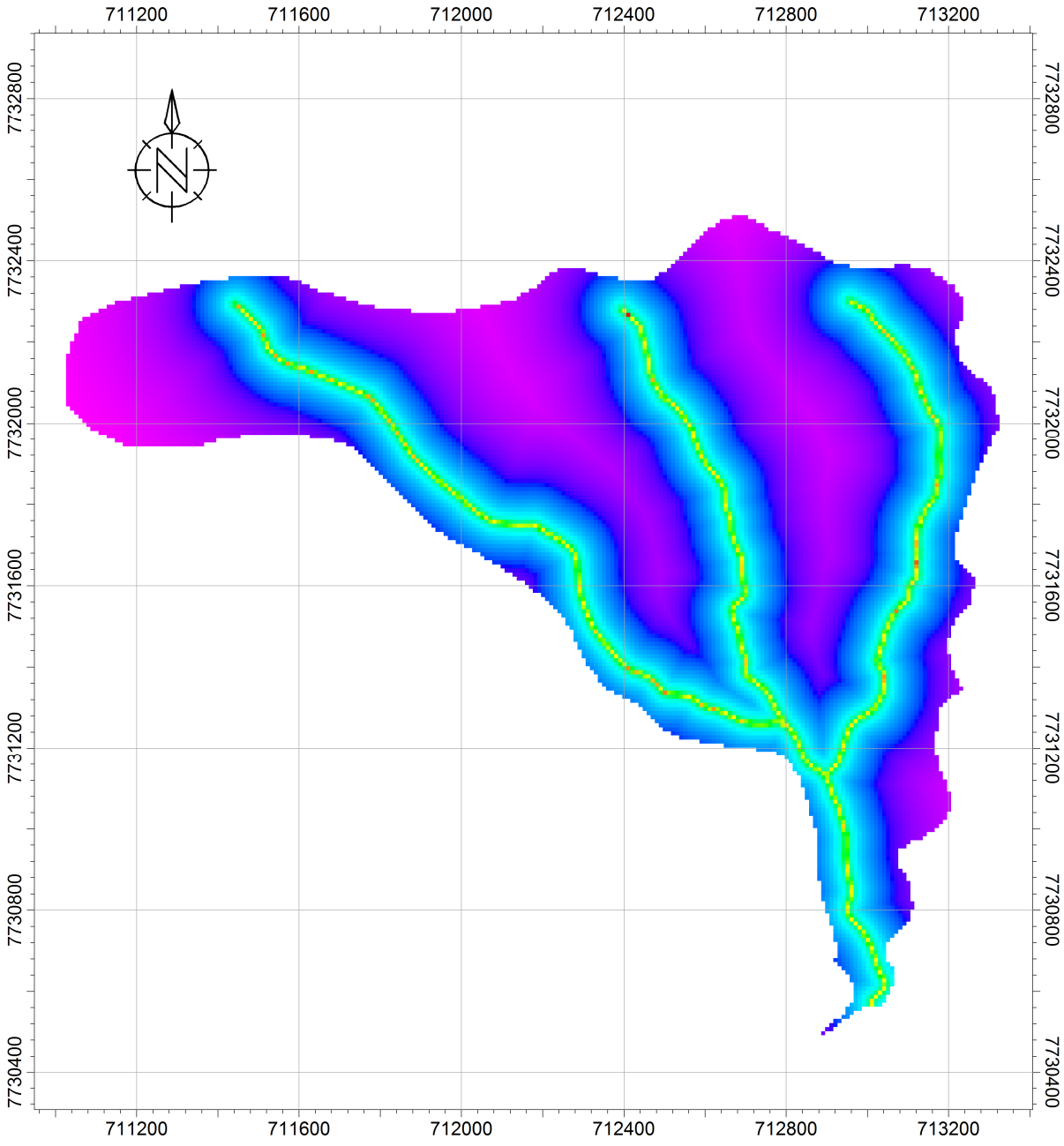

0 200 400 600 800 1000m

1:16384

480.00
460.00
440.00
420.00
400.00
380.00
360.00

Permeability Map at S.C	
Bolivia	*Scale* 1:16384
Potosi Dept	*Contour inc*
Crevasse splay 1 Crevasse Splay Finer Grid	*Created by* ytorrescarranz
Permeability[mD] Kckm	*Date* 06/26/2013
Horizon name	*Signature*

PETREL

Permeability Map(mD)_Crevasse Splay 2(S.C)

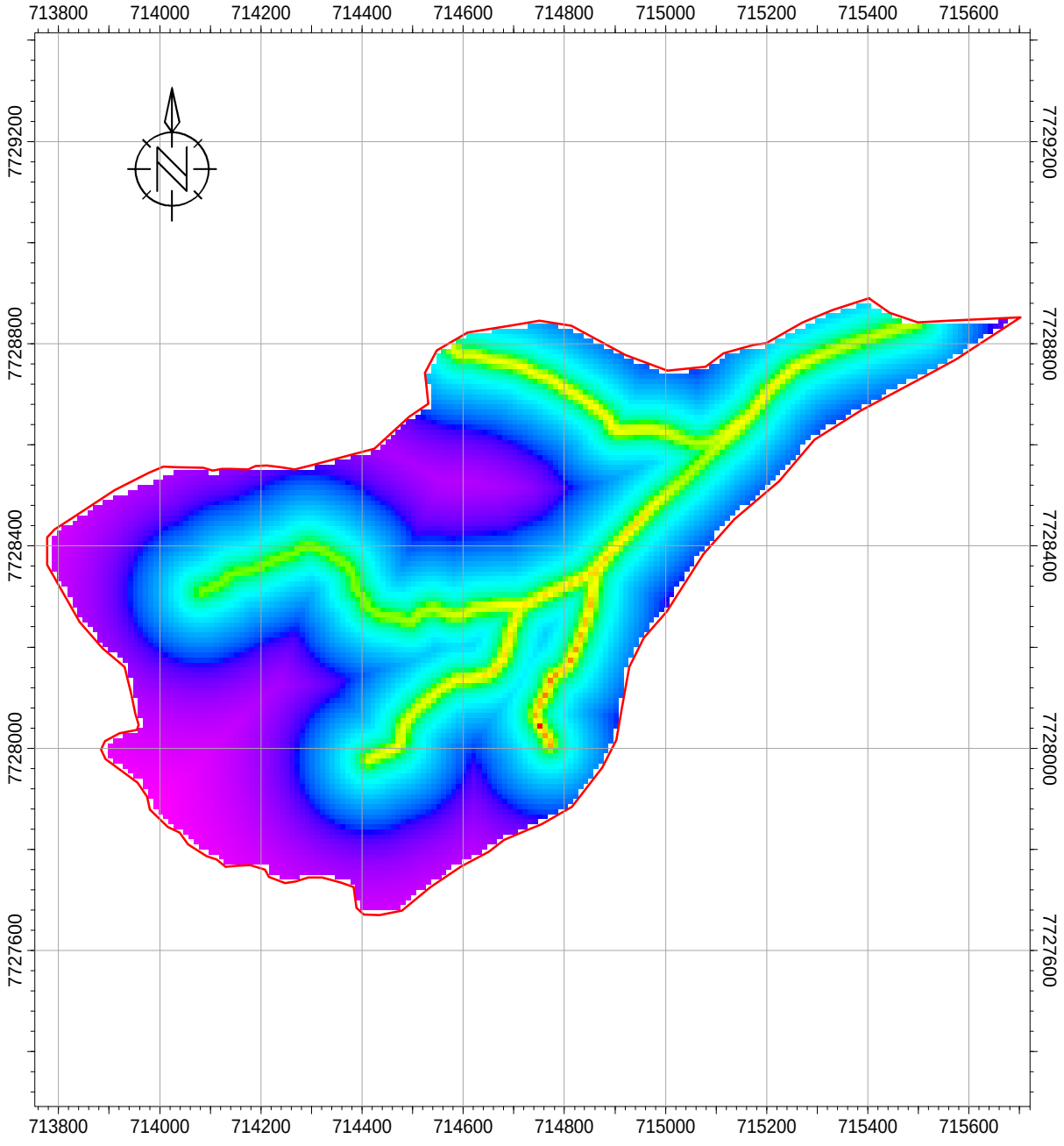

0 100 200 300 400 500m

1:13107

480.00
460.00
440.00
420.00
400.00
380.00
360.00

Permeability Map at S.C

Bolivia	*Scale* 1:13107
Uyuni	*Contour inc*
Potosi Dept	*User name* ytorrescarranz
Crevasse Splay 2 New model	*Date* 06/26/2013
Permeability[mD]	*Signature*

PETREL

Permeability[mD] Crevasse Splay 1

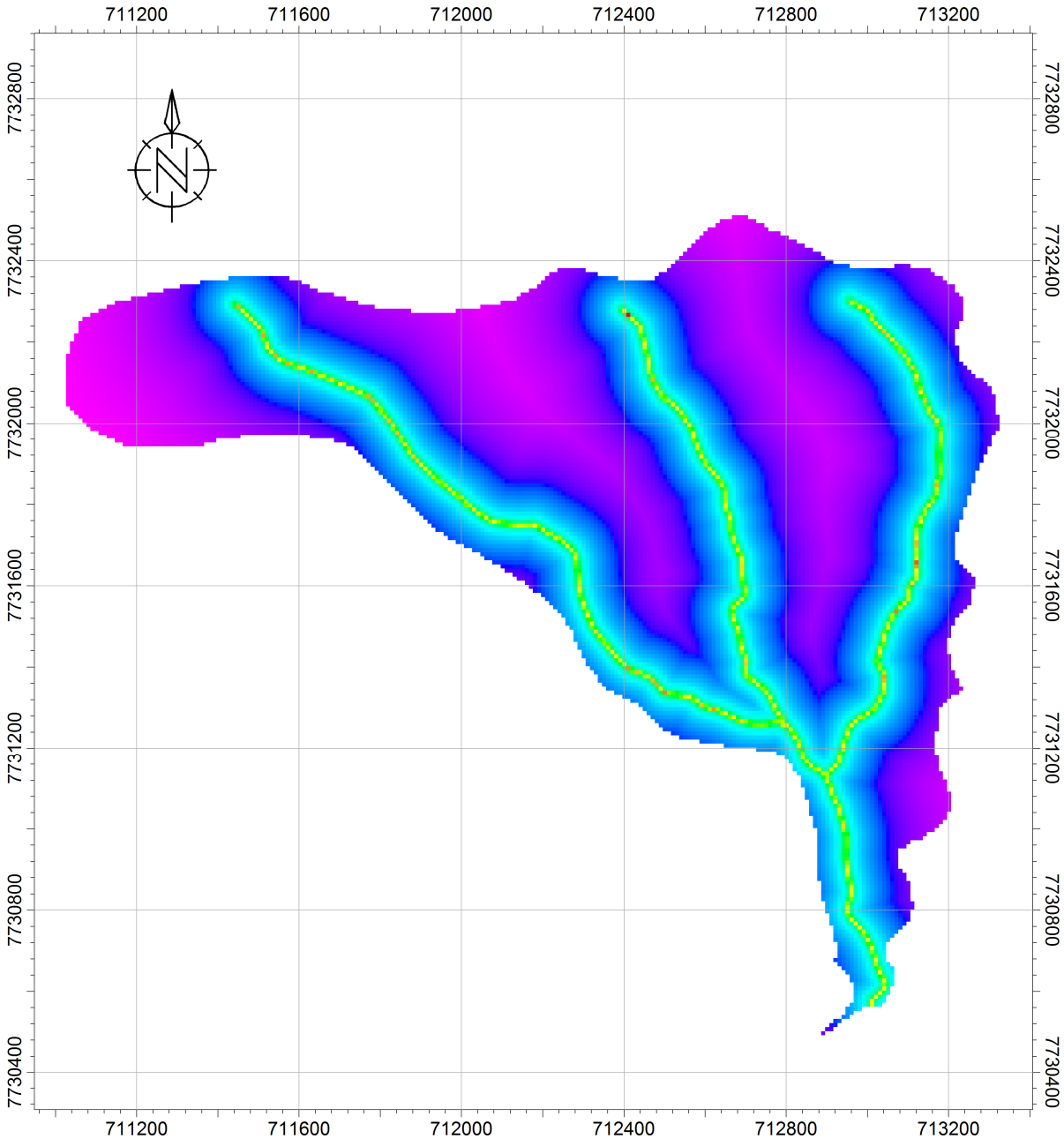

0 200 400 600 800 1000m

1:16384

0.13
0.12
0.11
0.10
0.09
0.08
0.07
0.06
0.05

Permeability Map at -3000m

Bolivia	*Scale* 1:16384
Potosi Dept	*Contour inc*
Crevasse splay 1 Crevasse Splay Finer Grid	*Created by* ytorrescarranz
Permeability[mD] Kckm_gs	*Date* 08/03/2013
Horizon name	*Signature*

PETREL

Permeability Map(mD)_Crevasse Splay 2(-3000)

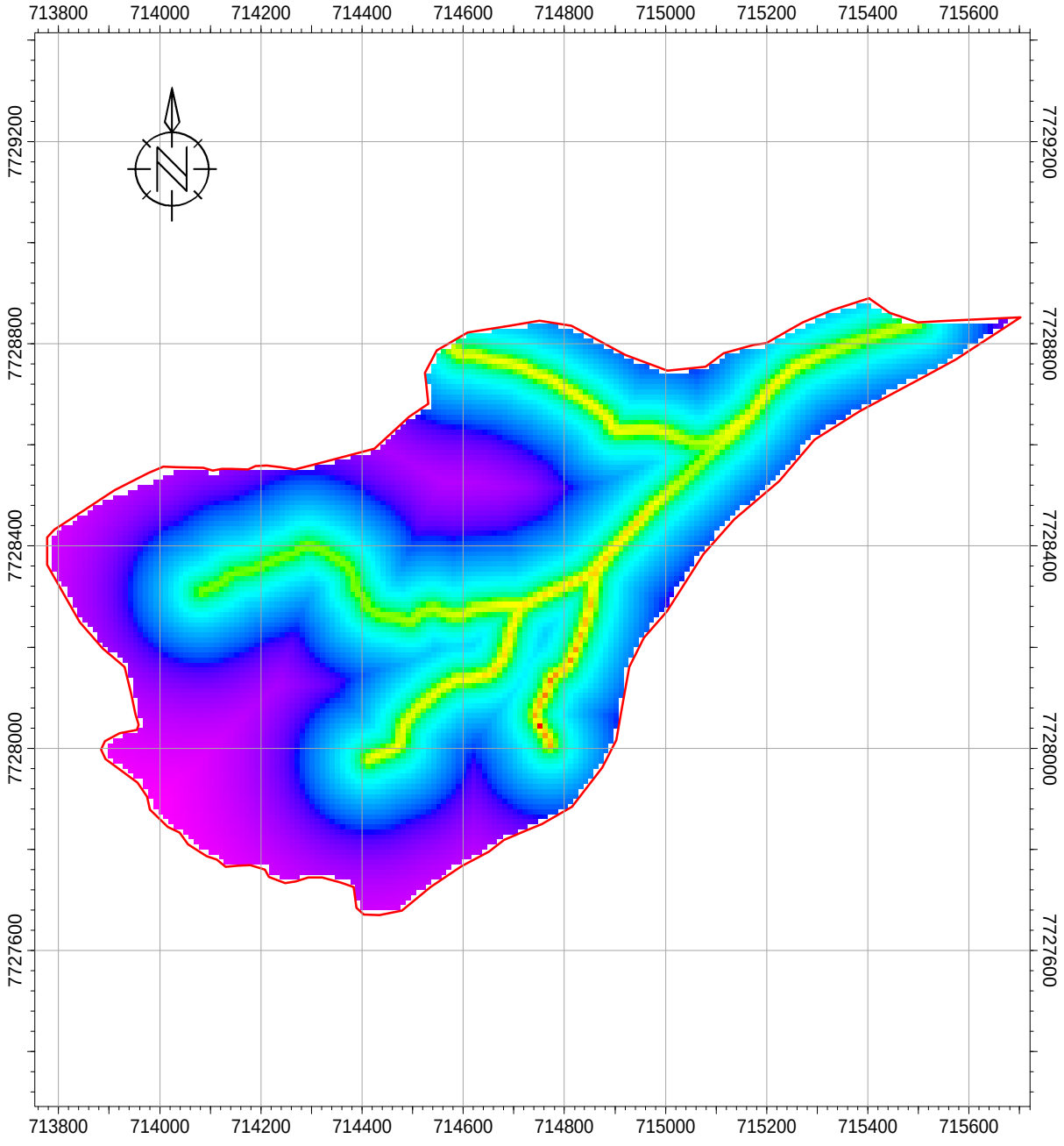

0 100 200 300 400 500m

1:13107

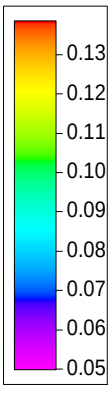

Permeability Map at -3000m

Bolivia	*Scale* 1:13107
Uyuni	*Contour inc*
Potosi Dept	*User name* ytorrescarranz
Crevasse Splay 2 New model	*Date* 08/03/2013
Permeability[mD]	*Signature*

PETREL